EQUAL-CHANNEL ANGULAR PRESSING OF HIGH-CARBON STEEL

REINIER BERGWERF

EQUAL-CHANNEL ANGULAR PRESSING OF HIGH-CARBON STEEL

Master thesis

REINIER BERGWERF

12 March 2007

Supervisors: Dr. Jilt Sietsma (TU Delft)
Dr. Alexis Miroux (NIMR)

Delft University of Technology
Department of Materials Science and Engineering
Mekelweg 2
2628 CD Delft
The Netherlands

Technische Universiteit Delft

CONTENTS

CHAPTER 1
INTRODUCTION

The search for materials with a higher strength-to-weight ratio is one of the main topics in metals research and industry. Part of this search is motivated by the Hall-Petch relationship [22,64], which says that the strength of a material is inversely related to the square root of the grain size. At the time of the discovery of this relationship speculations were made about what would happen if the grain size were reduced to one micrometer or less. Calculations predicted a tremendous increase of the strength and hardness, if such small grain sizes were achieved. Unfortunately, at that time only small amounts could be produced on a laboratory scale, because there were no machines available to produce such microstructures in large volumes.

This changed dramatically when new devices became available for severe deformation processing, the most popular of which is undoubtedly the process of equal-channel angular pressing [74-77]. These newly developed processes have received great interest from researchers worldwide over the past decade due to their ability to produce relatively large volumes of submicrocrystalline materials. Ultrafine-grained materials possess unusual and extraordinary mechanical and physical properties, such as a high strength and toughness at room temperature [e.g. 16,25,42], or low-temperature, high-strain rate superplastic behaviour [e.g. 48,58,59].

Research in this area has concentrated mainly on the processing conditions and on the microstructure and the properties after processing, while little attention has been payed to the microstructural and mechanical behaviour during processing. Additionally, surprisingly few studies are aimed at determining the mechanism of formation of submicrocrystalline grains during severe deformation [7,19,28,40,50,65,87]. As far as the materials are concerned, the bulk of the experiments have been conducted on aluminium, titanium and their alloys, whereas a very small number deals with severe deformation of steel. The steels that were tested comprise only interstitial-free steels [7,8] and low-carbon steels [63,79-85], both materials with a (very) small fraction of a second phase.

Recent research has shown that submicrocrystalline materials possess a very high yield and ultimate strength, but lack sufficient strain hardening [e.g. 3,23,45]. One method to increase the strain hardening is to use a duplex microstructure [e.g. 39,72,96]. Hence, it is the purpose of this study to investigate how such a duplex microstructure, which is predominantly eutectoid, evolves during severe deformation and to assess the effects on the mechanical properties during processing. The materials under investigation are three high-carbon steels that are processed by means of equal-channel angular pressing at an elevated temperature.

This report is built up as follows. Chapter 2 deals with the theoretical background of this report. Details are presented on the mechanism of formation of submicrocrystalline structures, on the process of equal-channel angular pressing and on the results that are generally obtained using this process. In addition, the technique of electron backscattered diffraction will be elaborated. This sophisticated technique is one of the main techniques that are used for this study. This report continues with a description of the experimental procedures in chapter 3, while the findings are presented and discussed in chapter 4. The latter chapter includes the results of the scanning electron microscopy, the electron backscattered diffraction analysis and the mechanical properties. Finally, conclusions are drawn in chapter 5 and recommendations for future research are given in chapter 6.

CHAPTER 2

BACKGROUND

2.1 INTRODUCTION

One of the most important topics, if not the most important topic, in metals industry is the search for metals with a higher strength-to-weight ratio. Several strengthening methods are conventionally applied in order to obtain these enhanced properties, including solid solution strengthening, strengthening by introducing a second phase, precipitation hardening and grain refinement. Out of these strengthening methods, the reduction of the grain size is considered the most effective, since this is the only method that has the advantage of greatly increasing both the strength and the fracture resistance. Moreover, grain refinement hardly has a deteriorating effect on ductility and weldability, whereas the other strengthening methods have the disadvantage of an unavoidable reduction of the ductility and/or the weldability, although considerable strengthening of the material can be achieved.

Unsurprisingly, ultrafine-grained or submicrocrystalline materials have been known for several decades along with several techniques to produce them. Gas condensation [20,21] or ball milling with subsequent consolidation of nanopowders [46,47] have been the prime sources of ultrafine-grained materials. Other processes, such as rolling and extrusion to very high reductions also have a small share. Although these processes are capable of introducing submicrocrystalline grains in various materials, their major disadvantages are that such grain sizes can only be produced in small volumes and that relatively complicated processing routes are required. Another important disadvantage of these processes is that they result in nanoporous materials. This nanoporosity is the cause of a deterioration of the mechanical properties. Consequently, this class of materials received little attention and the existing few commercial applications were limited to niche markets. In the last decade, however, the interest in the production of submicrocrystalline materials has greatly augmented. The increased popularity is caused by new techniques that were especially developed for the purpose of introducing ultrafine grain sizes, i.e. average grain diameters of less than 2 μm, in polycrystalline materials by means of severe deformation and that have overcome the disadvantages of the conventional processes to obtain ultrafine-grained materials. These techniques include equal-channel angular pressing (ECAP) [74-77], accumulative roll-bonding (ARB) [70,71] and severe plastic torsional straining (SPTS) [97,98].

The reasons for the increased attention to severe deformation processing is that these new techniques have overcome the disadvantages of the conventional techniques. Furthermore, the

main advantage of the new techniques is their ability to attain levels of deformation that greatly exceed those of the conventional techniques. Strains as high as 10 can be easily achieved, unlike the conventional techniques where strains in the order of magnitude of 5 are considered extremely high. As a consequence, the average grain diameter is greatly reduced and the strength is greatly increased, thereby decreasing the importance of additional alloying treatments with strengthening and grain refining elements. The grain sizes that can be achieved using these new techniques are typically (well) below 1 μm. Finally, there is the possibility of scaling to industry-sized machines for the production of bulk submicrocrystalline materials. Equal-channel angular pressing and accumulative roll-bonding are the only techniques among the severe deformation processing techniques that offer the possibility of scaling. Although the other techniques are well capable of introducing submicrocrystalline grains, they are solely used for conducting laboratory scale experiments on small specimens and they are not capable of processing bulk submicrocrystalline materials.

In this chapter, background information will be given about the metallurgical fundamentals, the processing technique and one of the analysis techniques that were used for this investigation. The mechanisms of the formation of submicrocrystalline grains by means of severe deformation will be discussed in the section 2.2. The process of equal-channel angular pressing was used for the severe deformation. Details of the principles, the process parameters and the processing route of this process will be given in the section 2.3. This chapter is concluded with a brief discussion of electron backscattered diffraction, which is one of the techniques that were used for the analysis of the materials.

2.2 FORMATION OF SUBMICROCRYSTALLINE GRAINS

For the past decades, heavy deformation conducted at low temperatures, for instance cold rolling or drawing, is known to produce considerable grain refinement. The essential difference between conventional deformation techniques and severe deformation techniques is the level of deformation attained. Consequently, different mechanisms operate during deformation. Moreover, the structures that are formed during conventional deformation are of a cellular type, whereas the structures formed by severe deformation are of a granular type [100]. These cellular type structures consist mainly of low-angle boundaries (LAB's), while the granular type consists mainly of high-angle boundaries (HAB's). These high-angle boundary and granular type of structures can be realised through severe deformation processing, provided the deformation is carried out at temperatures that are low enough to prevent dynamic subgrain growth and dynamic recrystallisation from occurring. In this section, the mechanisms underlying the formation of submicrocrystalline grain structures are elaborated in detail.

The graph in figure 2.1 shows a typical course of the development of the microstructure during severe deformation processing. The boundary spacing and the percentage of high-angle grain boundary area are depicted in this graph as a function of the applied deformation for an

Al-0.13%Mg alloy and an interstitial-free (IF) steel. The data have been obtained from high-resolution electron backscattered diffraction (EBSD) maps of the transverse and longitudinal direction of the specimens deformed at the same homologous temperature (i.e. the temperature relative to the melting temperature) of $0.3 \cdot T_m$ to an effective strain of ten.

It is apparent from these two graphs that both materials behaved similarly, although the rate of microstructural evolution was different. It can be observed that the initial grain dimensions decrease rapidly with increasing strain, but as the strain increases the rate of decrease progressively diminishes and at very high strains converges to the subgrain width. The same tendency is shown by the fraction of high-angle boundaries with respect to the total length of the boundaries. Initially, the percentage of high-angle boundaries increases rapidly with increasing strain, but at an effective strain of approximately six the percentage of high-angle boundaries approaches an upper limit and eventually approaches a value that is typically around 80% [7,8,18,65]. The separation of the low-angle boundaries revealed a similar though opposite effect. Notice that in the initial stage the grain length is much larger than the grain width, which is consistent with the formation of a lamellae structure in the early stage of deformation. In the final stage, however, both dimensions equal the subgrain size and the percentage of high-angle boundaries has greatly augmented, meaning the initial grains have subdivided into smaller grains that are separated by

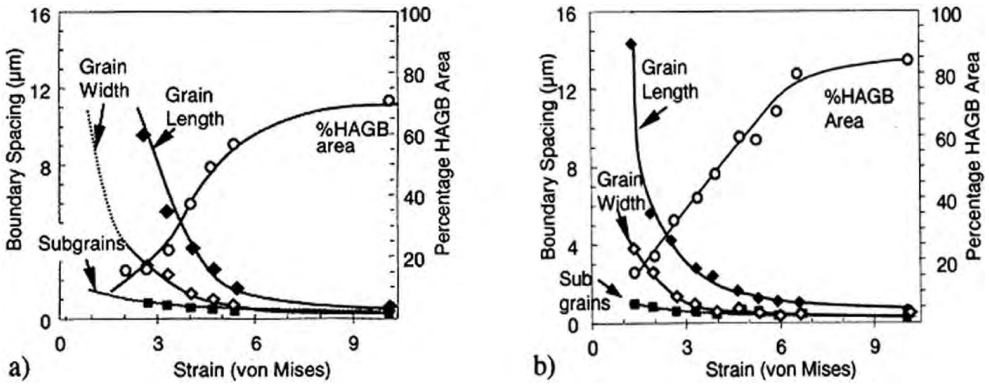

Figure 2.1. Grain dimensions, subgrain dimensions and percentage of high-angle grain boundary area, as measured from orientation image maps, as a function of the effective deformation for (a) an Al-0.13% Mg alloy and (b) an interstitial-free steel, as processed by equal-channel angular pressing at a temperature of 20 °C (293 K) and 500 °C (773 K), respectively. [7,8]

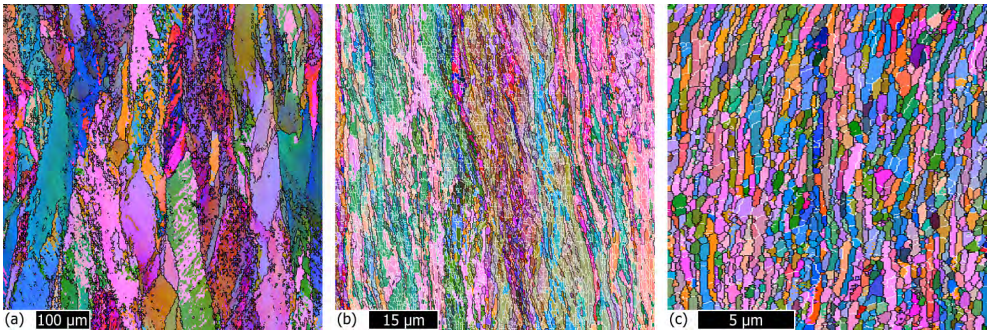

Figure 2.2. Orientation image maps of a titanium micro-alloyed interstitial-free steel after an effective deformation of (a) ε_{eff} = 1.33, (b) ε_{eff} = 3.33 and (c) ε_{eff} = 10.00. Low-angle boundaries ($\theta < 15°$) are indicated as white lines (omitted in (a)) and high-angle boundaries ($\theta > 15°$) as black lines. [7]

high-angle boundaries. This can be observed in figure 2.2 which shows orientation image maps of the microstructure at different strains. The fraction of high-angle boundaries, here indicated by the thin black lines, shows a clear and considerable increase.

The analysis of microstructures [7,8,65,81] and textures [28,81,83] revealed that subgrains tend to align to the shear direction as deformation progresses, thereby forming a lamellar microstructure. In the early stages of deformation a typical deformation microstructure is formed. This microstructure is characterised by intersecting microbands and the formation of dislocation cells and cell blocks that are bounded by these microbands. This stage in the deformation process can be seen in figure 2.3. Figure 2.4 depicts the next stage in the deformation process. As the deformation progresses, the grain shape changes to a lamellae structure that is both crystallographically and morphologically textured. The evolution of the microstructure during severe deformation can therefore be summarised by the following processes:

(1) Subdivision of the original grains;
(2) Formation and increasing volume fraction of high-angle boundaries;
(3) Formation of a crystallographically and morphologically textured microstructure.

These observations have been observed by different authors [7,8,14,15,28,49,65,83] and in different materials. A detailed analysis of the evolution of the microstructure that leads to the formation of ultrafine grains was conducted by Prangnell et al [65]. They distinguished four different stages in the evolution:

(1) Low strains ($\varepsilon_{eff} \leq 2$)
In the very first stage of deformation, the original grains subdivide on up to four different scales. An illustration of the different scales in the microstructural development of the grains at this level of deformation is depicted in figure 2.3a. The coarsest scale exhibits the formation of primary deformation bands (microbands) in such a manner that they subdivide the original grains into smaller segments [65]. On a finer scale, regular layers of aligned

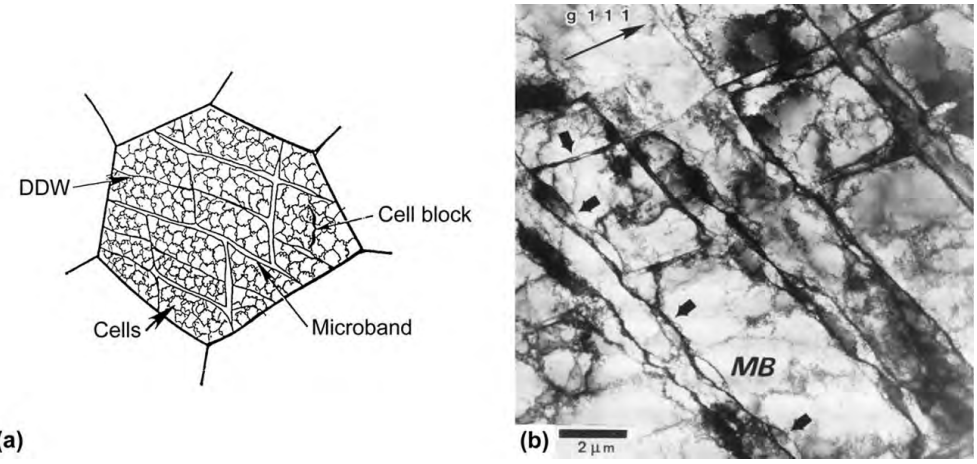

Figure 2.3. Schematic drawing and transmission electron micrograph of the deformation microstructure and grain subdivision at small to medium strain deformation. (a) Microbands (MB's) occur along with dense dislocation walls (DDW's) surrounding dislocation cells and cell blocks. (b) Nickel deformed in torsion to ε_{eff} = 3.5. The small arrows indicate microbands, whereas the large arrow indicates the direction of shear. [13,28]

cell blocks are formed [65] that are frequently bounded by the primary deformation bands and dense dislocation walls. At a finer scale, it can be observed that incidental dislocation boundaries within the cell blocks are formed, thereby forming dislocation cells [4,65]. A characteristic microstructural feature in this stage of deformation is that the layers and the cell blocks within the layers are oriented roughly perpendicular with respect to each other [65], as can be observed in transmission electron micrograph of figure 2.3b. Furthermore, the misorientation between the cell block layers are mostly low-angled in nature, but with increasing deformation the misorientation slowly increases. The fraction high-angle boundaries is, however, still small in this strain range;

(2) Low to medium strains ($2 < \varepsilon_{eff} \leq 4$)
Grain subdivision continues in the second deformation regime, leading to the formation of a lamellar microstructure and a further increase of the fraction of high-angle boundaries. The existing and newly formed lamellae become progressively more aligned to the shear direction [7,8,28,65], thereby forming a textured microstructure, similar to that observed during rolling to comparable strain levels [7,8,28,65,76]. The schematic drawing and the transmission electron micrograph in figure 2.4 depict the situation during this stage in the evolution of the microstructure. In this stage, the grains have a relatively large length and small width, which corresponds to the formation of a "fibrous microstructure" [65]. As the lamellae rotate towards the shear direction and thus towards their final orientation, new high-angle boundaries are formed. Simultaneously, the lamellae are subdivided by transverse bands, thus reducing the grain length. However, it appears that a more unstable orientation (relative to the deformation direction) promotes both the formation of new high-angle boundaries and the subdivision of the lamellae [7,8]. This results in a rather inhomogeneous formation of the high-angle boundaries and, therefore, in a final distribution revealing large local variations in the fraction high-angle boundaries. This can be observed in figure 2.2b, which shows areas with a relatively low and relatively high fraction of high-angle boundaries;

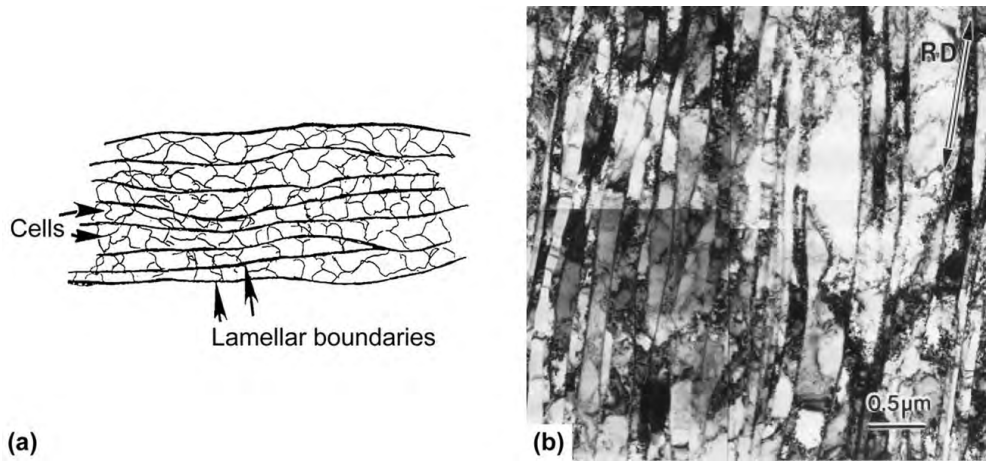

Figure 2.4. Schematic drawing and transmission electron micrograph of the deformation microstructure at medium to large strain deformation. (a) and (b) lamellar and microtextured structure. The material and the extent and mode of deformation are unknown. RD indicates the rolling direction. [13,28]

(3) Medium to high strains ($4 < \varepsilon_{eff} \leq 6$)

The microstructural evolution in this stage of deformation is characterised by a gradual decrease of the average lamellar width. This decrease continues until the lamellar width approaches one subgrain width at the end of this strain range. Simultaneously, new high-angle boundaries are formed at a low rate that is again dependent upon the orientation of the grain. These two processes lead to the formation of high aspect-ratio grains, i.e. grains with a large length and a small width, that differ in length, thus reflecting the original stability. The grains are linked to each other in such a manner that they give the appearance of "ribbons" [65]. The processes mentioned here are consistent with the observations from figure 2.1, where it can be seen that the grain width shows very little decrease, while the rate of decrease of the grain length still diminishes;

(4) Ultrahigh strains ($\varepsilon_{eff} > 6$)

In the final regime, the lamellae structure is further refined by the subdivision of the long "ribbon" grains into shorter grains, until at strains of more than ten a relatively homogeneous microstructure of submicrocrystalline grains is formed, as can be observed in figure 2.2c. This corresponds to a decrease in grain length and no change in grain width (see figure 2.1). Consequently, it can be observed that during this stage the volume fraction of submicrocrystalline grains increases rapidly, thereby enhancing the homogeneity of the microstructure.

It should be noted that the strain intervals mentioned should be regarded as indications, since they may vary for different materials. In addition, although this description of the deformation stages is derived from research on equal-channel angular pressing, several other researchers found the same results using other severe deformation techniques and materials [28,57].

In addition to the basic mechanism that is described here, there are several other factors that affect the final microstructural and mechanical properties of severely deformed materials. These include the crystal structure, the stacking fault energy and the number of active slip systems. These parameters determine the rate of development of the microstructure and the texture during processing as well as the microstructural homogeneity and the grain size after processing [99].

Another topic that has drawn the attention of researchers who are involved in ECAP-processing is the effect of the stacking-fault energy (SFE). In general, it can be said that low stacking fault energies, i.e. values of less than 100 $mJ \cdot m^{-2}$ [68], cause low rates of recovery, lower rates of grain growth during annealing and possess, therefore, a higher thermal stability. From a microstructural point of view, low stacking-fault energy materials prefer to deform by twinning and they have a small grain size after processing. Yet they possess a rather broad grain size distribution even at very high strains. On the other hand, high stacking-fault energy materials exhibit higher rates of recovery, higher rates of grain growth (less thermal stability) and prefer to deform by slip. However, their average grain size is fully homogeneous even at conventionally high strains [49,98]. It is apparent from figure 2.1 and figure 2.2 that the rate of evolution of the microstructure during severe plastic deformation differed for a face-centred cubic (FCC) aluminium-magnesium alloy and a body-centred cubic (BCC) interstitial-free steel. Bowen et al [7,8]

reported that a homogeneous microstructure of submicrocrystalline grains was achieved in the latter material, which appeared to be finer and to exhibit less grain growth than the aluminium-magnesium alloy. The body-centred cubic steel also exhibited superior properties as compared to the face-centred cubic aluminium alloy.

An important feature is the number of active slip systems, i.e. the planes and directions in which dislocations move through the lattice. The crystal structure determines the number of potentially active systems, whereas the stacking fault energy and the geometric constraints determine whether the slip or twinning system is activated [32,99]. For bulk polycrystalline materials, each grain is constrained by its neighbours [99]. Body-centred cubic metals have in general many potentially active systems (24 at most) and hence prefer to deform by slip. The primary slip direction in bcc metals is <111> and the primary plane is either the {110}-plane or the {112}-plane or the {123}-plane. Microalloyed to low-alloyed ferritic steels have a bcc structure and are therefore expected to be less affected by the crystal structure and the inherent number of active slip systems than fcc metals and alloys are.

The number and nature of the slip systems that are operating during equal-channel angular pressing were investigated by Shin et al [83] for a plain low-carbon steel. They concluded that in the initial stage of extrusion both the {110}<111> and the {112}<111> slip systems were operating and that these family of systems caused the formation of submicrometre-sized ferrite grains that are enclosed by serrated and low-angle boundaries. During further deformation, the initially formed shear bands prohibited the dislocations on other slip systems from crossing the bands. This resulted in the activation of all of the possible slip systems belonging to the {110}<111> and the {112}<111> slip systems family and in the formation of submicrometre-sized dislocation cells that are bounded by the {112} and the {110} planes.

A further and more detailed description of the mechanism of formation of submicrocrystalline structures in ferritic steels and the factors affecting this, can be found in the literature review by Reinier Bergwerf [6] and the PhD-thesis by Jake Bowen [7].

2.3 EQUAL-CHANNEL ANGULAR PRESSING

One of the most popular techniques that are used for the production of polycrystalline materials with a grain diameter in the submicrometre range is equal-channel angular pressing (ECAP), or equal-channel angular extrusion (ECAE) as it is named alternatively. This process was originally developed by V. M. Segal and his colleagues in the former Soviet Union in the late 1970's [74,75]. Following the collapse of the Soviet Union, Segal moved to Texas to work at Texas A&M University, where he improved and patented this technique [76-78]. Since then, this process has received considerable attention for three reasons: (1) ECAP has the capability of introducing ultrafine grains in the submicrometre range into both coarse- and fine-grained polycrystalline materials, (2) ECAP is a relatively simple process compared to the conventional processes for the production of submicrocrystalline grains and (3) ECAP has the possibility of scaling to industry-sized machines.

In this section, the process of equal-channel angular pressing will be elaborated in detail. In the first part, the construction of the equal-channel angular press will be discussed and in the second part, the characteristics of this process will be discussed. For the purpose of clarity, brief comparisons with conventional extrusion will be made.

The construction of the die of ECAP is illustrated in figure 2.5. The process of equal-channel angular pressing involves pressing a billet through a die, consisting of two channels of identical shape and cross-sectional dimension that are positioned under a predetermined angle Φ and an additional angle of Ψ that defines the arc of curvature at the outer point of intersection of the two channels [35,76 - 78]. The sole purpose of the corner angle is to facilitate the extrusion process. Typical channel angles are 90° and 120°, whereas typical corner angles are in the range of 0 ° to 30 °. An orthogonal system of three axes is introduced with respect to the billet, as indicated in figure 2.5. These are (1) the pressing direction, which is the direction in which the billet moves, (2) the width direction, which is the direction as measured from the inner to the outer surface of the die channel, and (3) the thickness direction, which runs perpendicular to the other two directions, thereby exiting the plane of the paper. The thickness direction is not indicated in figure 2.5. As the billet is extruded through the die, it is deformed at the point of intersection of the two channels along the shear plane indicated by the two dashed lines (for the case of a non-zero corner angle). If a corner angle of ψ = 0° is used, the shear plane is stationary, whereas if non-zero angles are used the shear plane gradually rotates, following the shape of the corner. Under ideal circumstances, where die friction, strain hardening and strain rate sensitivity do not

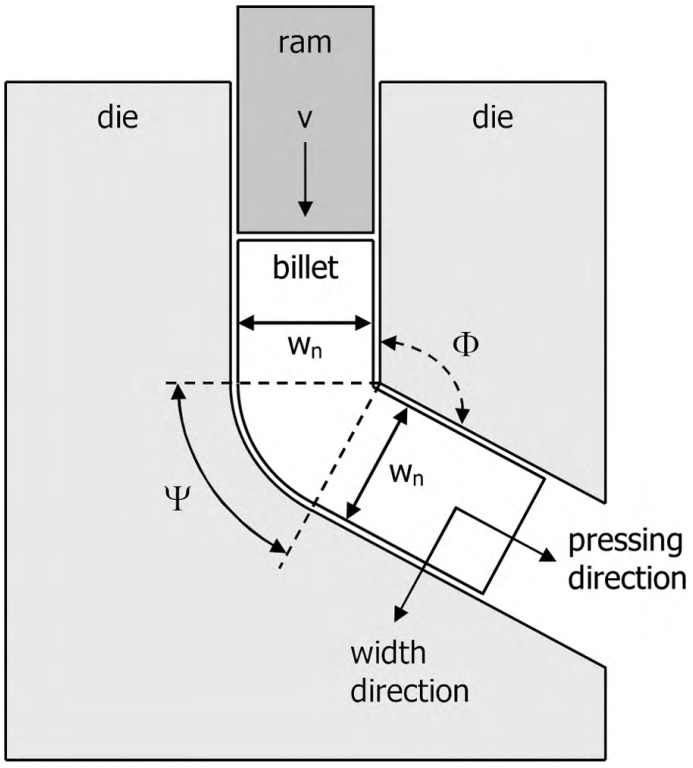

Figure 2.5. Schematic illustration of the construction of a die for equal-channel angular pressing (ECAP). v is the ram velocity, w_n is the width of the specimen during the n^{th} extrusion cycle, Φ is the channel angle and ψ is the corner angle.

occur, the deformation mode would be simple plane shear strain [8,43], as is the case with torsion. Under real conditions however, die friction, strain hardening and strain rate sensitivity affect plastic flow [8,43]. In addition, plastic flow of the billet does not follow the sharp angle of intersection of the two channels (Ψ = 0°), instead it tends to round off a bit [8,43] (see figure 2.6b). Therefore, real ECAP dies have a small angle of curvature in the outer corner (Ψ > 0°). This implies, however, that the shear plane gradually moves from the upper dashed line to the lower dashed line, as illustrated in figure 2.5. The unique feature of ECAP, which distinguishes this process from other deformation processes, such as rolling or torsion, is that the deformation is very homogeneous and occurs at or in the immediate vicinity of the shear plane [43]. Since the strain in the thickness direction is zero, the deformation is two-dimensional and therefore involves nearly simple plane shear strain [43,76,77].

When comparing the construction of the die for equal-channel angular pressing with that for conventional extrusion, the essential difference is that the cross-sectional shape and dimension remain the same for the inlet and the outlet channel of the equal-channel angular press. On the other hand, there is a drastic change in the shape and dimension between the "inlet channel" (i.e. the die) and the "outlet channel" (i.e. the die opening) of a conventional extruder as is illustrated in figure 2.7. It is because of this difference that deformation by means of conven-

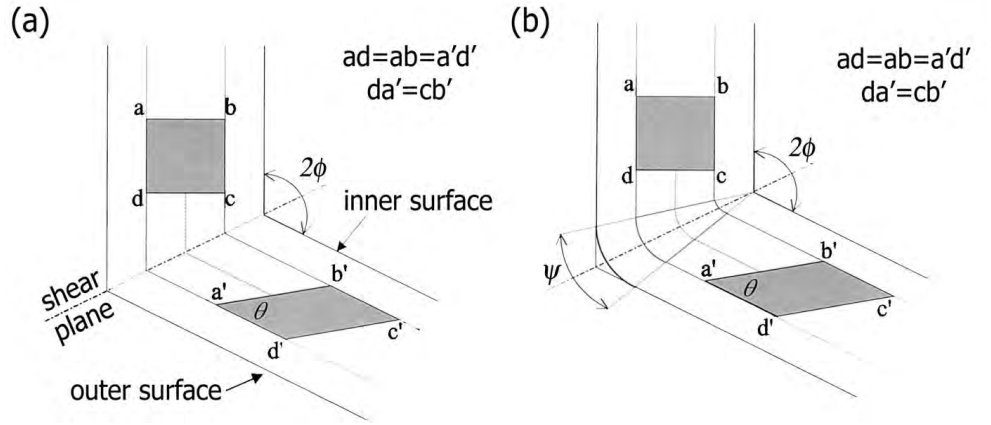

Figure 2.6. Schematic illustration of the shearing characteristics associated with the ECAP using (a) a sharp corner angle (Ψ = 0°) and (b) a curved corner angle (Ψ > 0°). The symbol Φ denotes the angle of intersection of the two dies and the symbol Ψ denotes the angle of curvature of the corner. [9,43]

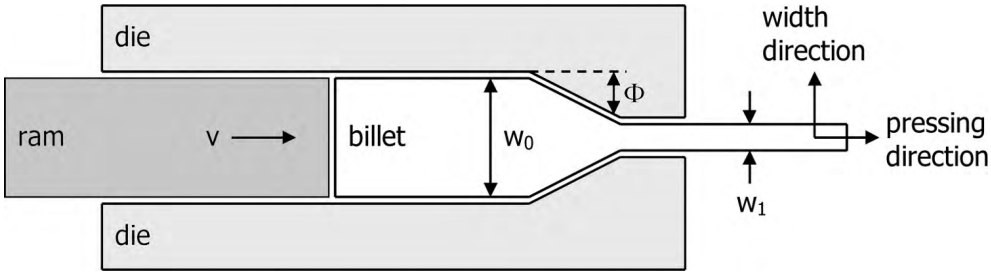

Figure 2.7. Construction of the die for conventional forward extrusion. V denotes the ram velocity, w_0 the initial thickness of the billet, w_1 the thickness of the billet after processing and Φ the angle of inclination of the die near the die opening.

tion extrusion can only be applied once. On the other hand, it is in theory possible to conduct an infinite number of pressings on a material when using equal-channel angular pressing. Hence, the total effective deformation equals the deformation of the single pressing in the case of conventional extrusion and the accumulated deformation per pressing in the case of equal-channel angular pressing:

Conventional extrusion: $\varepsilon_{tot} = \varepsilon_1$
Equal-channel angular pressing: $\varepsilon_{tot} = \varepsilon_1 + \varepsilon_2 + ... + \varepsilon_n = n \cdot \varepsilon_i$

The strain introduced in a single passage through the die of an equal-channel angular press may be estimated from a simple relationship that incorporates the individual values of Φ and Ψ [35,77]. Under ideal conditions [43] and using a corner angle of Ψ = 0° the shear strain (γ) is given by the following equation [43,78]:

$$\gamma = 2 \cdot \cot(\tfrac{1}{2}\Phi) \tag{2.1}$$

Under actual conditions, this equation should be modified to incorporate the effect of the corner angle on the shear strain [35,43]. The shear strain in the billet after a single pass can then be calculated from the following equation [35,56]:

$$\gamma = 2 \cdot \cot(\tfrac{1}{2}\Psi + \tfrac{1}{2}\Phi) + \Psi \cdot \mathrm{cosec}(\tfrac{1}{2}\Psi + \tfrac{1}{2}\Phi) \tag{2.2}$$

The Von Mises effective shear strain (ε_{eff}), or equivalent strain as it is named alternatively, can be calculated easily by dividing the shear strain (γ) by the square root of three. In the case of multi-pass extrusion, one simply multiplies the effective strain in a single pass by the number of passes (N), yielding the following equation:

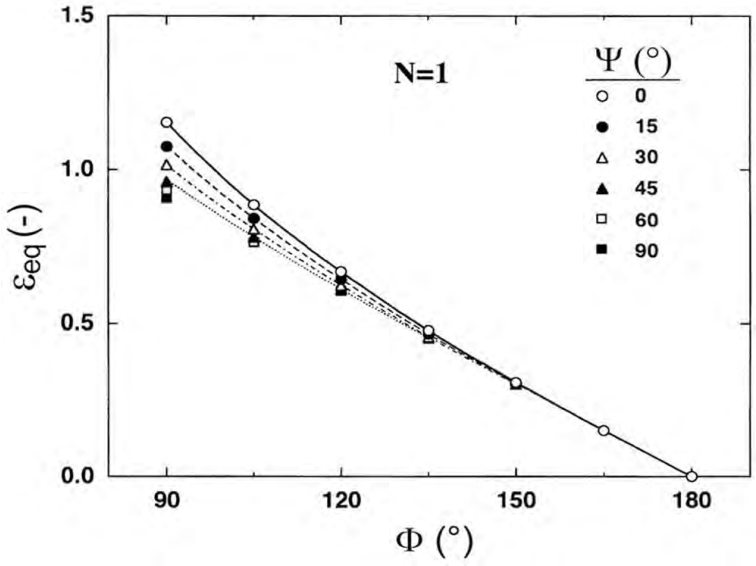

Figure 2.8. Equivalent strain (ε_{eq}) versus channel angle (Φ) for different corner angles (Ψ). [60]

$$\varepsilon_{eff} = \frac{N}{\sqrt{3}} \cdot (2 \cdot \cot(\tfrac{1}{2}\Psi + \tfrac{1}{2}\Phi) + \Psi \cdot \mathrm{cosec}(\tfrac{1}{2}\Psi + \tfrac{1}{2}\Phi)) \qquad (2.3)$$

The validity of this relationship has been demonstrated in model experiments [93]. According to equation 2.3, the equivalent strain in a single pass decreases with increasing channel angle and with increasing corner angle. Figure 2.8 depicts how the equivalent strain develops according to equation 2.3 for different channel and corner angles. Using equation 2.3, it can be shown that the equivalent strain per pass during ECAP decreases from its maximum of $\varepsilon_{eff} = 1.15$ at $\Phi = 90°$ and $\Psi = 0°$ to its minimum of $\varepsilon_{eff} = 0$ at $\Phi = 180°$ and $\Psi = 0°$. The effect of different channel and corner angles on the equivalent strain per pass and thus on the grain refinement has been demonstrated experimentally by Nakashima et al [60]. Later on, these results were confirmed theoretically by finite element analysis of the billet deformation behaviour by Kim et al [43,44]. They demonstrated that a curved corner decreases the equivalent strain and results in inhomogeneous plastic flow. Additionally, it is apparent that the channel angle has more effect on the strain generated during ECAP than the corner angle.

One of the advantages of this process is therefore that with a small number of passes a relatively large effective strain can be accomplished. In addition, ECAP offers some flexibility in the development of different microstructures and textures [77,78]. Moreover, it is possible to partially control the microstructural development, something that is impossible when using rolling for instance. Segal [77] first demonstrated that applying multiple extrusion passes may provide an opportunity to develop different microstructures by rotating the sample between consecutive pressings, thereby modifying the shear planes and shear directions. Several authors [17,35] have demonstrated the principle of billet rotation and it is clear from their results that the microstructural characteristics, in particular the microstructural evolution during ECAP, depend on the precise processing conditions, hence on the shearing characteristics in each passage through the die. The nature of shearing under different pressing conditions has been the topic of several investigations [14,17,18,36-38]. It is apparent from these papers that different routes lead to different microstructures.

A detailed description of the different processing routes in ECAP has been given by Furukawa et al [17] and Zhu et al [99]. They distinguished four different processing routes, which they designated routes A, B_A, B_C and C. Figure 2.9 schematically illustrates for each route how the billet

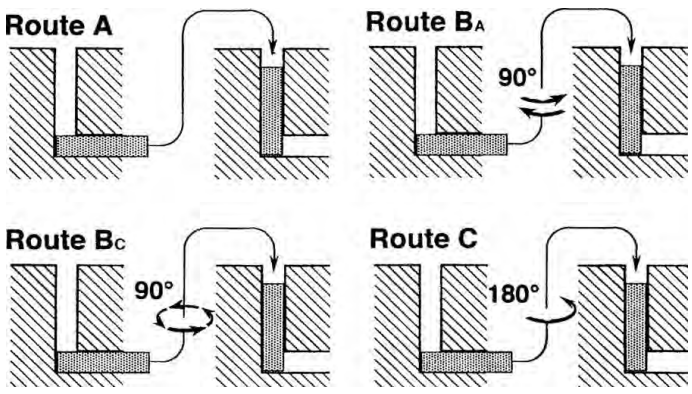

Figure 2.9. Rotation schemes for the four most commonly applied routes in ECAP. [100]

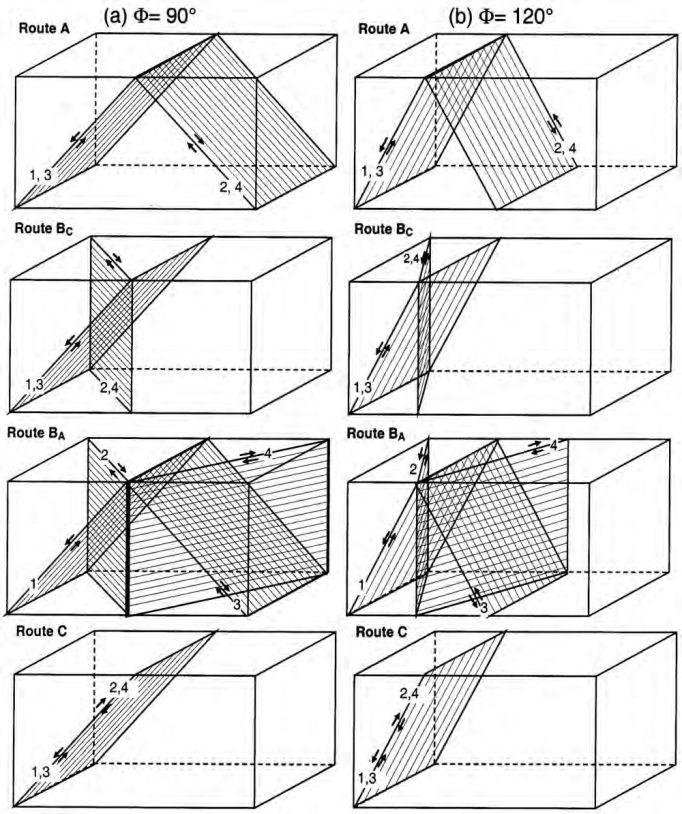

Figure 2.10. Planes of shear deformation during the first four extrusion cycles in equal-channel angular extrusion (ECAP) for four different routes under a channel angle of (a) Φ = 90 ° and (b) Φ = 120 °. [100]

Table 2.1. Shearing characteristics of the four commonly applied routes during processing by means of equal-channel angular pressing. [17,24]

Route	Plane	Number of pressings								
		0	1	2	3	4	5	6	7	8
A	X	□	▭	▭	▭	▭	▭	▭	—	—
	Y	□	▱	▱	▱	▱	▱	▱	▱	▱
	Z	□	□	□	□	□	□	□	□	□
B_A	X	□	▭	▯	╲	▯	╲	▯	╲	╱
	Y	□	▱	▱	▱	▱	▱	▱	▱	▱
	Z	□	□	▱	▱	▱	▱	▱	▱	▱
B_C	X	□	▭	▯	▯	□	▭	▯	▯	□
	Y	□	▱	▱	□	□	▱	▱	□	□
	Z	□	□	▱	▱	□	□	▱	▱	□
C	X	□	▭	□	▭	□	▭	□	▭	□
	Y	□	▱	□	▱	□	▱	□	▱	□
	Z	□	□	□	□	□	□	□	□	□

is rotated in between consecutive passes. When using route A the billet is extruded in several consecutive cycles without rotation of the billet, whereas using route B the billet is rotated 90 ° along its longitudinal axis (i.e. the extrusion direction) in between the cycles. Route B can be subdivided into two different routes, namely route B_A, where the rotations occur in alternate directions, and route B_C, where the billet is rotated in a single direction. The fourth route, route C, involves a 180 ° rotation of the billet in between the cycles. Since each rotation of the billet activates different slip systems [17], different microstructures may develop. Figure 2.10 shows the active shear planes associated with these four different processing routes for multipass extrusion through two dies with different channel angle. It is apparent from this figure that for route C shear deformation occurs along a single plane, whereas for route A and route B_C there are two distinct shear planes and for route B_A there are four distinct shear planes.

The effect of the different shear planes on the deformation can be visualised schematically by the extrusion of a cubic billet through a die having a channel angle of $\Phi = 90°$ and a corner angle of $\Psi = 0°$. This is illustrated in table 2.1, where for each route the distortion of the X-, Y- and Z-plane of the billet is depicted for the first eight passes through the die. The X-plane is here defined as the plane perpendicular to the extrusion direction, the Y-plane as the plane perpendicular to the thickness direction and, finally, the Z-plane as the plane perpendicular to the width direction [17]. It can be observed that using route A or route B_A, all planes are deformed in a single direction. Initially, there were some contradictions [14,17,18,37,62] as to the effectiveness of the routes in refining the grain size. For instance, several researchers [17] used a die with a channel angle of $\Phi = 90°$ and found that routes B_C and C are more effective than routes A and B_A, because the cubic element is restored after each 4N passes in route B_C and each 2N passes in route C, while routes A and B_A deform the cubic element continuously. Nevertheless, different results were found by Gholinia et al [18] who used a die with a channel angle of $\Phi = 120°$. They demonstrated that the most effective method of forming a submicrocrystalline structure by severe deformation is to maintain a constant strain path. Therefore, route A is most effective, whereas route B_A and route B_C have an intermediate effectiveness and route C is the least effective in grain refinement. From the work published on this topic, Zhu and Lowe [100] concluded that grain refinement during the ECAP process is affected by both the accumulated strain and the interaction of geometrical constraints with the crystal structure that determine which slip or twinning system is activated.

Research by Berbon et al [5] has pointed out that the pressing speed during ECAP-deformation of pure Al and Al-1%Mg has no significant effect on the equilibrium grain size. However, it appeared that the effect of recovery on the microstructural evolution is more evident at lower pressing speeds. They found from transmission electron microscopy that at lower pressing rate the grains and grain boundaries contained more extrinsic dislocations than at higher pressing rate and concluded therefore that the additional time available at lower pressing speeds permits the establishment of more equilibrated microstructures. Additionally, a higher proportion of dislocations become absorbed in the grain boundaries, due to lower pressing speeds.

Another topic within the area of ECAP-processing that has found very little attention is the effect of the processing temperature on the microstructure both during and after processing. Equal-channel angular pressing is frequently conducted at elevated temperatures to facilitate extrusion. Especially when hard materials are to be extruded, the pressure needed to deform a

material may sometimes exceed the maximum pressure that can be supplied by the extrusion machine. Hence, the use of elevated temperatures is unavoidable to lower the ram pressure, even though microstructural changes are possibly inevitable. Yamashita et al investigated the effect of the pressing temperature on the microstructural development during equal-channel angular pressing of pure and alloyed aluminium [94] and magnesium [95]. Their results revealed two characteristics. First, materials that were processed at elevated temperatures possess a larger grain size than those that were processed at room temperature. Second, the misorientation of the newly formed grain boundaries tends to be lower at elevated temperatures than at room temperature. Yamashita et al [94] explain the dominance of the low-angle boundaries at elevated processing temperatures by an increased rate of dislocation annihilations, which consequently limits the absorption of dislocations into cell walls. They suggest that the evolution of the microstructure into an array of high-angle boundaries is more difficult at the higher pressing temperatures, thereby favouring the retention of the subgrain structure to higher total strains in pure aluminium when the ECAP deformation temperature is increased [94].

The effect of the processing temperature on the microstructural development during equal-channel angular pressing has not been studied in steel. Therefore, no exact quantitative data can be given on this subject. However, research has revealed that the stacking fault energy of an Al-3%Mg alloy is only slightly smaller than that of a commercial low-carbon ferritic steel, approximately 90 $kJ \cdot mol^{-1}$ [88] and 106 $kJ \cdot mol^{-1}$ [81], respectively. It is therefore not unlikely that the same two characteristics described above can also be observed in this type of steels.

The processing route of materials through equal-channel angular pressing is rather simple. A typical processing route for ECAP-processing is given in figure 2.11. Here it is assumed that a hard material is going to be processed, which requires extrusion at elevated temperatures to facilitate the extrusion. Hence, one needs to heat up the billet to the deformation temperature and then hold it for a short time to allow the temperature of the billet to homogenise. Following the homogenisation, the billet is pressed through the die. In case the billet has cooled down too much in between the extrusion, reheating to the deformation temperature and homogenisation is required before subsequent pressings can be carried out. Care should be taken to prevent recrystallisation from occurring, since this would completely destroy the built-up of a dislocation structure that is needed to obtain an submicrocrystalline structure. In addition, recovery should be avoided or at least minimised as much as possible. After completion of the extrusion the billet is cooled down to room temperature.

Further information on the process of equal-channel angular pressing as well as on other severe deformation processes can be found in the literature review by Reinier Bergwerf [6], the PhD-thesis by Jake Bowen [7] and the review paper by Ruzlan Valiev [87].

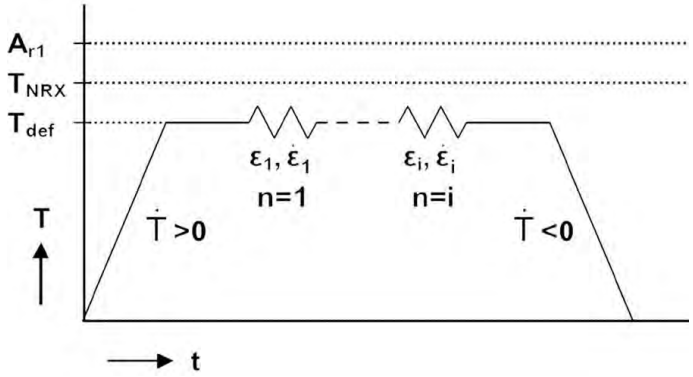

Figure 2.11. Typical processing route for equal-channel angular pressing.

2.4 ELECTRON BACKSCATTERED DIFFRACTION

Electron backscattered diffraction (EBSD) analysis, or electron backscattered pattern (EBSP) analysis as this technique is alternatively named, is nowadays a popular technique for the analysis of microtextures. Its main purpose is to provide crystallographic data on relatively large volumes of material. The use of electron backscattered diffraction analysis took a giant leap after the discovery in 1994 of a method to automatically analyse and index Kikuchi-patterns. The parallel development of faster computers, the availability of appropriate analysis programmes added to this major improvement. This not only enabled fully automated EBSD-analysis, but also greatly reduced the time required for the analysis and broadened the areas of application to include microtexture analysis, phase identification, deformation microstructures and grain statistics. With the development of the field emission gun, as a replacement for the thermo-ionic emission gun, the spatial resolution greatly augmented, thereby further enhancing the quality of the data. EBSD-analysis also benefits from other advantages, such as the relative ease of usage and the relatively low equipment costs.

The basic construction of a typical EBSD-system on a SEM is illustrated in figure 2.12. Crystallographic data is gathered by scanning a sample one volume element at the time with an electron beam in a scanning or transmission electron microscope. The electrons react with the atoms in the sample and diffract in a regular pattern. The diffraction pattern is then recorded on a CCD-camera, which in turn is linked to a computer. The signal from the CCD-camera is analysed by advanced computer software that rapidly calculates the orientation of the crystal at the point of measurement. The resulting data is usually presented graphically in an orientation image map.

Figure 2.13a exhibits the classical construction for diffraction at the planes of a crystal lattice and the formation of Kikuchi-lines. When an electron beam in an electron microscope is incident on a crystalline material, the electrons are diffusely scattered in all directions, thereby exhibiting a pattern of reinforced and extinct radiation. Peaks in the intensity of the diffracted electrons will occur for those conditions that satisfy Bragg's law:

$$n \cdot \lambda = 2 \cdot d_{hkl} \cdot \sin(\Theta_B) \tag{2.4}$$

where n is the order of the diffraction peak, λ is the wavelength of the incident beam, d_{hkl} is the distance between the atomic layers and Θ_B is the angle (Bragg-angle) under which the electron beam is reflected off the atomic planes. Since diffraction of the electrons through the Bragg angle occurs in all directions, the locus of the diffracted radiation is the surface of a cone, named a Kossel-cone, which extends about the normal of the reflecting atomic planes with half apex angle 90 - Θ_B. From substitution of typical values of the parameters in Bragg's law, it was found that the Bragg-angle Θ_B amounts roughly 0.5 °. Hence, the Kossel-cone has an apex angle of almost 180 °, i.e. it is nearly flat. In addition, the intercept of a Kossel-cone with a plane at short distance from the apex yields a curved line, but at a pseudo-infinite distance the intercept will appear as a straight line. The latter is the case when the diffracted electrons are recorded by the EBSD-camera. The lines that appear on the phosphor screen are named Kikuchi-lines. A Kikuchi-band always consist of two lines of different intensity and at an angular spacing of 2ΘB. This is shown in figure 2.13b, where the formation of the Kikuchi-bands is illustrated. The excess line is the brighter one and is formed by diffraction at the "frontside" of the lattice plane. The defect line is darker and is formed by diffraction on the "backside" of the lattice plane. In addition, two important characteristics of a Kikuchi-line include that it has a distinct width and that it corresponds to a distinct crystallographic plane. The width of a Kikuchi-line is related to the Bragg-angle of the corresponding lattice plane. Figure 2.14 shows two examples of Kikuchi-patterns as obtained from electron backscatter diffraction analysis of severely deformed eutectoid steel. Figure 2.14a clearly shows that each Kikuchi-line has a different width and orientation. An essential and characteristic feature are the numerous interceptions of the Kikuchi-lines. These are named zone-axes and are used to identify the lines and therefore the structure of the crystal.

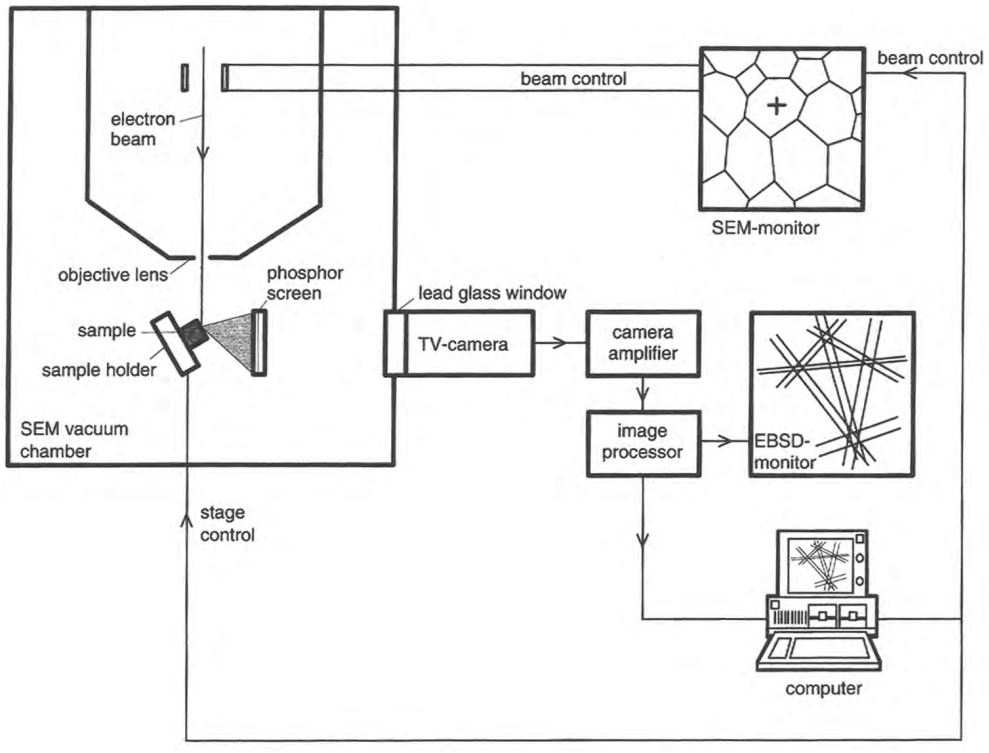

Figure 2.12. Illustration of the components in a typical system for EBSD-analysis. [67]

Since the Kikuchi-pattern incorporates both interzonal and interplanar angles, it implicitly contains the crystal symmetry.

Following the acquisition of the Kikuchi-patterns, the planes associated with a pair of lines have to be identified, after which the local orientation of the crystal with respect to the orientation of the sample can be determined. One of the major problems occurs during the identification of the pattern. The Kikuchi-bands often have a low contrast that hampers the indexation. Especially severely deformed materials can be rather cumbersome, since they contain an even higher fraction of low-contrast bands than non-deformed materials. The intensity of the Kikuchi-line depends on a number of factors:

(1) The type of electron microscope;
TEM's in general have a higher intensity than SEM's;
(2) The atomic weight of the sample material;
A higher atomic weight causes a higher intensity of the diffracted electrons, and;
(3) The angle of tilt of the sample;
Increasing the angle of tilt to 60-70° allows more electrons to be diffracted and detected.

Several methods have been developed to overcome this problem, including the Burns-algorithm [11,52,92] and the Hough-transform [26,34,51]. Nowadays the Hough-transform is the most frequently applied algorithm. The Hough-transform involves the transformation of the Kikuchi-bands in the original image into points in an accumulation space that is commonly named the Hough-space. Each point (x_i, y_i) in the original image (see figure 2.15a) is transformed into a sinusoidal curve in the accumulation space by selecting an interval of angles φ and calculating the corresponding values of ρ using the following equation:

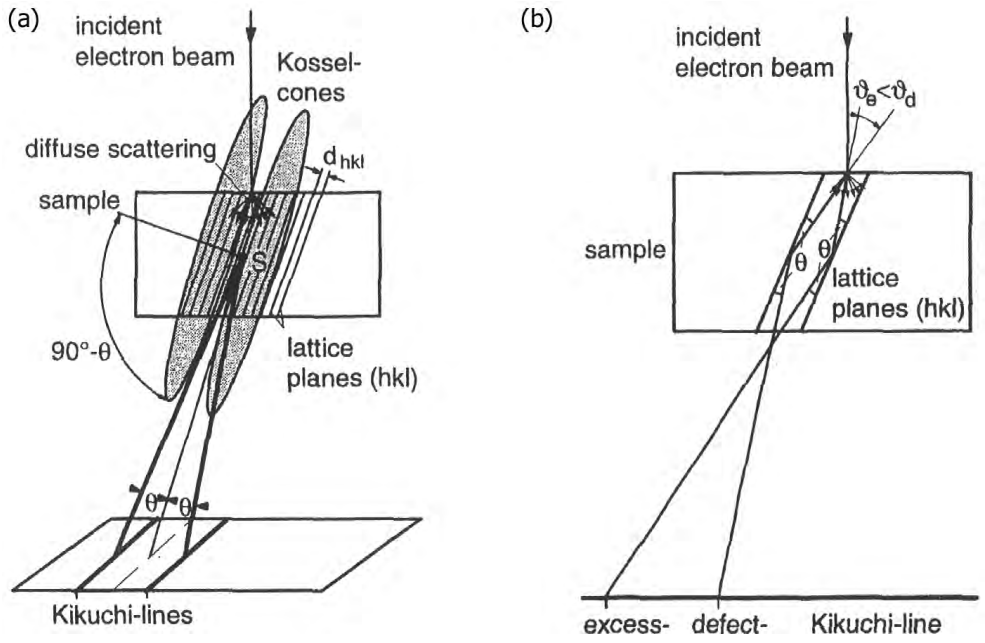

Figure 2.13. Origin of the Kikuchi-lines from electron beam diffraction on a crystalline sample. (a) Bragg diffraction at source S on lattice planes. (b) Formation of excess and defect Kikuchi-lines. [67]

$$\rho = x_i \cos\varphi + y_i \sin\varphi, \qquad \varphi \in [0°..180°], \qquad \rho \in R \tag{2.5}$$

In this equation, ρ is the perpendicular distance between the origin and the Kikuchi-line (ρ_1 and ρ_2 in figure 2.15a) that is positioned under an angle φ (φ_1 and φ_2 in figure 2.15a) with the x-axis. Each sinusoidal curve in Hough-space has the same intensity as its corresponding point (x_i, y_i) in the image-space and in the points of intersection of the curves the intensity adds up. Furthermore, all the curves of points on the same Kikuchi-line will intersect in the same point in Hough-space. Kikuchi-lines can be easily distinguished in Hough-space, even if they are of poor contrast, since they appear as bright spots flanked by two dark spots. The two dark spots derive from the dark edges of the Kikuchi-lines. The zone axis in the image-space which has the largest number of line intersections has the highest intensity in the Hough-space. For pattern indexation, the lines with the highest intensity are used to determine the local orientation. Unfortunately, frequently wrong lines are detected or ambiguous solutions are found of which the orientation cannot be determined. Figure 2.14b shows an example of a misindexed pattern, showing that the orientation of the index lines deviates from the orientation of the Kikuchi-lines.

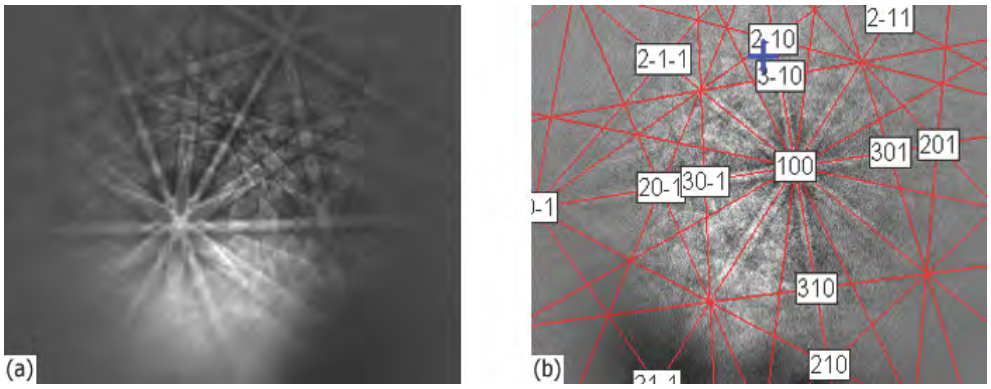

Figure 2.14. Examples of (a) a non-indexed and (b) an indexed Kikuchi-pattern of a severely deformed eutectoid steel as obtained from electron backscatter diffraction analysis in a scanning electron microscope. Note that the pattern in (b) is misindexed and does not correspond to the non-indexed pattern in (a).

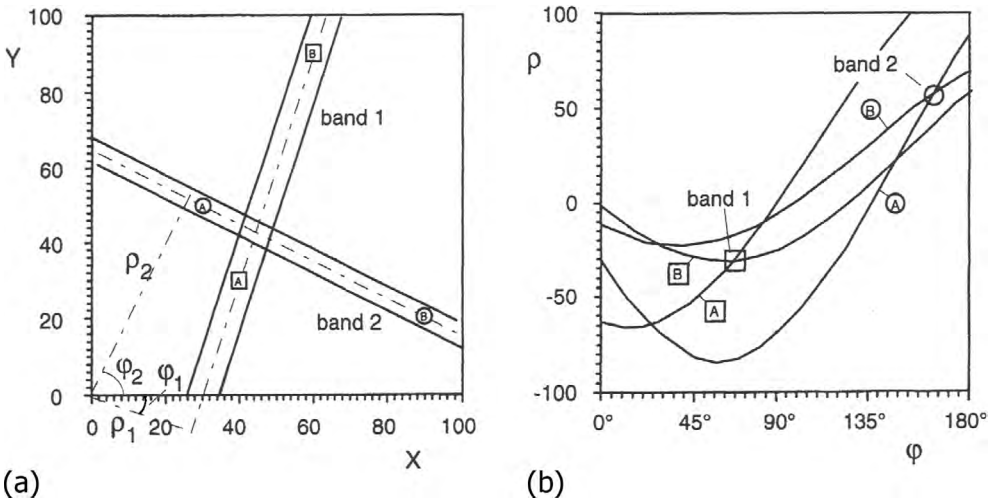

Figure 2.15. Schematic representation of the Hough-transform with (a) two Kikuchi-lines in the original image and (b) the two corresponding points in the Hough-space. [67]

The next step following the indexation of the pattern is the calculation of the orientation of the crystal lattice with respect to a fixed co-ordinate system, i.e. the specimen co-ordinate system. To do this, the three-dimensional co-ordinate system of the crystal lattice (C_C) needs to be related to the three-dimensional co-ordinate system of the specimen (C_S) via a rotation matrix (R) according to the expression:

$$C_C = R \cdot C_S \tag{2.6}$$

Where R is a square rotation matrix of the form:

$$R = \begin{vmatrix} r_{11} & r_{12} & r_{13} \\ r_{21} & r_{22} & r_{23} \\ r_{31} & r_{32} & r_{33} \end{vmatrix} \tag{2.7}$$

The coefficients of the rotation matrix can be calculated using Euler-angles, which involves rotation over three angles. The angles of rotation have been labelled differently over the years, but the Bunge-convention [10] is the one that is most frequently used. This convention is also adopted here, as is illustrated in figure 2.16. The three rotations are executed as follows:

(1) Rotate the co-ordinate system (X Y Z) around the Z-axis over an angle φ_1.
This yields the new co-ordinate system (X′ Y′ Z).
(2) Rotate the co-ordinate system (X′ Y′ Z) around the new X′-axis over an angle Φ.
This yields the new co-ordinate system (X′ Y″ Z′).
(3) Rotate the co-ordinate system (X′ Y″ Z′) around the new Z′-axis over an angle φ_2.
This yields the new co-ordinate system (X″ Y‴ Z′).

Matrix R is formed from the three Euler-angle rotations. It is hence composed of three rotation matrices and the resulting matrix is of the form $R(\varphi_1,\Phi,\varphi_2) = R_3(\varphi_2)\cdot R_2(\Phi)\cdot R_1(\varphi_1)$, where the rotation matrices $R_1(\varphi_1)$, $R_2(\Phi)$ and $R_3(\varphi_2)$ are defined as follows:

$$R_1(\varphi_1) = \begin{vmatrix} \cos\varphi_1 & \sin\varphi_1 & 0 \\ -\sin\varphi_1 & \cos\varphi_1 & 0 \\ 0 & 0 & 1 \end{vmatrix}$$

$$R_2(\Phi) = \begin{vmatrix} 1 & 0 & 0 \\ 0 & \cos\Phi & \sin\Phi \\ 0 & -\sin\Phi & \cos\Phi \end{vmatrix} \tag{2.8}$$

$$R_3(\varphi_2) = \begin{vmatrix} \cos\varphi_2 & \sin\varphi_2 & 0 \\ -\sin\varphi_2 & \cos\varphi_2 & 0 \\ 0 & 0 & 1 \end{vmatrix}$$

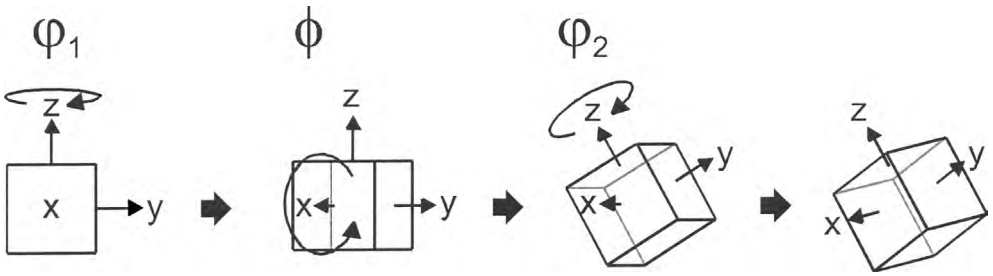

Figure 2.16. Illustration of the Euler-angles using the Bunge-convention. [10,12]

The coefficients of the general rotation matrix $R(\varphi_1,\Phi,\varphi_2)$ therefore take on the form:

$$
\begin{aligned}
r_{11} &= \cos\varphi_1\cdot\cos\varphi_2 - \sin\varphi_1\cdot\sin\varphi_2\cdot\cos\Phi \\
r_{12} &= \sin\varphi_1\cdot\cos\varphi_2 + \cos\varphi_1\cdot\sin\varphi_2\cdot\cos\Phi \\
r_{13} &= \sin\varphi_2\cdot\sin\Phi \\
r_{21} &= -\cos\varphi_1\cdot\sin\varphi_2 - \sin\varphi_1\cdot\sin\varphi_2\cdot\cos\Phi \\
r_{22} &= -\sin\varphi_1\cdot\sin\varphi_2 + \cos\varphi_1\cdot\cos\varphi_2\cdot\cos\Phi \\
r_{23} &= \cos\varphi_2\cdot\sin\Phi \\
r_{31} &= \sin\varphi_1\cdot\sin\Phi \\
r_{32} &= -\cos\varphi_1\cdot\sin\Phi \\
r_{33} &= \cos\Phi
\end{aligned}
\qquad (2.9)
$$

In orientation image mapping, Euler-angles are commonly used to graphically illustrate the local orientation by assigning a specific colour to a specific orientation. The Euler-angles of each data point are converted into a colour in the RGB-colour space. These colours are composed of a red (R), a green (G) and a blue (B) component whose values are calculated as follows:

$$
[R] = \frac{255\cdot\varphi_1}{360°}
$$

$$
[G] = \frac{255\cdot\Phi}{360°} \qquad (2.10)
$$

$$
[B] = \frac{255\cdot\varphi_2}{360°}
$$

A detailed introduction to the principles and practice of all modern texture analysis is provided by Randle and Engler [67]. Extensive information on the principles and the equipment for electron backscattered diffraction can be found in the book by Schwartz et al [73].

CHAPTER 3

EXPERIMENTAL PROCEDURES

3.1 MATERIALS AND PROCESSING

Three non-commercial high-carbon steels were used for this investigation, namely a hypo-eutectoid steel containing 0.6 weight-percent of carbon, an (pseudo-) eutectoid steel with 0.8 wt.% C and a hyper-eutectoid steel with 1.2 wt.% C. The steels contain a pearlite volume fraction of 0.80, 0.99 and 0.92, respectively. The hypo-eutectoid steel also contains 20 volume-percent of ferrite, while the eutectoid and the hyper-eutectoid steels contain 1 and 8 vol.% cementite, respectively. The volume-percentages are calculated from data in the ASM Handbook [2]. The chemical compositions of the three steels are given in table 3.1.

The materials were supplied by Corus UK who produced them in batches of 60 kg at the Swinden Technology Centre in Rotherham. The steels were vacuum cast into slightly tapered ingots with a square cross-section of approximately 150 mm by 150 mm and an approximate length of 400 mm. Subsequently, the ingots were reheated and soaked at 1,200 °C (1,473 K) to homogeneously dissolve the carbon, followed by hot rolling at a temperature of 1,050 °C (1,323 K) to a thickness of 75 mm, which is equivalent to approximately 50 % rolling reduction. The slabs were then air-cooled to room temperature to produce steels with an initial grain size of about 40 µm.

Table 3.1. Chemical composition in weight-percent of the three high-carbon steels.

Steel	C	N	Al	Si	P	S	Mn
hypo-eutectoid	0.61	0.0057	0.031	0.20	0.016	0.005	0.69
eutectoid	0.81	0.0062	0.031	0.20	0.015	0.004	0.70
hyper-eutectoid	1.22	0.0069	0.030	0.20	0.016	0.005	0.69

3.2 MEASUREMENTS AND OBSERVATIONS

Samples were taken from the rolled slabs with their length axis parallel to the rolling direction and subsequently machined to cylindrical extrusion specimens with a diameter of 14.75 mm and a length of 100 mm. Prior to processing, all specimens were lubricated with a graphite coating to facilitate the extrusion, followed by heating them for 20 minutes in order for the steel to reach the

processing temperature of 500 °C (773 K) and to allow the temperature in the sample to become fully homogeneous. The specimens were extruded in the equal-channel angular press at a rate of 30 mm/min ($5 \cdot 10^{-4}$ m·s^{-1}) for up to five passes, during which a constant strain path deformation was maintained. This processing route is generally known as route A [17] and does not involve rotation of the billet in between extrusion cycles. The constant strain path deformation was chosen, because previous research showed it to be the most effective method to introduce a homogeneous submicrocrystalline structure under the present equal-channel angular pressing conditions [18,86]. The specimen was water-quenched immediately after each pressing, thus eliminating any chance of recovery at such elevated processing temperatures.

Figure 3.1 depicts the extrusion die that was used. It consisted of two mirrored halves that are closed during pressing. Each die halve consists of an inlet and an outlet channel that intersect at an angle of $\Phi = 120°$. Both are semi-cylindrical channels with a constant diameter of 15 mm. Furthermore, the outer corner at the plane of intersection of the two channels is not rounded off, i.e. $\Psi = 0°$. These parameters yield an effective strain of $\varepsilon_{eff} \sim 0.67$ per pass, which leads to the set of deformations given in table 3.2.

Subsequent to the ECAP-processing, the extruded specimens were prepared either for observation in a scanning electron microscope (SEM) or for assessment of the mechanical properties by tensile testing and microhardness measurements. Figure 3.2 schematically depicts the sample preparation: firstly, the undeformed rear end of the sample is cut off (this is the piece with length L_2). The following step involves cutting off an approximately 5 mm thick disk at points AD and

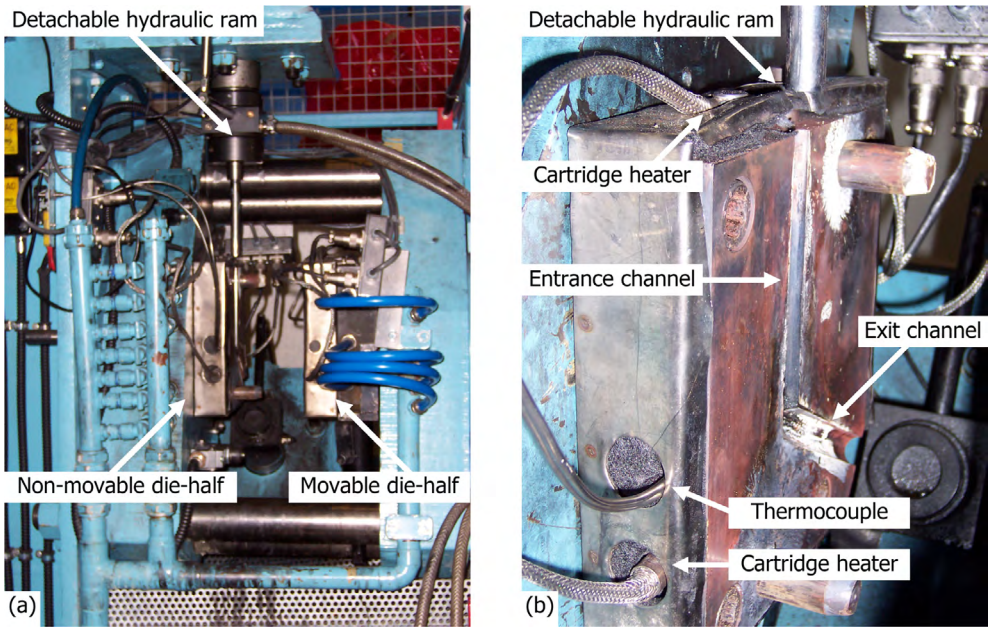

Figure 3.1. Construction of the die for equal-channel angular pressing.

Table 3.2. Effective deformation (ε_{eff}) of the billet during the first five passes (N) of equal-channel angular pressing using a channel angle of $\Phi = 120°$ and a corner angle of $\Psi = 0°$.

N	0	1	2	3	4	5
ε_{eff}	0.00	0.67	1.33	2.00	2.67	3.33

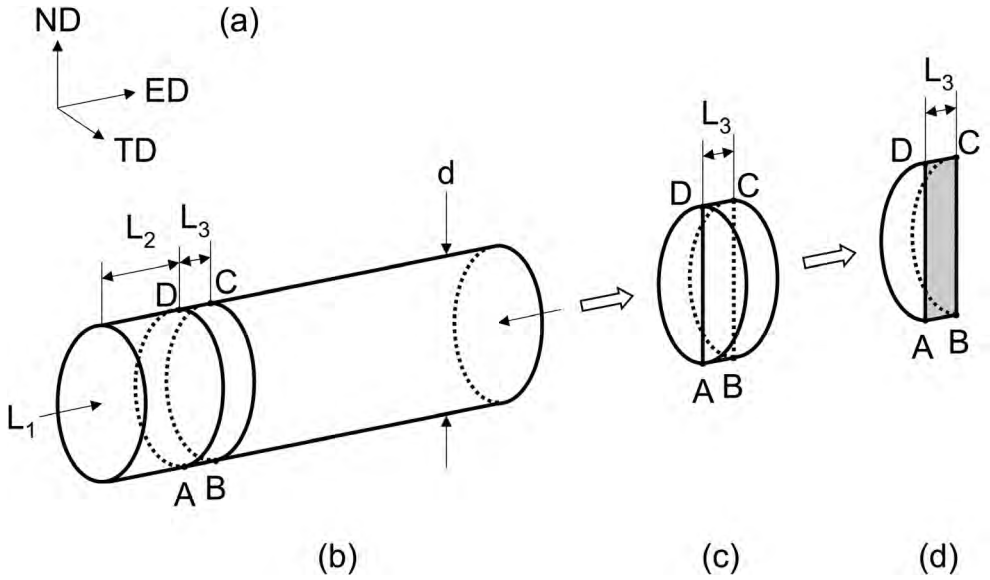

Figure 3.2. Sample preparation for microscopic observation and assessment of the mechanical properties. ED = extrusion direction, ND = normal direction and TD = transverse direction.

BC (see figure 3.2a). This disk is again sawn in half across plane ABCD (see figure 3.2b), yielding two semi-circular pieces. These pieces were subsequently mounted and mechanically polished down to a surface roughness of 0.05 µm, where each polishing step lasted one hour.

After the mechanical polishing treatment, the specimens that were used for the observation of the microstructure by SEM were chemically etched for 16 seconds in a well-stirred solution of 5 g 100 wt.% pure picric acid ($C_6H_6N_3O_7$) and 5 ml 8 vol.% pure hydrochloric acid (HCl) in 100 ml 100 vol.% pure methanol (CH_3OH). This particular etchant was chosen, because it attacks the ferrite, while leaving the cementite unharmed. It therefore enables a clear distinction between these two phases, but unlike nital it does not reveal the grain boundaries. The samples that were used for the electron backscattered diffraction analysis were given a different treatment to yield a strain-free surface: an electropolishing treatment was carried out by submerging the mechanically polished sample for 10 seconds in a well-stirred solution under an applied constant voltage of 60 V, followed by thorough cleaning in a bath of methanol. The solution consisted of 8 ml 62 vol.% pure perchloric acid ($HClO_4$) in 92 ml 100 vol.% pure acetic acid (CH_3COOH).

The microstructures of the processed specimens were characterised by secondary electron imaging or high-resolution electron backscattered diffraction analysis. Images and maps were made at the centreline of the specimen to avoid any effects of possible inhomogeneous flow on the microstructure. The plane of view is indicated in grey in figure 3.2d and is spanned by the normal and extrusion direction. The viewing direction lies parallel to the transverse direction. Orientation image maps were acquired from samples at different strain levels, using either a Philips XL30 or a CamScan Maxim 2040SF scanning electron microscope. Each microscope is equipped with a field-emission gun (FEGSEM) and a Nordlys-detector from HKL Technology for the automated detection of the Kikuchi-patterns. In addition, Channel5-software from HKL Technology was used for the acquisition of the patterns. Both FEGSEM's have a spatial resolution

of approximately 30 nm and an angular resolution of approximately 1 °. Further details of the characteristics of this system can be found in the review by Humphreys [31].
Figure 3.3 depicts the orientation convention of the orientation image maps that is adapted here. Unless otherwise stated, the orientation of the specimen is always such that the extrusion direction (ED) is towards the right side of the vacuum chamber, which corresponds to a positive vertical (or upwards) direction on the orientation image map. Furthermore, the positive horizontal (or rightwards) direction on the map corresponds to the normal direction (ND) of the specimen. As the orientation image map lies parallel to the transverse plane, the direction of view lies parallel to the transverse direction (TD) and the direction perpendicular to the map and exiting the plane of view corresponds to the transverse direction. Hence, the plane of view of the specimen is the transverse plane. The shear direction (SD) and the normal to the shear plane (SPN) are also depicted in figure 3.3. Note that the shear direction is always positioned at a fixed angle of 60 ° to the extrusion direction due to the die configuration.

The assessment of the mechanical properties at different levels of deformation was carried out by both Vickers microhardness measurements (with a load of 1 kg) and tensile testing. The remaining ECAP-processed samples were used to produce two tensile test specimens that were subsequently tested at room temperature in order to determine the 0.2 % proof stress, the 0.5 % proof stress, the ultimate tensile stress and elongation at fracture. The tensile testing was again carried out at the Swinden Technology Centre of Corus UK.

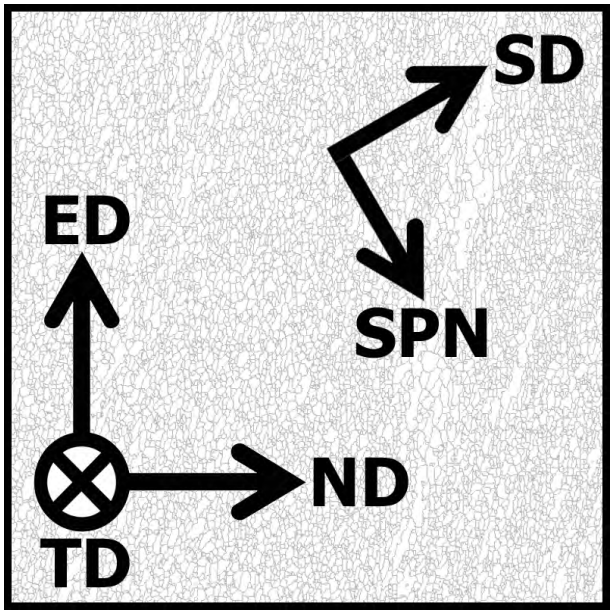

Figure 3.3. Orientation convention of the orthogonal axes system with respect to the orientation image map.

CHAPTER 4

RESULTS AND DISCUSSION

4.1 SECONDARY ELECTRON IMAGE ANALYSIS

Microstructural analysis was carried out by means of secondary electron imaging in a scanning electron microscope. Images were taken of the three high-carbon steels in the as-received condition and in the deformed conditions after one to five passes by equal-channel angular pressing. Subsequent qualitative and quantitative analysis yielded data on the evolution of the microstructures. This was done with the aims of observing and analysing the changes in the microstructure with increasing strain and to later on link these changes to the mechanical properties.

This section starts off with a description of the procedures for the analysis of the secondary electron images, followed by a qualitative description of the microstructures in subsection 4.1.2. Subsequently, a quantitative analysis of the microstructures will be given in subsection 4.1.3 and in the fourth and final subsection the findings from the microstructural analysis are discussed.

4.1.1 PROCESSING AND ANALYSIS PROCEDURES

DATA ACQUISITION

Specimens for the analysis in the scanning electron microscope were prepared using the routines mentioned previously in section 3.2. Subsequently, the specimens were placed in the scanning electron microscope for the actual microscopic analysis using secondary electron imaging. The microscope settings were adjusted to a working distance of 10 mm, an acceleration voltage of 10 keV, beam size 3 and aperture size 4. These settings were used for all the images and corrections for astigmatism were applied.

Images of the microstructures were taken from the three high-carbon steels in each condition. Three categories of images were made, namely:

(1) Survey images

These images give a general impression of the microstructure in a certain condition. Hence, they cover a large area and are made at a low magnification of 500x to 1,000x. These images are not suitable for quantitative analysis, because of the low magnification;

(2) Images of specific features

Contrary to the survey images, these images were made of small characteristic features in the microstructure. These detailed images were taken at high magnifications of 2,000x to 20,000x, although no quantitative analysis was carried out on these images;

(3) Images of (un-) fragmented lamellae

These images were taken with the purpose of determining the interlameller distance, the lamellae width and the rate of fragmentation of the cementite lamellae. The images for the quantification of the distance and the width were made of the three high-carbon steels in the initial condition only, because the microstructures of the steels in the deformed conditions are so complex that no accurate value of the distance and the width can be determined. The images for the quantification of the rate of spheroidisation were made of all conditions. For accurate quantifications, it was necessary to use high magnifications in the range of 2,000x to 40,000x.

DATA PROCESSING

The computer programme QWIN was used for the quantitative analysis of the images. This commercially available software is capable of quantitatively analysing images and can be modified to a wide range of purposes.

The secondary electron images need to be transformed from grey-scale images to pure black-and-white (binary) images before being analysed. An automatically or a manually selected threshold was applied to convert all grey-values below the threshold to black and all grey-values above the threshold to white.

The selection of the correct value of the threshold poses another problem, since the quality of the images is not optimal for quantitative analysis, due to a relatively large beam size, a low resolution and a high magnification. These three factors lead to a relatively large width of the edge of an object as compared to the actual dimension of an object. Hence, the computer software is not always capable of selecting the correct threshold value. In order to overcome this problem, it is chosen to create three binary images from one grey-scale image, namely one for which the threshold is automatically set and two for which the threshold is manually chosen using the lowest and highest acceptable grey-scale value. All parameters are then calculated for each of these and the average value is taken and used for further analysis.

In the quantitative analysis the objects that touch the edges of the image were not omitted from the analysis. If these objects were omitted, the number of detected lamellae would be reduced to zero in the case of the images of the unfragmented lamellae, while the number of detected lamellae would be hardly affected due to their abundance in case of the images of fragmented lamellae.

The width appeared to be the best suitable parameter for the quantitative analysis of the lamellar microstructures in the initial conditions. Additionally, the perimeter, the area, the roundness and the equivalent circular diameter appeared to be the best suitable parameters for the quantitative analysis of the deformed specimens. They were chosen because of their usefulness, ease of determination and accuracy. A description of these parameters is given below:

(1) Width

The width or thickness of an object is defined as the distance between the parallel tangents of two opposite points of an object. The dimension of the width is expressed in unit length. The width can be determined in all types of microstructures, although preferably in microstructures with straight lamellae. Difficulties arise due to the rotation of the lamellae and the matrix that may cause the measured distance and width to differ from the actual distance.

(2) Perimeter

The perimeter or circumference of an object is defined as the total length of the outer edge of the object, where holes inside the object are disregarded. The dimension of the perimeter is expressed in unit length. The perimeter can be easily and in most cases also accurately determined in all types of microstructures. Moreover, it gives a good indication of the changes in the microstructure.

(3) Area

The area of an object is defined as the total number of pixels and its dimension is expressed in the square of a unit length. Like the perimeter, the area can be easily and accurately determined under most conditions and it also gives a good indication of the changes in the microstructure.

(4) Roundness

The roundness is a dimensionless parameter that is defined as the ratio of the square of the perimeter over the product of the area and 4·π. The following equation was used to calculate the average roundness:

$$R = \frac{L_{p,i}^2}{4 \cdot \pi \cdot A_i \cdot f} \tag{4.1}$$

In this equation $L_{p,i}$ is the perimeter of object i, A_i is the area of object i and f is a correction factor that is used only by QWIN to correct the perimeter for the effect of the corners produced by the digitisation process. The roundness of fully round objects is one, while the roundness for non-circular objects is more than one. This parameter can be easily and in most cases also accurately determined in all types of microstructures, preferably deformed microstructures with a certain degree of spheroidisation. It is, however, not a useful parameter for the quantitative analysis of lamellar microstructures.

(5) Equivalent circular diameter

The equivalent circular diameter or Feret-diameter is defined as the diameter of a circle having the same area as the object. Its dimension is expressed in unit length. The following equation was used to calculate the average equivalent circular diameter:

$$ECD_{avg} = \frac{1}{N} \cdot \sum_{i=1}^{i=n} \sqrt{\left(\frac{4 \cdot A_i}{\pi}\right)} \tag{4.2}$$

In this equation, N is the total number of analysed objects. The equivalent circular diameter can be determined in all types of microstructures, and most accurately in deformed

microstructures. This parameter may give a good indication of the rate of fragmentation of the lamellae. The ECD can be easily and in most cases also accurately determined.

Preliminary analysis of the secondary electron images has shown that it is impossible to accurately determine the width of an object in a deformed microstructure. This is due to the complex nature of the deformated microstructures and to the fact that the cementite fragments become progressively more fragmented and their edges become progressively more rounded off. It was therefore decided to determine only the width of the lamellae in the initial conditions. For the same reasons and because most of the lamellae extend beyond the limits of the image, a reliable value of the length cannot be given either. Hence, it was decided not to quantify the length at all in this investigation. Microscopic differences in the thickness can be filtered out by taking the average of at least six measurements.

For all the parameters listed above goes that care should be taken with the quantification of images of highly spheroidised microstructures at relatively low magnification and with images of poor contrast, since the inaccuracy under these circumstances is significant.

4.1.2 QUALITATIVE ANALYSIS

This subsection deals with the evolution of the microstructures of the three steels as observed after each consecutive pressing. This subsection is divided into three parts; in the first part a description is given of the microstructures that were observed in the initial conditions, while in the second part yet another description is given of the development of the microstructures as a function of deformation, and in the subsequent paragraphs the microstructures that are typical for one of the phases are described. The micrographs shown in these subsections are all produced by SEM and oriented according to the orientation convention laid out in section 3.2.

MICROSTRUCTURES OF THE UNDEFORMED CONDITIONS

The microstructures of the three steels in the initial condition are depicted in figures 4.1 to 4.3. The microstructures shown in these figures, are typical for lamellar eutectoid materials. Three phases can be observed, namely cementite, ferrite and pearlite. In all three steels, the pearlite has its usual appearance of thin and long parallel lamellae of cementite in a ferrite matrix. In the high-contrast and low-brightness images that were taken, the cementite lamellae in the pearlite appear as the bright phase, whereas the ferrite lamellae and the grain boundary ferrite appear as a dark phase. The grain boundary cementite shows up as a dark phase with light edges.

The microstructure of the hypo-eutectoid steel in the as-received condition is depicted in figure 4.1. This secondary electron image shows pearlite and ferrite grains in a ratio of 80 vol.% to 20 vol.%. Figure 4.2 shows a secondary electron image of the microstructure of the eutectoid steel. This steel is almost fully pearlitic, since it is actually slightly hyper-eutectoid with 1 vol.%

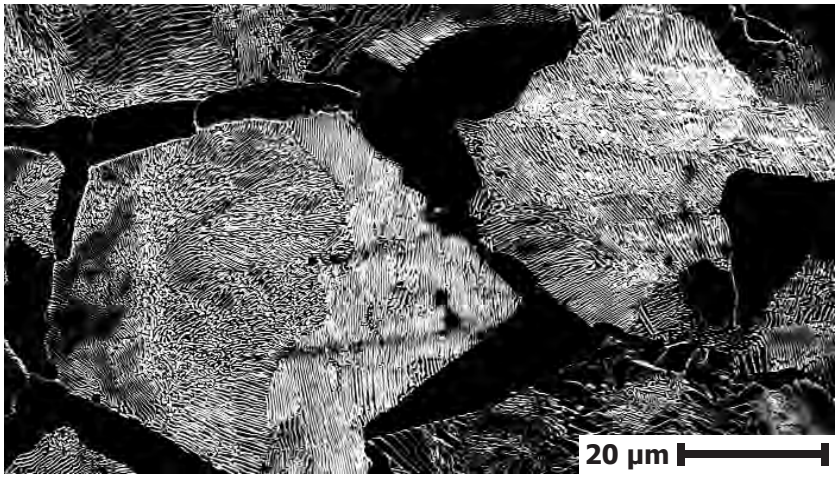

Figure 4.1. Secondary electron image of the hypo-eutectoid steel in the initial condition.

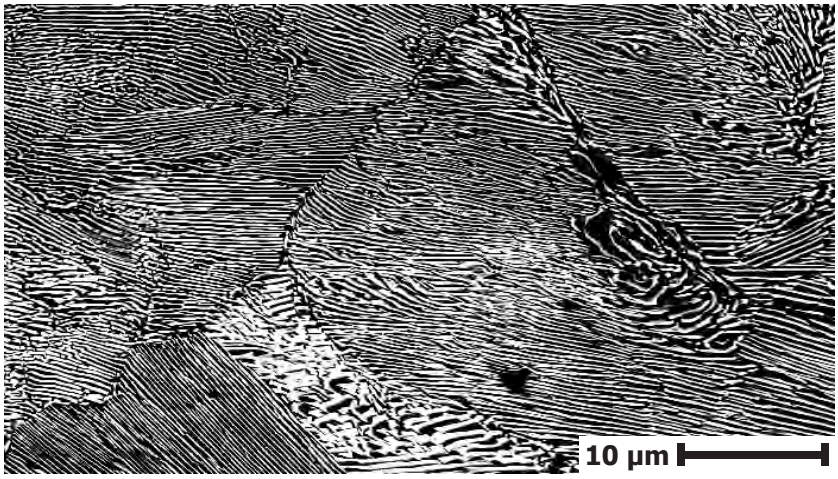

Figure 4.2. Secondary electron image of the eutectoid steel in the initial condition.

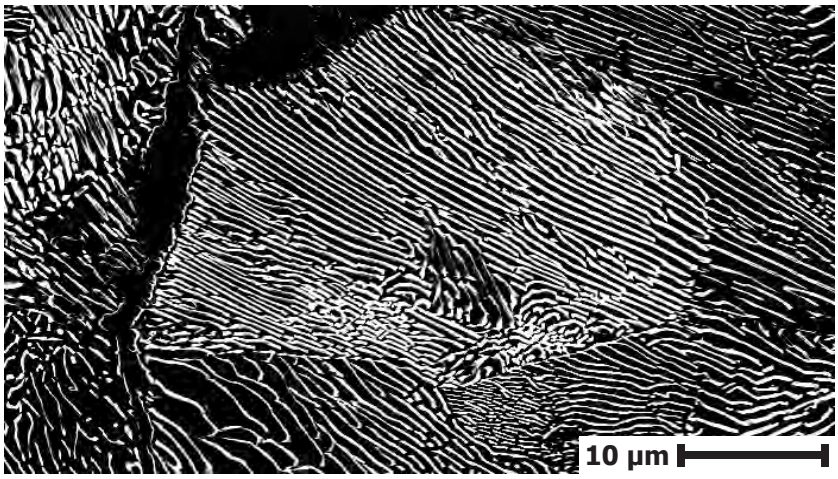

Figure 4.3. Secondary electron image of the hyper-eutectoid steel in the initial condition.

grain boundary cementite. Finally, the microstructure of the hyper-eutectoid steel, shown in figure 4.3, exhibits a matrix of pearlite grains (the lamellar phase) with some cementite (the thick dark phase) at the pearlite grain boundaries, in a ratio of 92 vol.% pearlite to 8 vol.% cementite. The data for these calculations were taken from the ASM Handbook [2].

GENERAL BEHAVIOUR OF THE DEFORMED CONDITIONS

The microstructure of the three high-carbon steels evolves from a typical lamellar eutectoid structure into a fully fragmented structure, because of the applied intense shear deformation. The origin of the fragmentation process lies in the accommodation of the macroscopic shear strain by the microstructure. A certain amount of inhomogeneity of the structure on a microscopic level is present due to different phases, grain dimensions, crystal orientations and subgrain structures. This implies that in each grain the deformation conditions are different and hence each grain responds differently. Gradients in the deformation condition occur even within a grain. This inhomogeneous behaviour of the microstructure often leads to the formation of very complex microstructures, as can be seen in figure 4.4.

It is possible to distinguish the following four stages in the evolution of the microstructure of the three high-carbon steels during equal-channel angular pressing: (1) shear banding, (2) spheroidisation, (3) separation and (4) shrinkage. The first stage comprises the plastic deformation of the lamellae and the formation of deformation bands. This is exhibited in figure 4.5, which shows two deformation bands (indicated by the arrows) that formed during two subsequent pressings. These bands are formed to accommodate the different deformation conditions in areas of a grain. Further deformation will lead to the second stage, which includes the breaking up of the lamellae inside the existing bands. The deformation bands are thin and long and frequently have an irregular shape. If fragmented the bands have the appearance of "canals" [89-91] that run through the microstructure, thereby dividing the pearlite colonies within the grains. An example of the second stage in the microstructural behaviour can be observed in figure 4.6. It should be noted, however, that the first and the second stage overlap to a certain extent; simultaneously, one can observe the formation of new bands and the connection of bands from neighbouring grains, together with the fragmentation of the existing bands. The fragmentation process is accelerated due to the fact that each pressing produces a different orientation of the deformation bands, since the plane of shear deformation is different in each of the pressings via route A.

The third stage is characterised by a substantial fraction of lamellae that have broken up into tiny fragments, while the remaining lamellae are fractured into smaller lamellae. Figure 4.7 shows a clear example of this stage of deformation. The number of "canals" has greatly increased, such that small regions of a more lamellar nature remain that have become isolated from other regions. The overall microstructure then has the appearance of "islands" [89-91] of deformed lamellae. In the fourth and final stage the fragmentation of the remaining lamellae has become the dominant process. The proceeding fragmentation causes the "islands" to become progressively smaller until the entire microstructure is fully and homogeneously fragmented at the end of this stage. Figure 4.8 shows an example of the eutectoid steel after four passes.

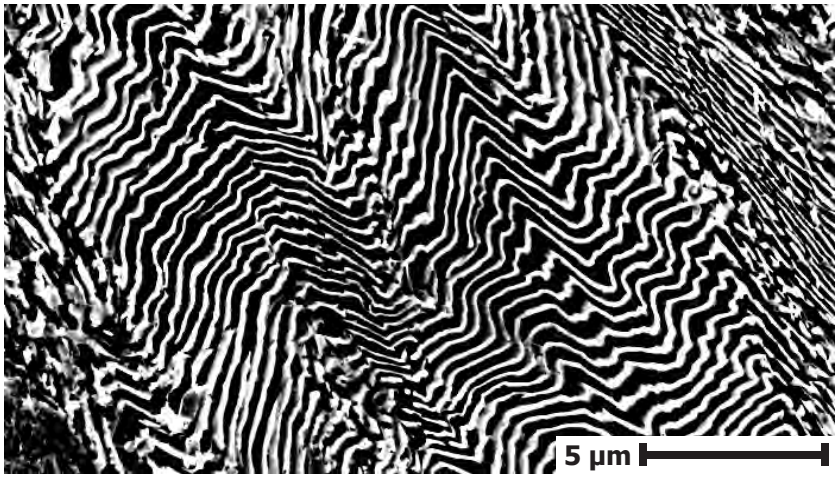

Figure 4.4. Secondary electron image showing complex and inhomogeneous deformation behaviour in the hypo-eutectoid steel after two passes.

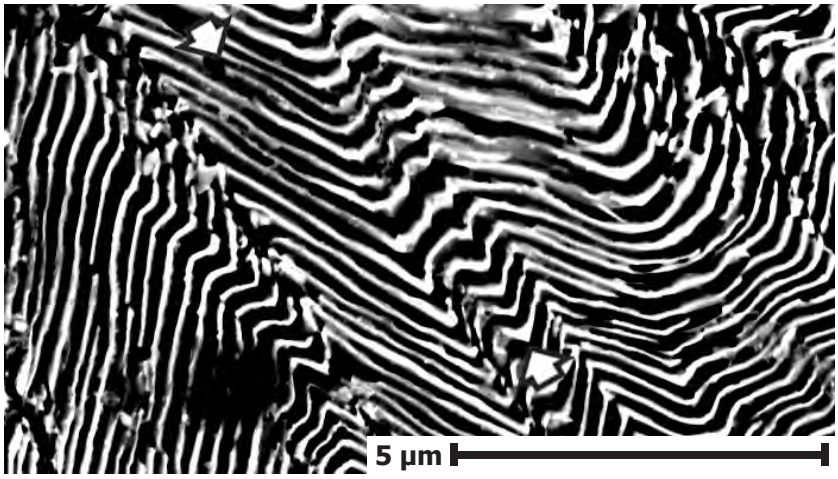

Figure 4.5. Secondary electron image of deformation bands in the eutectoid steel after two passes.

Figure 4.6. Secondary electron image of a "canal" cutting through a pearlite colony in the eutectoid steel after one pass.

The majority of the lamellae has broken up into tiny fragments, but a small number of smaller lamellae remains, meaning the fragmentation process is not complete yet.

Besides these common characteristics there are also several differences in the microstructural evolution, depending on the alloy. For instance, the rate of fragmentation differs from one type of steel to the other. Apparently, the fragmentation progresses at a higher rate in the hypo-eutectoid steel than in the other two steels. Already after three passes a considerable fraction of the lamellae is highly fragmented, while after five passes the fragmentation is complete. On the other hand, the eutectoid and especially the hyper-eutectoid steel still contain some smaller lamellae after five passes.

Additionally, after four passes it is possible to observe subgrains that are formed due to the severe deformation, such as the ones shown in figure 4.9. This secondary electron image of the hypo-eutectoid steel after five passes contains subgrains that formed in between the spheroidised cementite lamellae. It also clearly shows that the size of the subgrains is limited on two sides by the lamellae. Given the fact that several subgrain boundaries are clearly connected to the tips of fractured lamellae, it is very likely that the lamellae tips act as sources for the generation of new dislocations that during subsequent deformation evolve into subgrain boundaries. At the points indicated by the arrows, the lamellae were fractured, prior to the onset of spheroidisation, and the fracture tips have shifted a little, making the space between the fractured lamellae larger than the space between the spheroidised lamellae. These fracture tips seem to have a higher potential for the formation of dislocations than for instance other spheroidised lamellae fragments.

MICROSTRUCTURES OF THE DEFORMED FERRITE

Figure 4.10 shows a typical microstructure of the ferrite in the deformed hypo-eutectoid steel. The only deformation feature of the ferrite is that the softer ferrite grains are flattened and stretched out in between the harder pearlite grains due to the applied deformation. The ferrite grains have the appearance of "ribbons", whose morphology changes gradually from randomly shaped ferrite grains in the undeformed condition to high aspect-ratio grains with their longitudinal axis nearly parallel to the shear direction.

MICROSTRUCTURES OF THE DEFORMED PEARLITE

Pearlite is the main constituent of all three high-carbon steels. It exhibits several microstructural features during the initial passes of equal-channel angular pressing that are typical for this phase, regardless of the steel in which these are observed. Seven different features of deformed pearlite are shown in figures 4.11 through 4.18 and their characteristics are described below:

(1) Kink banding

Following its appearance of a kink in the pearlite lamellae, this type of microstructural feature has been appropriately designated "kink band" [32,66]. As can be seen in figure 4.11, the orientation of the lamellae is abruptly altered twice, namely once from the original orientation to the orientation of the kink band and once from that orientation back to the original one again. This microstructural feature obviously involves shear deforma-

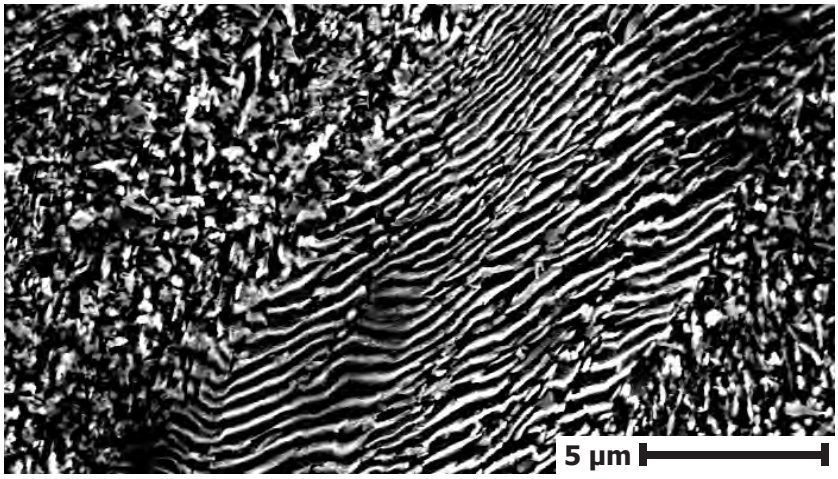

Figure 4.7. Secondary electron image of an "island" of lamellar pearlite among fragmented pearlite in the eutectoid steel after three passes.

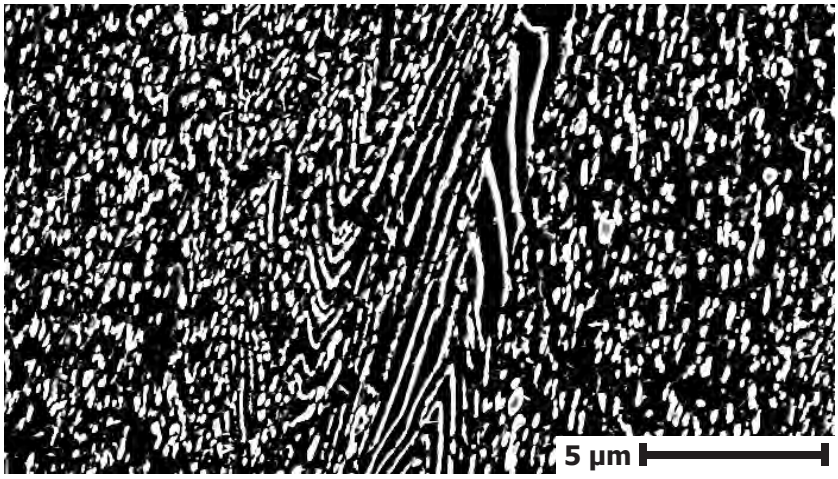

Figure 4.8. The same as figure 4.7, but taken after four passes.

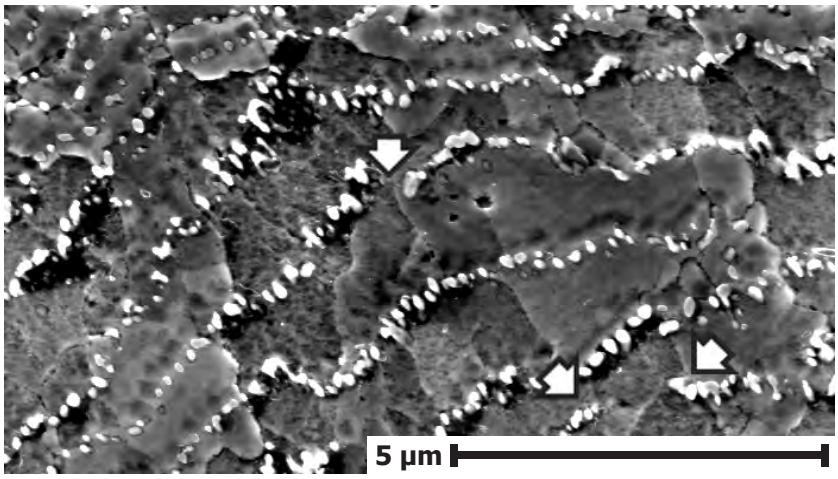

Figure 4.9. Secondary electron image of subgrains in the hypo-eutectoid steel after five passes.

tion, which causes the lamellae to be bent collectively in such a manner that they remain parallel to each other. The dimensions of the kink band are clearly visible and two (nearly) parallel shear planes may be distinguished at the points of inflexion. The width of the kink bands may vary considerably, ranging roughly from 80 nm to 10 μm. It is noticeable that the cementite lamellae in general do not crack due to the applied shear deformation, meaning the level deformation is only moderate or the cementite can sustain very high levels of deformation under these conditions. The ferrite surrounding the cementite lamellae may thereby act as a hydrostatic medium to prevent fracture of cementite [61]. Another noticeable characteristic is that the kink bands do not extend beyond grain boundaries, but are confined to a single grain. This is likely to be caused by a combination of a large lattice misorientation and local differences in strain accommodation between adjacent grains. This combination of factors causes local differences in the intensity of the deformation and perhaps in the mode of deformation as well, and prevent the kink band to continue in the neighbouring grain;

(2) Shear cutting

As can be observed in figure 4.12, the cementite lamellae are collectively broken, thus revealing a (nearly) linear row of fractured cementite lamellae. Unlike kink banding, the orientation of the lamellae is not changed because of the shear cutting, but the lamellae retain their original orientation. They are only slightly displaced with respect to each other in a direction that is nearly perpendicular to the lamellae. Since the lamellae are broken collectively, the required shear stress for shear cutting is higher than that required for kink banding. Hence, shear cutting can be considered as a more drastic deformation reaction of lamellae to accommodate the severe shear deformation during equal-channel angular pressing [89];

(3) Shear switching

Several examples of this deformation feature can be seen in figure 4.13, indicated by the arrows. This feature has the appearance of two diverging bands that originate in a single point. The bands are always formed by collective shearing of the lamellae over a small distance and in the opposite direction. They therefore show some similarity with kink bands, although on the other hand they are distinctly different, because the bands are always curved and because of the absence of a clearly distinguishable plane of inflexion. The exact mechanism of the formation of this type of microstructural feature is unclear. One possibility is that it involves a sort of tandem kink banding, where the two bands have opposite orientation in the transverse direction. Given the similarities with kink banding, shear switching requires only moderate shear deformation;

(4) Shearing

Figure 4.14 shows an example of shearing. This deformation feature is quite similar to the kink banding discussed before, since the lamellae are bent collectively and again the lamellae remain parallel to each other. Contrary to kink banding however, only a single shear plane can be observed. Another noticeable difference is that the angle under which the lamellae are bent, is much larger: acute angles of more than 90 ° are no exception!

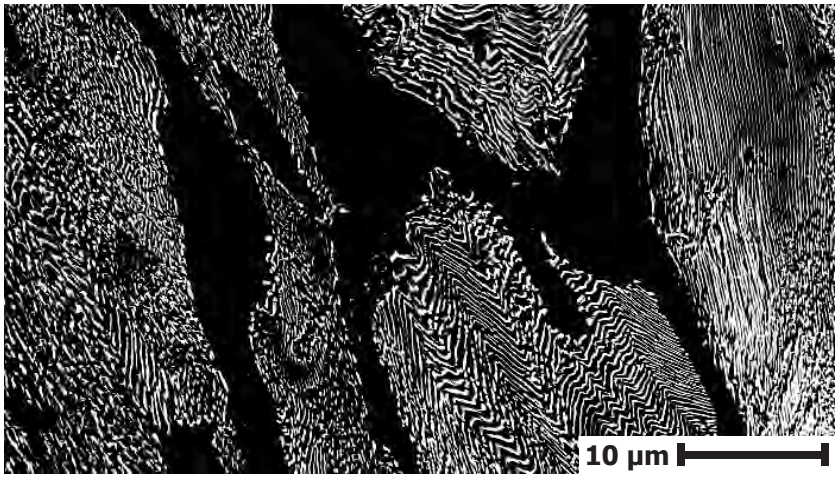

Figure 4.10. Secondary electron image of deformed ferrite in the hypo-eutectoid steel after two passes.

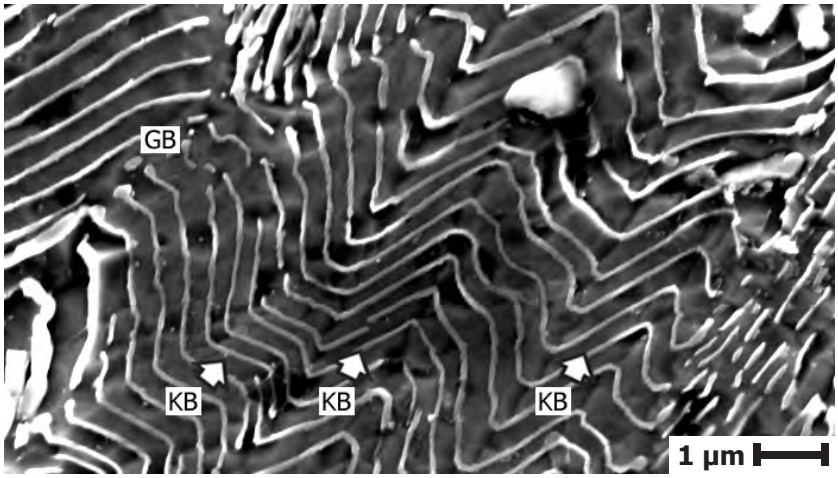

Figure 4.11. Secondary electron image of the eutectoid steel after one pass, showing kink banding in the deformed pearlite.

Figure 4.12. Secondary electron image of the hypo-eutectoid steel after two passes, showing shear cutting in the deformed pearlite.

Moreover, most of the lamellae are not broken. This contradicts the general believe that cementite is a brittle phase that is unable to deform plastically. Cementite is apparently very well capable of undergoing plastic deformation, but only under the appropriate circumstances. Additionally, given the often acute angles under which lamellae are deformed, shearing involves large local deformations;

(5) Buckling
Figure 4.15 (also figure 4.14) shows an example of buckling in the centre of the image. Buckling occurs under certain specific deformation conditions in which lamellae are compressed with such a force that they buckle. Buckling is a commonly observed deformation feature, despite its specific conditions. Adjacent buckled lamellae mostly have various complex wavy shapes, which is evidence of the microscopic heterogeneity in the local deformation condition. Details of these conditions are laid out in section 4.1.4;

(6) Necking
Figure 4.16 shows an example of cementite lamellae that remained almost perfectly aligned after the extrusion. It is also apparent that the lamellae have broken into smaller fragments and that the tip of the lamellae fragments show necking, similar to the necking that is observed during tensile testing. They retain their original undistorted shape but are being broken into smaller fragments. Details of the circumstances under which this deformation feature occurs, are given in section 4.1.4;

(7) Bending
An example of bending can be observed in figure 4.17 along with two narrow kink bands. The cementite lamellae are bent collectively, but, unlike kink banding, no plane of inflexion may be distinguished and the lamellae are bent gradually. Moreover, due to the large scale under which this instance of bending occurred, the deformation needs to be very homogeneous over a relatively large area and, consequently, instances like these are exceptional and bending is therefore mostly confined to microscale areas and moderate deformation.

The microscopic features may combine to form new and more complex deformation features during subsequent passes in severe deformation processing. Furthermore, it must be noted that microstructural features are not confined to a single material nor to a single deformation condition, i.e. more than a single deformation feature can be found co-existing in the same grain as adjacent features or superimposed on each other during subsequent deformation passes.

Another observation on the deformation behaviour of pearlite can be made at higher magnifications, such as figure 4.18. It can be seen in this secondary electron image that the pearlite grains exhibit some sort of transition region (TR) between the neighbouring ferrite grains (α-Fe) and the interior of the pearlite grains (CR). The pearlite lamellae in this region often seem to be more aligned to the direction of flow of the ferrite than the pearlite in the centre of the grains. It appears from microscopic observation that the extent of fragmentation of the pearlite in the transition region depends on the orientation of the pearlite lamellae with respect to the ferrite. If the pearlite lamellae are oriented at high angles, then they are easily broken into

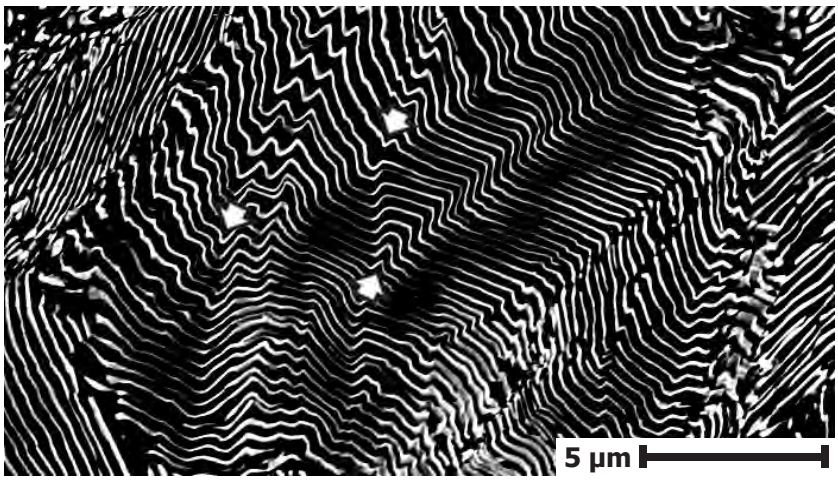

Figure 4.13. Secondary electron image of the eutectoid steel after one pass, showing shear switching in the deformed pearlite.

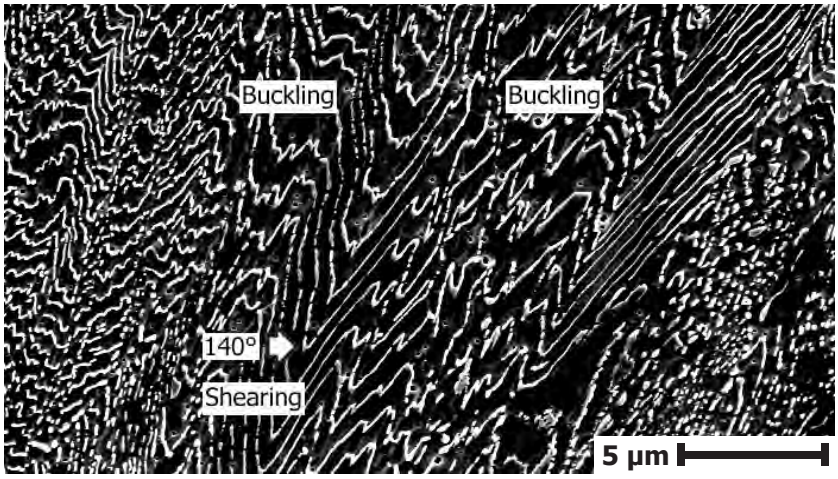

Figure 4.14. Secondary electron image of the hypo-eutectoid steel after four passes, showing shearing and buckling in the deformed pearlite.

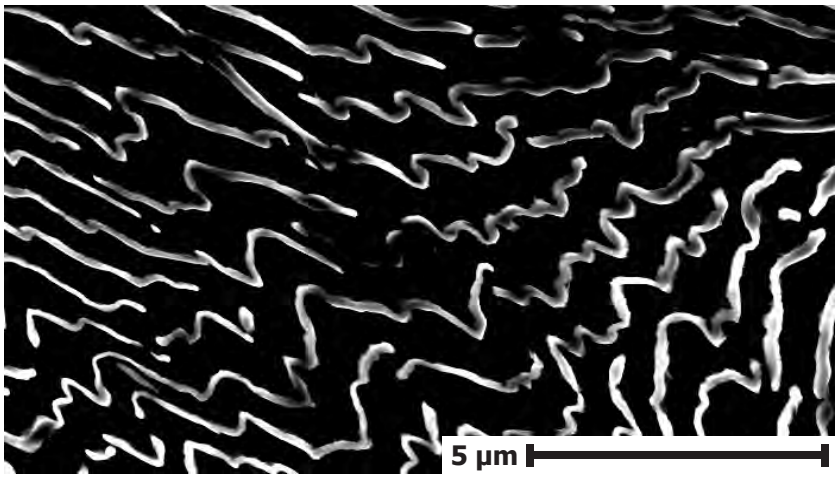

Figure 4.15. Secondary electron image of the hyper-eutectoid steel after one pass, showing buckling in the deformed pearlite.

small fragments. Instead, if they are oriented at relatively low angles, then they are likely to remain intact or otherwise deform plastically. This orientation gradient suggests the presence of local strain inhomogeneity that causes the ferrite to deform at a higher rate than the pearlite in the centre. This discrepancy in the rate of deformation has to be accommodated for by the pearlite in the transition region. It is however impossible to quantify these observations at this point. A more detailed elaboration of the quantification of the local strain inhomogeneity will therefore be given in the section on electron backscatter diffraction analysis.

It is evident from the observation of the microstructures that different grains respond differently to the imposed stress and that even within a single grain areas may respond differently. The observation that the microstructural features are confined to a single grain and that their dimension and orientation may vary considerably from one grain to another implies that the magnitude and orientation of the deformation may vary considerably from one grain to another, depending on which slip system is activated. Thus, while the macroscopic strain may seem homogeneous, i.e. near plain shear strain, the deformation behaviour at a microscopic level is very inhomogeneous. It may therefore be concluded that strain accommodation plays an important role during deformation. This has also been pointed out by Nijhof [61] who conducted wire-drawing experiments on pearlitic steels and by Wang et al [89-91] who conducted equal-channel angular pressing on an eutectic aluminium-copper alloy.

MICROSTRUCTURES OF THE DEFORMED CEMENTITE

Although cementite is one of the constituents of all three steels in the form of Fe_3C-plates in the pearlite, the grain boundary cementite in the hyper-eutectoid steel responds differently from the cementite lamellae in the pearlite. The former type of cementite is mostly much thicker, longer and more irregularly shaped than the latter type. Consequently, the different dimensions cause different mechanical behaviour. Unlike the cementite lamellae inside the grains, the cementite at the grain boundaries does not exhibit the complex microstructural features that the cementite lamellae in the pearlite do. In fact, the grain boundary cementite shows several microstructural features that are characteristic for this phase and hence are observed only in the hyper-eutectoid steel. Figures 4.19 to 4.21 show an overview of these characteristic microstructures. At relatively low magnification (of typically 2,000x or less) the microstructure reveals the formation of dark, large and irregularly shaped particles, as can be observed in figure 4.19. These particles appear after two passes by equal-channel angular pressing and persist during subsequent deformation, although they decrease in size and increase in number with increasing deformation. Secondary electron images at higher magnification, shown in figures 4.20 and 4.21, reveal the origin and nature of these particles. These images reveal that the particles are not solid, but in fact form clusters of deformed and partially fragmented cementite lamellae that seem to "collide" with the grain boundary cementite. Figure 4.20 shows an example of such a "collission" and figure 4.21 shows a closer view of such a cluster. A possible mechanism to explain the formation of these clusters is that under certain deformation conditions a pearlite colony adjacent to a grain boundary is pushed towards the grain boundary where it encounters the cementite. The pearlite colony then reacts similar to a car's crumple zone during a crash into a rigid object.

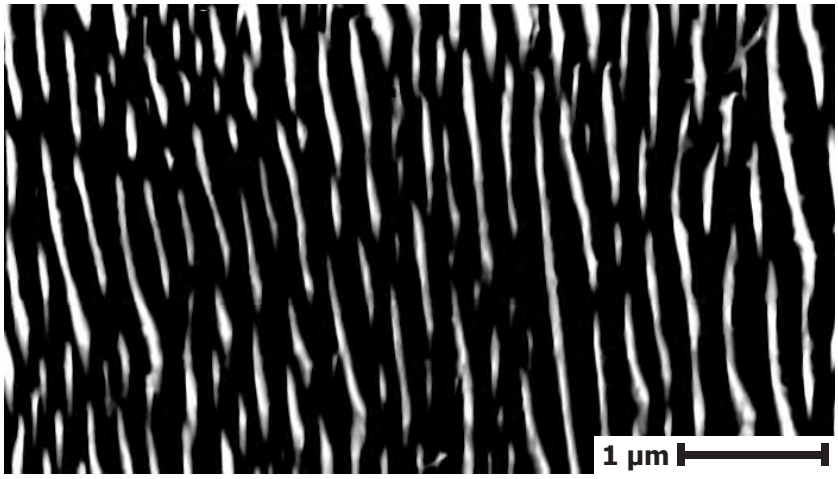

Figure 4.16. Secondary electron image of the eutectoid steel after two passes, showing necking in the deformed pearlite.

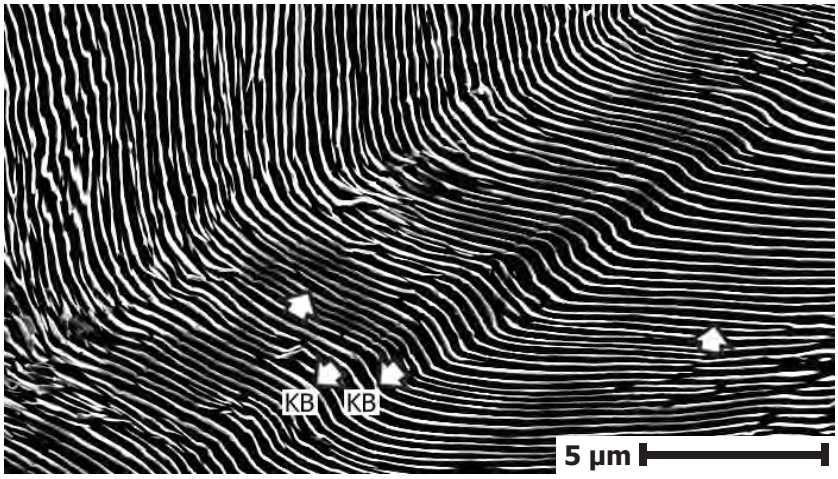

Figure 4.17. Secondary electron image of the eutectoid steel after one pass, showing bending in the deformed pearlite.

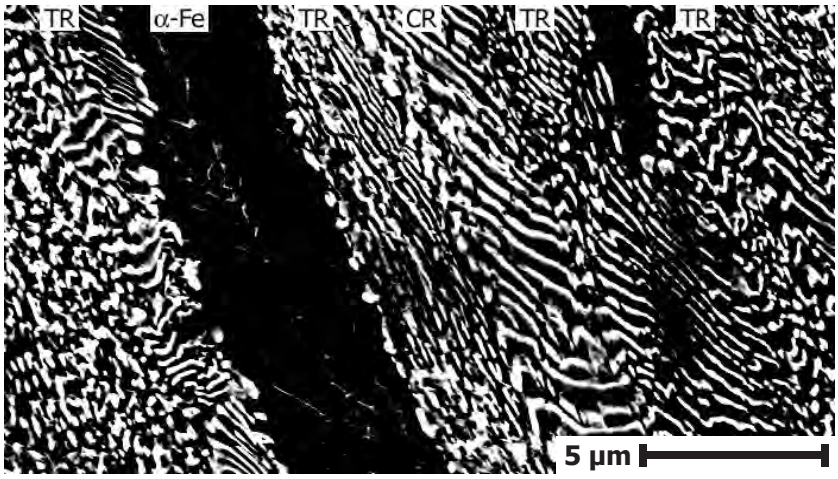

Figure 4.18. Secondary electron image of inhomogeneous deformation in the hypo-eutectoid steel after two passes.

If now the lamellae in the colony are oriented at high angles with respect to the grain boundary cementite, the lamellae will shatter into tiny fragments. On the other hand, if the misorientation angle is relatively small, the lamellae will deform plastically and pile up against the grain boundary cementite. Consequently, the ferrite lamellae in between the cementite lamellae is mostly squeezed out, hence giving the cluster the appearance of a large and solid second phase particle at relatively low magnifications. Moreover, the clusters of deformed cementite lamellae even act as rigid second phase particles during deformation. A further elaboration on this topic will be given in the section on the microstructural behaviour as observed and measured by electron backscattered diffraction analysis.

4.1.3 QUANTITATIVE ANALYSIS

The data from the secondary electron images was collected using QWIN and subsequently analysed using the procedures laid out in section 4.1.1. The results of this analysis are presented in the next paragraphs. Graphs of the area, the perimeter and the roundness as a function of the number of passes for the three high-carbon steels are shown in figures 4.22 to 4.24. A survey of the average and standard deviation values is given in tables A1 and A2 in appendix A.

LAMELLAE DIMENSIONS

The interlamellar spacing was determined using the image analysis programme ImageTool (version 3), which calculates the distance between and width of the cementite lamellae in a certain selected region. The interlamellar spacing is defined here as the perpendicular distance between the edges of two opposite lamellae, whereas the lamellar width is the cross-sectional width of the lamellae. The values that are thus obtained are listed in table 4.1.

Table 4.1. Average measured distance and width of the cementite lamellae in the three high-carbon steels in the initial condition.

	Distance (µm)	**Width (µm)**
Hypo-eutectoid steel	0.28	0.10
Eutectoid steel	0.27	0.11
Hyper-eutectoid steel	0.48	0.18

The table above shows that the lamellae are substantially wider spaced and thicker in the hyper-eutectoid steel than in the other two steels. The distance and width of the lamellae in the hypo-eutectoid and the eutectoid steel are very similar. These differences will probably cause the hyper-eutectoid steel to respond differently to deformation as compared to the other two steels.

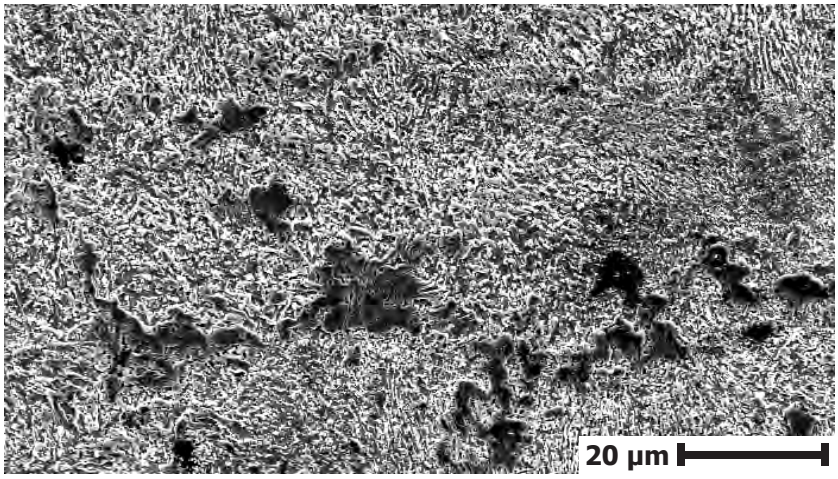

Figure 4.19. Secondary electron image of a deformed microstructure in the hyper-eutectoid steel after five passes.

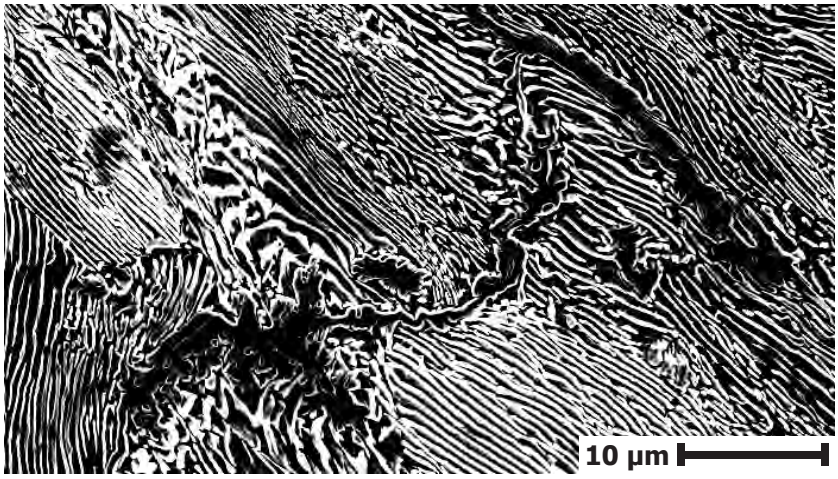

Figure 4.20. Secondary electron image of the hyper-eutectoid steel after one pass, showing complex deformation behaviour at the grain boundaries.

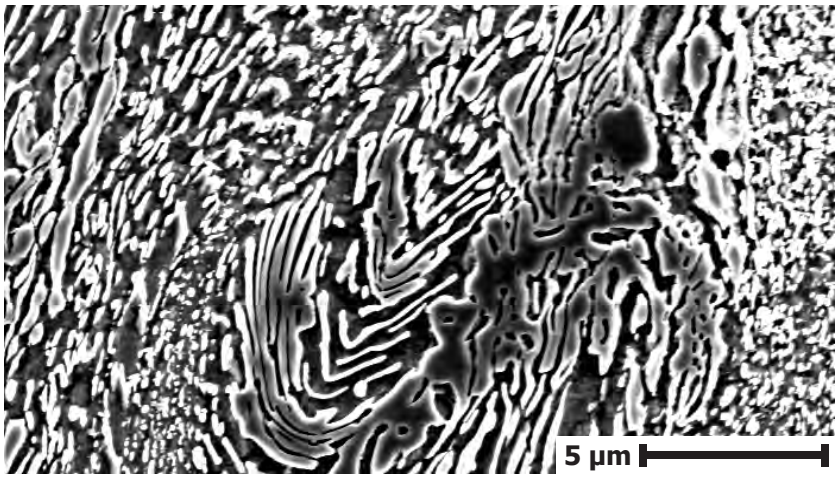

Figure 4.21. Secondary electron image of the hyper-eutectoid steel after four passes, showing a close-up view of a cluster of deformed cementite lamellae.

FRAGMENTATION BEHAVIOUR

The area and the perimeter, depicted in figures 4.22 and 4.23, reveal very similar trends. Firstly, the curves of the hypo-eutectoid steel are fluctuating without exhibiting a particular trend in all the graphs. On the other hand, the curves of the other two steels are relatively widely spaced, except for the condition after one pass and the highest levels of deformation. The curves of the area and the perimeter of the eutectoid steel both show a sharp decrease up to two passes and a much smaller decrease after two passes, whereas the hyper-eutectoid steel shows a decrease over the entire deformation range, except for the initial small increase up to two passes. Contrary to the previous graphs, the data points in the graph of the roundness are more closely spaced, as can be observed in figure 4.24. This graph also exhibits a clear sigmoidal course of the curves of the eutectoid steel and the hyper-eutectoid steel with the roundness decreasing with increasing deformation. Notice that the majority of the evolution occurs between the second and the fourth pass, whereas little evolution occurs at deformation levels of up to two passes and more than four passes. And again, the curve of the hypo-eutectoid steel lacks a clear trend.

The deformed lamellae break up into numerous very small fragments that also have a large effect on the mechanical properties. These parameters are the major factors that determine the final submicrocrystalline grain size through their effect on the development of a dislocation network, which evolves to subgrains and submicrocrystalline grains. A good understanding of their behaviour during equal-channel angular pressing is therefore essential.

4.1.4 DISCUSSION

QUALITATIVE DISCUSSION OF THE MICROSTRUCTURAL ANALYSIS

The amount of literature on the microstructural analysis of materials processed by equal-channel angular pressing is growing fast. Nevertheless, there are still very few high-quality papers with detailed investigations on the microstructural evolution during subsequent passes. Thorough investigations on steel are non-existent until now. It is therefore often necessary for a proper comparison to rely on work published a few decades ago or on work that is less related to the current topic. In this light, the work done by Nijhof [61] and Wang [89-91] shares similarity with the experiments presented here. Hence, a comparison is made.

In the past few years Wang and co-workers published several papers on the microstructural development of an aluminium-copper alloy during equal-channel angular pressing. The material they used was an eutectic Al-33%Cu alloy with a lamellar structure, which they pressed from one to eight passes using route B_C at a processing temperature of 400 °C (673 K). Their die configuration consisted of two channels intersecting at an angle of 90° and having a round cross-sectional diameter of 13 mm. No information was given on the corner angle, but from the schematic drawing of their configuration it appears to be 0°. This configuration yields an effective deformation of $\varepsilon_{eff} = 1$ per pass.

Two decades earlier, Nijhof [61] conducted a detailed investigation to the microstructural evolution of lamellar structures by cold-rolling in a laboratory mill of three lamellar pearlitic steels

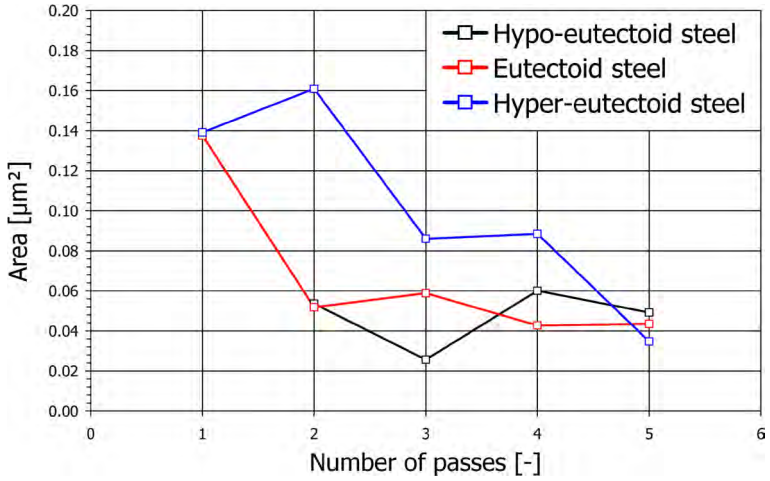

Figure 4.22. The area of the cementite lamellae as a function of the number of passes for the three high-carbon steels.

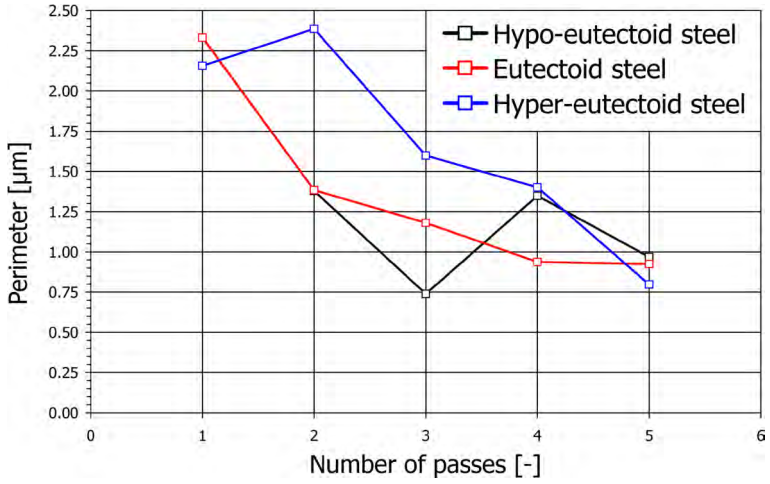

Figure 4.23. The perimeter of the cementite lamellae as a function of the number of passes for the three high-carbon steels.

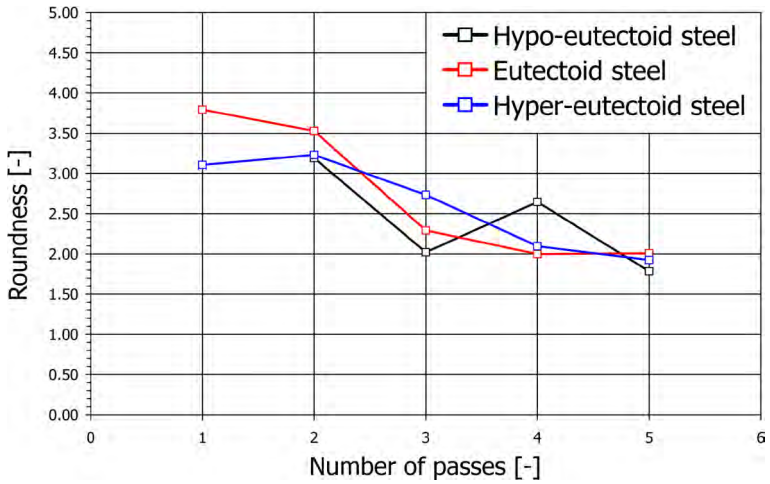

Figure 4.24. The roundness of the cementite lamellae as a function of the number of passes for the three high-carbon steels.

containing either 0.73, 0.82 or 0.85 weight-percent carbon. The amount of deformation he applied varied from 0 to 72 percent rolling reduction, equivalent to a total strain of $\varepsilon_{eff} = 1.27$.

The way in which the lamellar pearlite microstructure of the three high-carbon steels changes on a macroscopic scale resembles the one in which the lamellar eutectic aluminium-copper alloy tested by Wang et al changes. The microstructure of their alloy gradually changes from a lamellar microstructure to a duplex microstructure with fully spheroidised Al_2Cu-particles in an aluminium-matrix. Wang et al [91] distinguished three stages in this transformation process:

(1) Subdivision
Wang et al too observed the existence of narrow bands of fragmented lamellae, which they aptly named "canals", that cut through the lamellae colonies, thereby subdividing them into smaller lamellae blocks;

(2) Separation
This step involves the increasing number and size of the "canals". Consequently, it was found that the number of lamellae blocks increased, and that they were not connected to other neighbouring blocks, rather they evolved into isolated "islands";

(3) Shrinkage
In the final step of the transformation process the islands become progressively smaller through the fragmentation of the lamellae, which is especially strong at the interface between the lamellar "islands" and the surrounding equiaxed microstructure. This process continues until the entire microstructure is fully fragmented.

Contrary to Wang et al, a fourth stage is distinguished in the present investigation, namely the formation of shear bands. This additional stage precedes the other three stages. Since the "canals" were not observed in the initial condition, they must have formed as a consequence of the severe deformation of the material. The most likely explanation for the formation of the "canals" would be the creation of shear bands to accommodate for the macroscopic shear strain. The deformation then concentrates in these bands during subsequent passes, thereby causing them to fragment at a higher rate than the adjacent colonies. For unknown reasons Wang et al did not regard this as a separate stage. It is noteworthy to mention that Nijhof [61] observed the same mechanism of spheroidisation described here, though he did not go into detail on this particular subject.

Wang et al also found that the fragmentation occurred concurrently with the stages of subdivision and separation of the colonies. However, the rate at which their aluminium-copper alloy spheroidises differs from that of the three high-carbon steels. A fully and homogeneous equiaxed duplex microstructure is only established after eight passes ($\varepsilon_{eff} = 8$) by equal-channel angular pressing [89], whereas the three steels that are under investigation here, reach this state after only five passes ($\varepsilon_{eff} = 3.33$).

In the transition from a lamellar eutectoid microstructure to a fully spheroidised duplex microstructure, the pearlite exhibits various features that are typical for this phase. Detailed microstructural analysis has been carried out by Nijhof [61] and Wang et al [89-91] and their results show remarkable similarities with the results presented in this report. Wang et al discerned four typical deformation features in the microstructure of their lamellar eutectic alloy:

(1) Periodical bending
A feature where the lamellae are collectively bent, so that the lamellae remain largely parallel to each other. This features has a wavy appearance, due to the repeated bending.

(2) Periodical shearing
This feature is the same as periodical bending, except for the vertices. The lamellae change their orientation collectively and acutely in periodical shearing, whereas they change their orientation more smoothly in periodical bending.

(3) Parallel shearing
A feature where the direction of shear deformation runs parallel to lamellae, causing the formation of very narrow bands of often fragmented lamellae.

(4) Periodical cutting
This feature is characterised by repeated cutting of the lamellae. The direction of shear deformation runs (nearly) perpendicular to lamellae, causing the lamellae to fracture and otherwise deforming the lamellae very little.

In a previous article Wang et al [89] also regarded shear switching as an essentially separate feature, though later on [91] they categorised it as belonging to either periodical bending and periodical shearing. They also observed that shear banding is the most common deformation feature. This feature occurs in various forms, varying in intensity from mild to sharp, having a symmetric or asymmetric morphology, and with orientation angles in the range from approximately 10° to 90° with respect to the lamellae orientation. Furthermore, as concluded in this investigation and by Wang et al [89] the microstructural features may combine to form new and more complex features during subsequent deformation.

Nijhof [61] and Wang et al [89] describe that the shear cutting process that has been observed by them and in the present investigation, is essentially not a separate feature, but instead a form of very narrow shear bands that cut through the lamellae. The high-magnification TEM-image in figure 4.25 shows an example of such a narrow shear band cutting through the cementite lamellae. These narrow shear bands are typically only a few tenths of nanometres wide.

Both Nijhof [61] and Wang et al [91] concluded that the formation of the features described above "is an important mechanism for the lamellae to accommodate the severe plastic deformation". And also: "Extensive investigations and analysis indicates that the essential origin for the development of shear band is the interaction between the existing sheet-like anisotropy feature and the ongoing deformation. (...) When these sheet-like anisotropy features are strong enough, instability and deformation localisation may occur during the ongoing deformation, which leads to shear banding."

In addition to the typical features in the deformation microstructures described above, two features are found here that have not been observed by Wang et al. These are buckling and necking of the cementite lamellae. Furthermore, there is some controversy about the mechanism of formation of these features.

The mechanism for the occurrence of buckling demands three requirements to be met simultaneously. The first requirement is that all lamellae must be aligned parallel to the direction of deformation. Furthermore, a local state of normal compressive deformation must be present.

This can only be accomplished under principal stress conditions, since in that case no shear deformation occurs. Notice that in this case a shear deformation would cause the lamellae to be displaced in a direction parallel to the lamellae, but would not cause buckling of the lamellae. The third requirement states that the compressive deformation must exceed a certain threshold value or, equivalently, the lamellae must be too thin to resist a certain compressive deformation, which causes the lamellae to buckle and undergo extensive plastic deformation. Notwithstanding these demanding circumstances, this deformation feature is far from exceptional and may be observed in all three steels at moderately high deformation. Nijhof [61] too observed that buckling occurred when the lamellae were parallel to the direction of the applied force, i.e. parallel to the normal direction in his cold-rolling experiments. This suggests that the buckling observed in the present investigation may involve a compressive deformation component in addition to the shear deformation component.

Additionally, the mechanism for the occurrence of necking differs from that for the occurrence of buckling. The lamellae should be aligned parallel to the direction in which the elongation occurs. The cementite lamellae are capable of deforming plastically during necking, since the ferrite lamellae act as a hydrostatic medium that prevents the cementite lamellae from breaking. Necking of the cementite lamellae was rarely observed in the three high-carbon steels, although it has been observed by several other researchers [61,66]. These researchers found that cementite lamellae that were aligned parallel to the rolling direction [61] or to the drawing direction [66] broke into fragments of different length that became progressively smaller with deformation. In addition, they observed that both the thickness of the cementite lamellae and the interlamellar spacing decreased significantly.

Another observation that has also been made by Nijhof, are the size restrictions of the subgrains in the pearlite. Nijhof too found that the subgrains that are formed in the ferrite lamellae are bounded on two sides by the cementite lamellae. Furthermore, he found that many dislocations are formed at the interface between the ferrite and the cementite, as is shown in figure 4.26. The tendency to form dislocations is especially strong at the tips of the cementite fragments, because these are often sharp, causing them to be local points of stress concentration. This in turn leads to the creation of subgrain boundaries formed by tangled dislocations and cementite particles. It is therefore important to be able to control the fragmentation process of the cementite lamellae in order to control the subgrain dimensions and consequently the final submicrocrystalline grain size, too. A comparison with the results of the EBSD-analysis shall be made in section 4.4.

QUANTITATIVE DISCUSSION OF THE MICROSTRUCTURAL ANALYSIS

During the analysis of the microstructures, it was often found too difficult to clearly distinguish between fragmented regions and lamellar regions. Moreover, it was impossible to determine the fraction of lamellae that are almost fully broken and the fraction that are not (or less). Hence, it was also not possible to accurately define the terms "lamellar" and "fragmented". To avoid these difficulties it was necessary to create a separate series of images that were used only for the quantification of the lamellae dimensions in addition to the series of images that were used

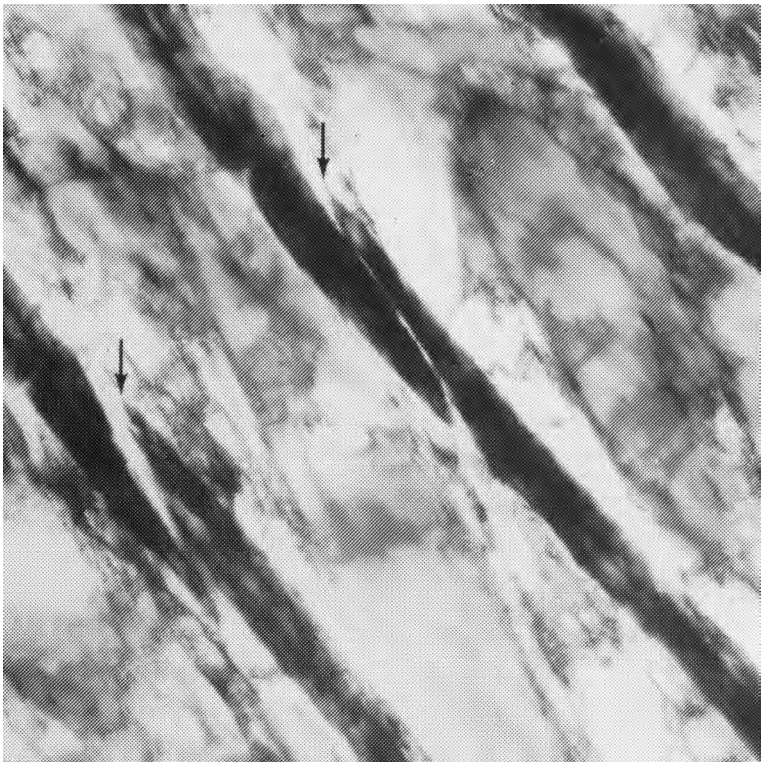

Figure 4.25. High-magnification transmission electron micrograph showing shear bands (indicated by the arrows) that cut through the cementite lamellae in a pearlite colony during cold-rolling. [61]

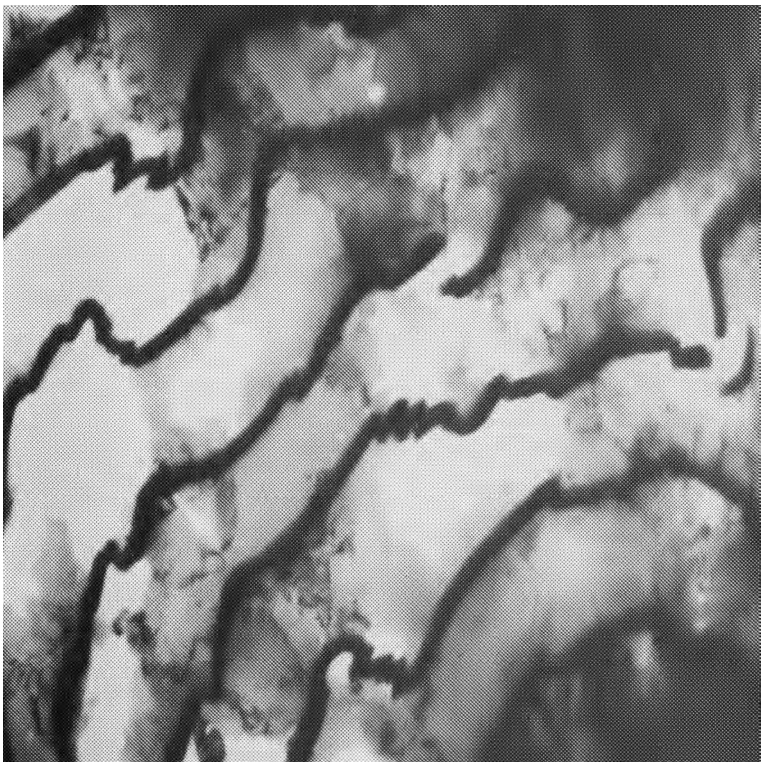

Figure 4.26. High-magnification transmission electron micrograph showing the ductile behaviour of cementite lamellae and the formation of dislocations at the ferrite-cementite interface. [61]

only for the qualitative microstructural analysis. The former series were taken from regions that were clearly fragmented.

Several calculations are made on the fragmentation behaviour with the purpose of showing how the shape and the size of the cementite lamellae change with increasing deformation, and showing which pass (-es) is (are) most effective in the breaking down of the lamellae. Since the surface, the circumference and the roundness are less clear for this purpose, the equivalent length and the equivalent width of a model lamella is calculated for each steel and after each pass. This is done by assuming that the lamellae were perfectly rectangular. The length (L_{eq}) and the width (W_{eq}) of a model lamella are calculated from the measured area (A) and the measured perimeter (P) using the following equations:

$$A = L_{eq} \cdot W_{eq} \tag{4.3}$$

$$P = 2 \cdot (L_{eq} + W_{eq}) \tag{4.4}$$

Equations 4.3 and 4.4 are solved simultaneously to yield the variables L_{eq} and W_{eq}, which are subsequently plotted in figure 4.27 and figure 4.28 as a function of the number of passes. The results exhibit a nearly constant course of the calculated widths for both the eutectoid and the hyper-eutectoid steels. The width of the lamellae in the eutectoid steel are indeed smaller than those of the hyper-eutectoid steel. This confirms the measurements listed in table 4.1. Additionally, the variation in the calculated width is less than the inaccuracy. This means that the dissolution of carbon from the cementite is negligible.

The graphs of the calculated length of both steels exhibit different trends. While the course of the graph of the eutectoid steel is clearly hyperbolic, that of the hyper-eutectoid steel is either sigmoidal or linear. The graph of the calculated length of the lamellae in the eutectoid steel starts off at about 1 µm after one pass and then quickly diminishes during subsequent passes. However, the decrease becomes progressively smaller until the length stabilises at just under 0.35 µm after four passes. No change in the length can be observed between four and five passes. The graph of the calculated length of the lamellae in the hyper-eutectoid steel exhibits a different behaviour. Initially, the length increases slightly from just under 1 µm after one pass to just above 1 µm after two passes, though this increase is not significant. At higher deformation, the length diminishes significantly and at a constant rate to a value of about 0.3 µm after five passes. No sign of stabilisation is detected here.

The fragmentation behaviour is best represented by the third curve, which presents the relative change in length between each pass. A value of 1 indicates there is no fragmentation taking place, while a value of more than 1 indicates that the fragmentation is in progress with the higher values representing a higher rate of fragmentation. The relative change of the eutectoid steel varies from about 1.7 between the first and the second pass to nearly 1 between the fourth and the fifth pass. The hyper-eutectoid steel shows the opposite behaviour with the relative change increasing from about 0.9 between the first and the second pass to nearly 2 between the fourth and the fifth pass.

The two high-carbon steels clearly exhibit different behaviour. Whereas the eutectoid steel exhibits an immediate onset of the fragmentation of the cementite lamellae, followed by a hyperbolic decrease, the hyper-eutectoid steel exhibits a delayed onset with a subsequent linear

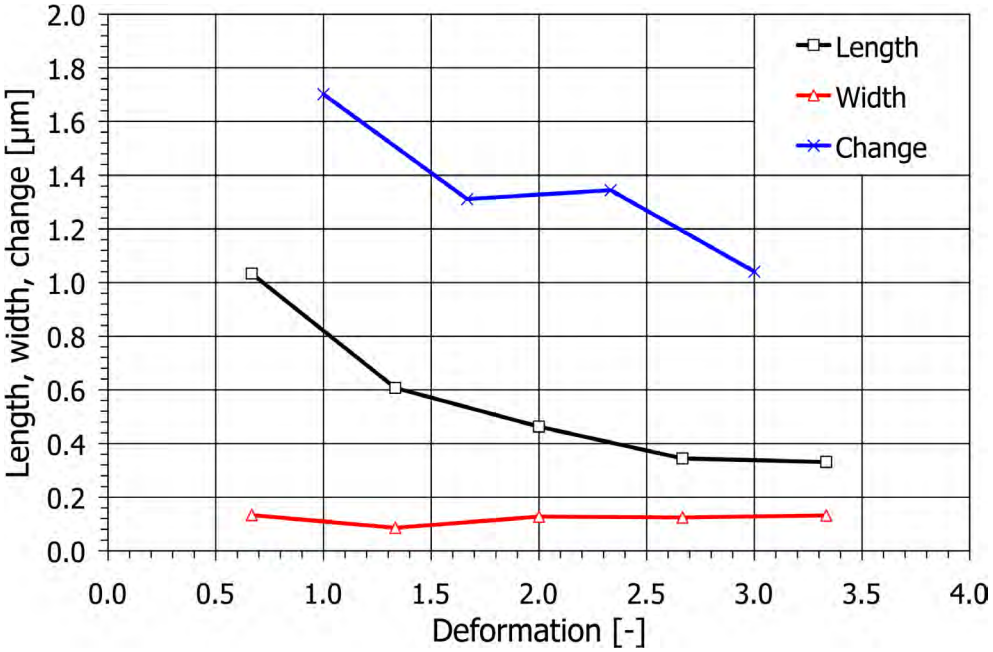

Figure 4.27. The calculated length [µm], width [µm] and the change of the length [-] between two subsequent measurements of a model lamellae in the eutectoid steel as a function of the accumulative deformation.

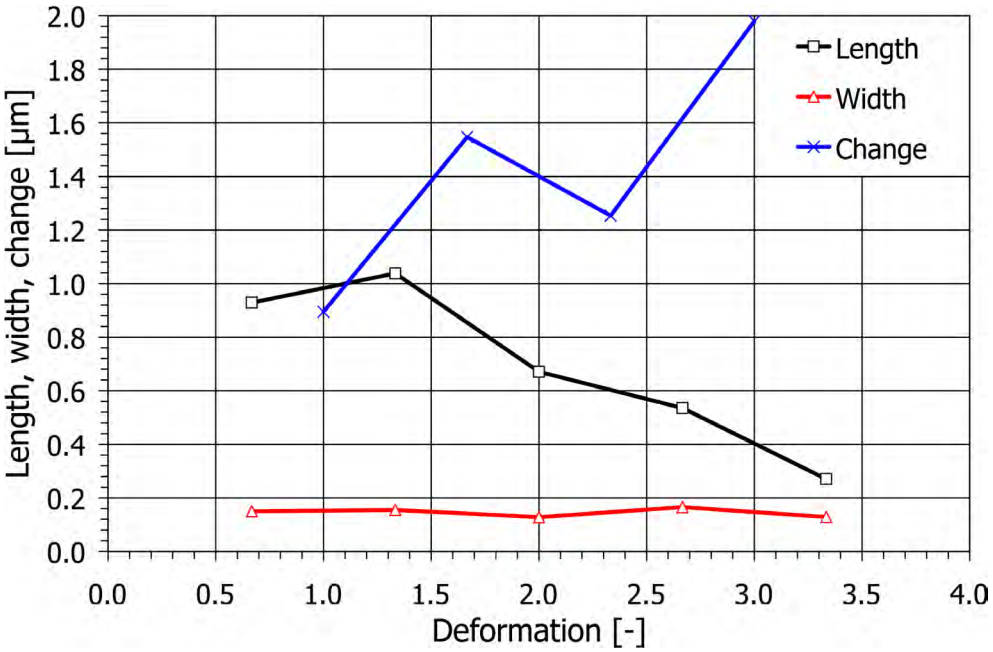

Figure 4.28. The calculated length [µm], width [µm] and the change of the length [-] between two subsequent measurements of a model lamellae in the hyper-eutectoid steel as a function of the accumulative deformation.

decrease. This delayed onset can be explained by the presence of thick lamellae, as opposed to the immediate onset in the eutectoid steel that is caused by thin lamellae. The lamellae in the hyper-eutectoid steel are nearly twice as thick as those in the other two steels, as was shown previously in section 4.1.3. Hence, it can be expected that the hypo-eutectoid steel would exhibit similar fragmentation behaviour as the eutectoid steel. The different behaviour of these two steels has also been observed at the opposite end of the deformation range. The lack of any significant change in the length of the lamellae in the eutectoid steel after four passes implies that this microstructure is fully fragmented. Contrarily, the fragmentation is still in progress after five passes in the hyper-eutectoid steel.

The present findings are in good agreement with the findings of Nijhof [61]. He found that the behaviour of the cementite depends on:

(1) The orientation of the lamellae;
(2) The thickness of the lamellae, and;
(3) The mode of deformation.

The often wavy or sharply bent cementite lamellae shown in section 4.1.2 and in the TEM-images by Nijhof, see for instance figure 4.26, are evidence of its ductility. The thickness of the cementite lamellae has a strong influence on their ductility. Nijhof observed many fractures by ductile necking of thin cementite lamellae. Contrarily, the coarse and hence stiffer cementite lamellae are able to resist more deformation before fracture occurs. The point of onset of fragmentation may therefore be regarded as the upper limit to the ability of the cementite lamellae to resist deformation. Additionally, the increased stiffness of the thick lamellae causes work-hardening to concentrate in the neighbouring weak ferrite, although dislocations have also been observed in deformed thick cementite lamellae, too. The latter observation is evidence of some plastic deformation. The fragmentation behaviour of the cementite lamellae and the work-hardening behaviour of the ferrite lamellae may interact in the generation of new dislocations and the obstruction of the movability of existing, gliding dislocations.

The mode of deformation greatly affects the fragmentation behaviour of the cementite. The brittle character of cementite frequently appears during tensile testing when shear cracking occurs. On the other hand, the ductile character appears during compressive testing when kink banding occurs even in coarse pearlite [61]. In this respect, the absence of brittle cracking during equal-channel angular pressing indicates that this process resembles compressive deformation more closely than tensile deformation.

A comprehensive survey of the fracture behaviour of the cementite lamellae is given in the paper by Langford [54], while a description of the nature of dislocations in deformed cementite can be found in the paper by Gil Sevillano [19].

CONCLUDING REMARKS

From the analysis of the microstructures it should first be concluded that studying the evolution of severely deformed microstructures is very well possible using scanning electron microscopy and an appropriate etchant.

The secondary electron images revealed that each of the three high-carbon steels responds differently to the severe deformation. The analysis of the microstructures revealed that often very complex microstructures are formed during equal-channel angular pressing. It also revealed that subgrains form in between the cementite lamellae of the pearlite. Consequently, the interlamellar distance affects the size of the subgrains and ultimately also the size of the submicrocrystalline grains. It is therefore important to determine the interlamellar distance and to know how to control the interlamellar distance.

Interesting findings have also been made after a comparison of the results presented in this report with the literature on this topic. Both similarities and differences with the results of Nijhof [61] were found. The materials used in both investigations are much alike in their chemical composition (both are plain high-carbon steels) and their crystal structure (both are body-centred cubic metals). On the other hand, the deformation mode is rather different. Whereas the cold-rolling performed by Nijhof involves a plane strain condition, the deformation mode during the equal-channel angular pressing involves a compressive shear strain condition. Likewise, there are striking similarities between the results from Wang et al [89-91] and the results presented in this report, despite obvious differences. Wang et al used the same device to apply the deformation, but the aluminium-copper alloy they tested had a face-centred cubic crystal structure. It must therefore be concluded that under the present conditions both the macroscopic mode of deformation and the crystal structure have only little influence on the evolution of the microstructure.

4.2 ELECTRON BACKSCATTERED DIFFRACTION ANALYSIS

Electron backscattered diffraction analysis was carried out with the purpose of following the changes in the microstructure during severe deformation processing. Orientation image maps, which are also known as EBSD-maps, are made of all three steels after each pass by equal-channel angular pressing. These maps are subsequently processed to yield statistical data on the boundary misorientation, the shape and the size of the subgrains and grains. As the routines for the processing of the maps and the analysis of the data are not standard and straightforward procedures, a separate subsection is devoted to the explanation of these procedures.

In the first section, the routines for the processing and the analysis of the data from the orientation image maps are laid out. The findings from the qualitative analysis of the microstructures as observed in the orientation image maps are presented in the second subsection, followed by a similar presentation of the quantitative analysis in the third subsection. The findings of the EBSD-analysis are discussed and compared with the literature on this topic in the fourth and final subsection.

4.2.1 PROCESSING AND ANALYSIS PROCEDURES

DATA ACQUISITION

All specimens for electron backscattered diffraction analysis were prepared in the same manner, as described in section 3.2. Following the preparation, the specimens were placed in the vacuum chamber of the scanning electron microscope for subsequent analysis.

The next step is the acquisition and indexation of the Kikuchi-patterns. Various detection parameters may be set in this stage, each of which has a complex effect on the results. Explanation of the effects of all the parameters is beyond the scope of this report. Therefore, it is decided to simply give an overview of the parameters that are used for the acquisition and the indexation of the Kikuchi-bands instead. These parameters are listed in table B11 in appendix B. Two parameters, however, have found to be of such great importance to the results that they should be mentioned here. These are the preselected phases and the step size.

The acquired band pattern is indexed automatically using a built-in list of possible solutions for one or more preselected phases. In most cases only the list of possible solutions for the ferrite phase was selected, but in two cases both lists for the ferrite and cementite phase were selected. The latter two have the advantage of yielding a higher fraction of indexation of the data points, but the disadvantage of a slightly longer analysis time per data point.

The other parameter that greatly affects the results is the step size. A step size of 0.05 μm was used for most of the maps, but for a few ones either a step size of 0.10 or 0.20 μm was used. On one hand, step sizes as small as these enable a clear observation of the development and further evolution of the subgrain structure and improve the accuracy of the determination of the (sub-) grain dimensions, but on the other hand, the maps that are created cover only a relatively small area that may not be representative of the entire microstructure. Hence, large orientation image maps of at least 600 by 600 data points were created in order to avoid this.

For the subsequent processing and initially also the analysis of the orientation image maps the computer programme VMAP was used. This purpose-built programme is developed by Professor F. J. Humphreys and his colleagues at the Manchester Materials Science Centre to process and analyse the orientation image maps produced by the hard- and software from HKL Technology.

During the stage of processing of the maps, it appeared to be undesirable to have both phases detected, since only the ferrite phase is the only phase we are interested in as far as the quantitative analysis is concerned. Unfortunately, the data processing software is unable to manipulate each phase separately and because of that the simultaneous processing of both the ferrite and the cementite phase will disrupt the statistics. This is especially the case for the deformed hyper-eutectoid steel in which large clusters of deformed cementite lamellae appear.

Despite the careful choice of the parameters for the acquisition of the Kikuchi-patterns, all the maps that were made, exhibited a considerable fraction of data points that were either not indexed or incorrectly indexed. Various reasons exist for the non-indexation or misindexation of a data point and the following list sums up the most important ones:

(1) The pattern of Kikuchi-bands of adjacent grains overlap at the grain boundaries, causing ambiguous solutions to which the detector is unable to find the correct one. This is a frequent cause of an error in the detection;

(2) Generally, only the Kikuchi-bands from the selected phase (-s) are indexed. However, it occasionally occurs that two phases share a common or very similar solution, for instance aluminium and silicon. In such a case, the wrong Kikuchi-pattern may be chosen, which leads to a misindexed data point.

(3) The lattice strains in severely deformed materials may be so intense that the lattice may deform slightly on a local scale, causing the Kikuchi-pattern to become blurry. This causes a slight twist in the orientation of the Kikuchi-bands, which complicates the determination of the orientation of the lines. It may then be advantageous to select more bands and decrease the threshold intensity for the indexation. This increases the probability of finding the correct solution, although this also slightly increases the analysis time per data point.

DATA PROCESSING

The misindexed data points have the tendency to be grouped in irregularly shaped clusters of only a few data points that are completely surrounded by high-angle boundaries, and consequently they are considered as grains. Previous research by Bowen [7] and by Shin et al [63,79-85] has shown that grain sizes smaller than 0.20 µm are not achieved. Thus, taking into account the use of step sizes of 0.05, 0.10 and 0.20 µm, these particles are too small to be real grains at all the deformation levels. Since the clusters compose a considerable fraction, they also have a proportionally large effect on the (sub-) grain size and the boundary misorientation. Figure 4.29 shows an example of the effects of these clusters on the boundary misorientation distribution. Graph (a) shows the distribution prior to the removal of misoriented points with two sharp peaks: one around 30 ° and one around 60 ° in misorientation. Graph (b) shows the corrected distribution after the removal. Notice the different scales of the fraction and distribution. Due to the unrealistic size of the "grains" and their detrimental effect on the statistics, it is decided to remove all the misindexed data points. Subsequently, the orientation image maps contain a large number of fragmented subgrains that again disturb the statistics. This is caused by the heterogeneous nature of the deformation, due to which some subgrains deform at a higher rate than others. The misindexation tends to be concentrated in the highly deformed subgrains. Further processing of the maps is needed and the data processing software has several functions available to do so. The following paragraphs list descriptions of these functions:

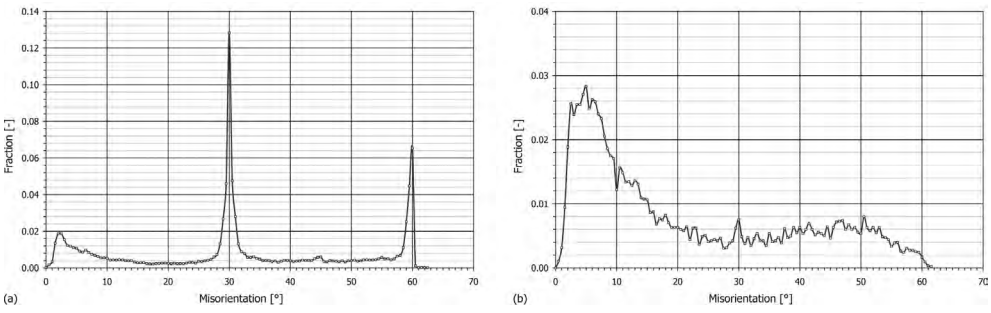

Figure 4.29. Graphs showing the boundary misorientation distribution (a) before and (b) after processing of the data from the orientation image map of the hypo-eutectoid steel after three passes.

(1) Removal of suspect data points

This function is used to remove dubious data points. These are defined as singular data points that are fully surrounded by either non-indexed data points or indexed data points of the same orientation (i.e. having an orientation difference of less than the threshold value for high-angle boundaries), such that the singular data point is separated by a high-angle boundary from the surrounding indexed data points. Note that a singular data point will not be removed if it is surrounded by at least one indexed data point that has an orientation that differs from the other adjacent indexed data points. A similar situation occurs when the orientation difference between the singular data point and the surrounding indexed data points is less than the threshold value for high-angle boundaries;

(2) Subgrain reconstruction

It is often necessary for the analysis of orientation image maps to treat the non-indexed data points as if they were indexed, for instance when data points at the boundaries appear non-indexed or when large parts of the subgrains are non-indexed after the removal of the misindexed data points. A method of subgrain reconstruction (named "cleaning" in the data processing programme) has been developed that addresses this problem. The average orientation of the data points surrounding the non-indexed data point is calculated and assigned to the non-indexed data point. This method is composed of four different sub-methods that differ in the extent to which they reconstruct the subgrain: "level-0 cleaning" requires at least four indexed neighbouring data points for the non-indexed data point to be indexed, "level-1 cleaning" requires at least three indexed data points, etc. Caution should be exercised when applying this reconstruction routine when reliable quantitative data is to be obtained from orientation image maps.

(3) Orientation averaging

Orientation averaging involves the application of a modified Kuwahara-filter to smoothen the small orientation differences within a subgrain. This serves to increase the angular resolution [7,30] and to remove the misorientation noise at very small misorientations of typically less than 1.5 °. Due to the latter effect, the course of the subgrain boundaries becomes clearer and the fraction of low-angle boundaries decreases slightly in favour of the fraction of high-angle boundaries. The filter was originally developed by Kuwahara et al [53] for image enhancement and later modified by Humphreys et al [30] for orientation averaging. The filter has two varieties: the Kuwahara-4 (K4) filter and the Kuwahara-9 (K9) filter. The routine calculates the average orientation of the four (K4-filter) or eight (K9-filter) square blocks of data points surrounding a central data point. Provided the misorientation with the surrounding data points does not exceed the preselected lower threshold value for low-angle boundaries, the orientation of the central data point is replaced by the average orientation of the surrounding four or eight data points. The modified Kuwahara-filters carry out five consecutive cycles of orientation averaging. The process can be stopped at any time after each cycle. The greatest effect occurs during the first cycle.

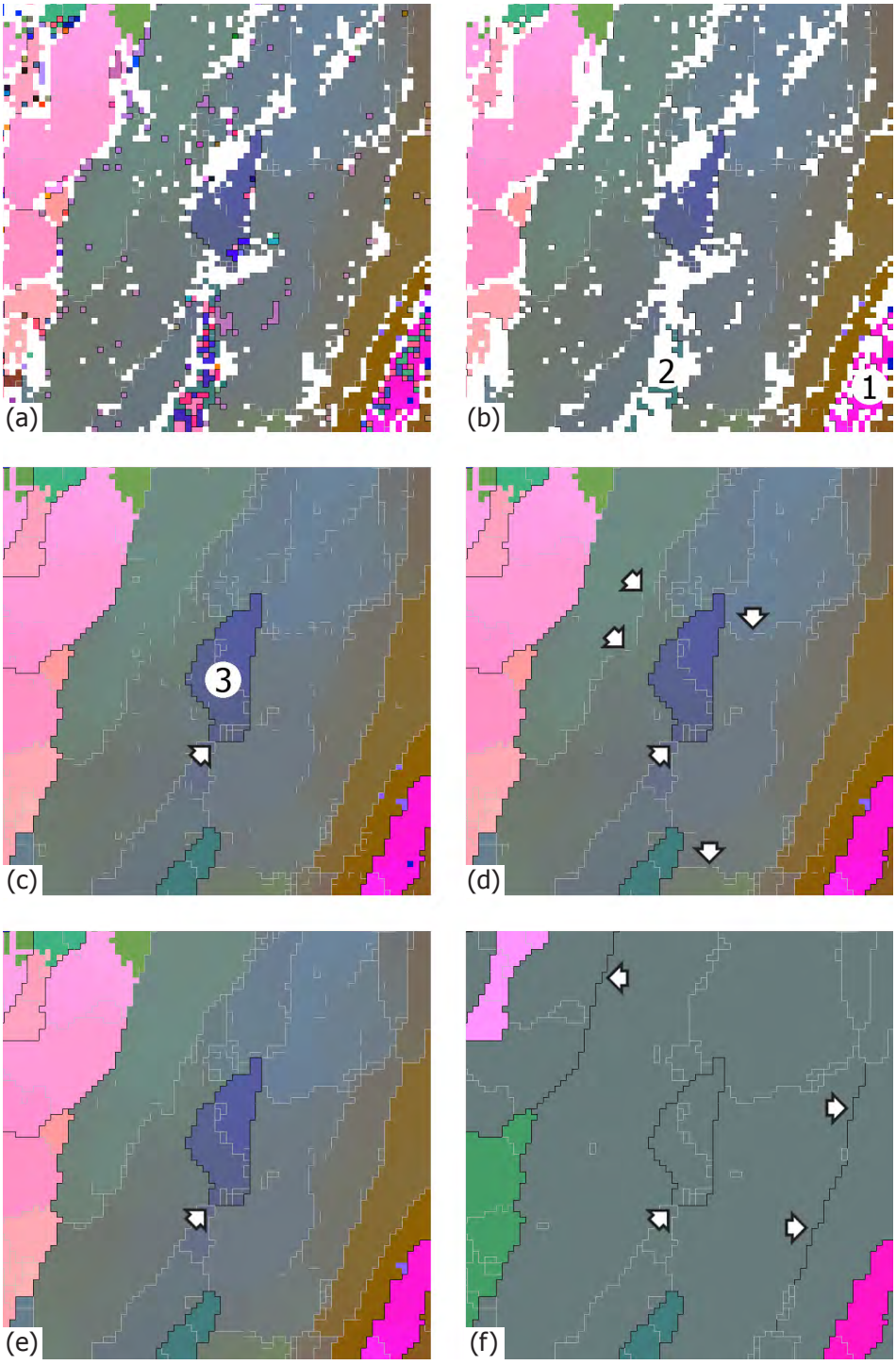

Figure 4.30. Effect of different processing parameters on the orientation image maps. (a) Original and unprocessed map, showing the data points in Euler colours and the low- and high-angle boundaries, (b) the same map after removal of the suspect and misindexed data points, (c) as (b) but with subsequent grain reconstruction, (d) as (c) but with a single cycle of orientation averaging, (e) as (c) but with five cycles of orientation averaging, and (f) the same map as in (e), but showing the grain map.

(4) Reallocation of small subgrains

Often tiny subgrains occur in the process of formation of a subgrain structure. In this stage of deformation, single dense dislocation walls (DDW's) split into two to form microbands (MB's), where the interior of the MB's is formed by tiny subgrains [27]. The DDW's and MB's alternate each other and form discontinuous chains that divide the subgrains. As with the clusters of misoriented data points, there are numerous tiny subgrains that consequently disrupt the statistics. Hence, they should be removed. In order to do so, a processing routine has been developed that re-incorporates all the subgrains that have a size (in data points) of less than a certain pre-selected threshold value into the adjacent subgrain that has the smallest misorientation difference with the reallocated subgrain. Note that this filter only applies for subgrains whose boundary misorientation exceeds the lower threshold, but does not exceed the upper threshold for low-angle boundaries. It should also be noted that the actual orientation of each data point is not altered!

The procedure developed here is applied to all the orientation image maps. Figure 4.30 shows sample maps of several stages in the processing. Figure 4.30a shows an orientation image map in the initial unprocessed condition. This map clearly exhibits a large number of non-indexed data points (indicated in white) and misindexed data points (the tiny clusters that are surrounded by black lines). The first step involves the removal of these suspect and misindexed data points. The suspect points are automatically identified and removed by the data processing software, whereas the misindexed points have to be manually identified and removed. The results of this step can be observed in figure 4.30b. Two small areas are noteworthy, namely the subgrain in the bottom right corner (labeled '1') and the non-indexed area in the lower middle (labeled '2'). Notice that due to the removal these subgrains are divided into very small clusters that share no connection with each other. Thus, to reconnect the clusters a reconstruction of the subgrains is carried out. This involves expanding the subgrains to such an extent that the subgrain fragments that are created due to the removal of suspect and misindexed data points are now re-incorporated into the subgrain, thereby leaving the original microstructure as much as possible in the original shape. In order to accurately quantify the (sub-) grain size, several assumptions were made. It was assumed that in the initial maps all non-indexed data points, both in the interior and surrounding the subgrains, were at the position where cementite was and that the fraction of non-indexed data points elsewhere was negligible. Contrarily, the non-indexed data points in a manually cleaned map comprise both points where cementite is at and where misindexed ferrite points were at. Care should be exercised not to expand the subgrains too much, since the subgrains are partially bounded by cementite lamellae. Consequently, a compromise has to be found between the selected "level of cleaning" and assigning an orientation that corresponds to ferrite to a non-indexed data point that is known to be cementite. A "level-1 cleaning" was chosen at first, but this reconstruction option left too many fragments isolated and too many non-indexed data points in the interior of the subgrains. Therefore, a full "level-3 cleaning" was chosen to accomplish adequate subgrain reconstruction. However, this expands the subgrains somewhat too much, requiring the subsequent application of a correction factor. The result of

the subgrain reconstruction is shown in figure 4.30c. Notice that the (sub-) grain in the middle (labeled '3') is surrounded by high-angle boundaries (indicated in black), except for a tiny portion where the boundary misorientation is low-angled in nature (indicated by the arrow).

The small orientation gradients are subsequently smoothened by applying a K9-filter. In order to establish the extent of orientation averaging that should be applied, i.e. the number of cycles, several trial runs were carried out to determine the amount of removal of the misorientation noise with respect to removing actual subgrain boundaries. This is shown in figure 4.30d and figure 4.30e, in which orientation image maps after a single cycle and after five cycles of smoothening are depicted. During the first cycle most of the misorientation noise was removed, while after subsequent cycles small parts of the boundaries were destroyed (as indicated by the arrows), while others were created. Because of these effects, it was decided to apply only one cycle of the Kuwahara-9 filter to all the maps. Following the orientation averaging, the reallocation routine was applied. It was chosen to reallocate all the subgrains that are less than five data points in size, since subgrains this small are unrealistic given the level of deformation that was applied and the step sizes that were used.

A survey of all the parameters that are used to process the orientation image maps can be found in tables B1 and B2 in Appendix B.

DATA ANALYSIS

The data from the processing of the orientation image maps is stored and subsequently used for the statistical calculations. The following paragraphs explain the routines that were used.

After the last step of processing of the orientation image maps, the area of each subgrain, which is equivalent to the total number of data points, is determined. The equivalent circular diameter (ECD) is then calculated from the equivalent square length (ESL), which equals the square root of the area (A), using the equation:

$$\mathrm{ECD} = \frac{2}{\sqrt{\pi}} \cdot \sqrt{A} = \frac{2}{\sqrt{\pi}} \cdot ESL \tag{4.5}$$

As mentioned previously, the area should be corrected for the number of non-indexed and misindexed data points. During processing of the cleaned map, the subgrains are expanded too much and to correct for this, the area is multiplied by a correction factor (f_c) using the equation:

$$A_c = A_{nc} \cdot f_c \tag{4.6}$$

The correction factor is defined as the ratio of the percentage of indexed data points before processing (f_b) to the percentage of indexed data points after processing (f_a):

$$f_c = f_b / f_a \tag{4.7}$$

Substituting equations 4.2 and 4.3 into equation 4.1 and converting the equivalent circular diameter in data points into the equivalent circular diameter in micrometers yields:

$$ECD_c = \frac{2}{\sqrt{\pi}} \cdot \sqrt{f_c} \cdot ESL \cdot \Lambda \quad (4.8)$$

Where ECD_c is the corrected equivalent circular diameter in micrometers, ESL is the equivalent square length in data points, Λ is the stepsize in micrometers and f_c is a dimensionless correction factor. Before calculating the average and standard deviation values, a filter was applied to the area, the equivalent circular diameter and the lengths in the normal and the extrusion direction. This filter compares the value of equivalent circular diameter to a preset threshold value. If the value of the equivalent circular diameter is less than the threshold value of 0.25 μm, the values of all parameters are omitted from the statistics. The application of this filter appeared to be a necessity in order to enhance the reliability of the statistics.

In addition to the parameters mentioned above, the percentage of low-angle and high-angle boundaries is also calculated. These values are calculated from the orientation image maps that are processed, therefore the grains and subgrains are expanded until they impinge upon each other. Consequently, the resulting values for the percentage of low-angle and high-angle boundaries are not the real physical values, but should be considered as an indication of how much the subgrains have rotated with respect to each other.

PLOTTING MAPS

Following the processing of the data, orientation image maps were plotted. The maps were divided into two categories, namely maps for qualitative analysis and maps for quantitative analysis. The sole purpose of maps of the first category is to get a good impression of what the microstructure looks like under the different conditions that were applied. Getting reliable statistical data from these maps is not a criterium. The purpose of the maps of the second category is on the other hand to get reliable statistical data. Therefore, care has been exercised to develop an analysis procedure with which reliable results can be produced.

In the figures depicting the orientation image maps (figures 4.31 to 4.41), the top map always shows the pixel maps in Euler colours with the addition of the boundaries, but without orientation averaging. The bottom maps on the other hand show the grain maps in Euler colours, again with the addition of the boundaries and after applying the previously discussed routines. Note that the pixel maps show colours that may differ slightly for each data point, regardless of the size and orientation of the (sub-) grain that they belong to, whereas in the grain maps each grain is depicted in a single colour, despite the slight orientation differences that actually occur.

In all the maps shown, low-angle boundaries are indicated in grey and high-angle boundaries are indicated in black. Low-angle boundaries are defined here as boundaries having a minimum misorientation of 1.5° and a maximum misorientation of 15°, whereas high-angle boundaries are defined as boundaries having a misorientation of 15° or more. The lower threshold value of 1.5° is chosen to reduce the level of misorientation noise. Further information of this topic can be found in the review by Humphreys [31] and the PhD-thesis by Bowen [7].

4.2.2 QUALITATIVE ANALYSIS

Orientation image maps of the three high-carbon steels were made after each pass. Since the microstructures of the three steels after the first two passes are similar, only two maps of these conditions are shown. The maps of the steels that are deformed to three, four or five passes on the other hand are distinctly different and hence maps of each of these conditions are shown. The orientation image maps can be found in figures 4.31 to 4.41.

EVOLUTION OF THE GRAIN STRUCTURE

Typical examples of the microstructure as observed from the orientation image maps of the three steels in the early stages of deformation are shown in figures 4.31 and 4.32. These two figures were taken from the eutectoid steel after one pass and the hypo-eutectoid steel after two passes. Figure 4.31 shows part of two adjacent grains that are separated by a high-angle boundary (labeled 'GB'). Apparently, a single pass (equivalent to an effective deformation of $\varepsilon_{eff} = 0.67$) does not cause significant changes of the microstructure, since the grains have retained much of their originally polygonal shape. Small changes may be observed, such as the small areas adjacent to the grain boundary (labeled 'A') that have a different orientation than the surrounding material. These are perhaps small regions that deformed differently to accommodate the severe deformation close to the grain boundary. After two passes ($\varepsilon_{eff} = 1.33$), the microstructure exhibits a considerable fraction of deformed pearlite lamellae (labeled 'P'), as can be seen in figure 4.32. These appear as wavy patterns in which the ferrite is indexed and the cementite is not. In addition, several flattened and deformed ferrite grains (labeled 'F') can also be observed. After three passes ($\varepsilon_{eff} = 2.00$), a mixed behaviour may be observed. Maps of this condition are depicted in figure 4.33 (hypo-eutectoid steel), figure 4.36 (eutectoid steel) and figure 4.39 (hyper-eutectoid steel). The orientation image maps of the steels in this condition exhibit both areas with a lamellar nature and areas with a fragmented nature. In the former type it can be seen that the severe deformation causes the lamellae to undergo extensive distortion, though they still have retained their lamellar nature. Instances of this type can be observed in figure 4.33a (the area indicated by the 'P' with a large number of tiny fragments) and figure 4.36a (the area in the bottom left corner indicated by the 'P'). The fragmented nature is characterised by numerous tiny bits of cementite that have broken up from the pearlite lamellae. This can be observed in figure 4.36a (indicated by the non-indexed data points mainly in the right half) and in figure 4.39b (indicated by the tiny fragments inside the grains). A noticeable difference between the deformed and the fragmented lamellae is that the grains in which the fragmented nature prevails, are often more of less elongated, while the deformed grains tend to be irregularly shaped. During subsequent deformation in the fourth and the fifth pass ($\varepsilon_{eff} = 2.67$ and $\varepsilon_{eff} = 3.33$), the grains and the subgrains become progressively more elongated and cementite lamellae from the pearlite become progressively more fragmented until after five passes the microstructure contains fragmented cementite lamellae only, as can be observed in e.g. figure 4.41. This behaviour is typical for all three steels, although it is less obvious in the hypo-eutectoid and the hyper-eutectoid steels. The orientation of the grains

in these two steels is further complicated by the presence of the soft ferrite phase in the hypo-utectoid steel and by the hard cementite clusters (labeled 'C') in the hyper-eutectoid steel. Also, the boundary misorientation of the (sub-) grains varies and is affected more by the phases that are present than by the deformation. An example of this behaviour can be found in figure 4.34, which shows an orientation image map of the hypo-eutectoid steel after four passes. The ferrite grains are much more flattened and elongated than the pearlite grains. Another example can be found in figure 4.41, which shows an orientation image map of the hyper-eutectoid steel after five passes. The large clusters of deformed cementite lamellae clearly cause a random size and shape of the grains. Additionally, no clear morphological orientation can be observed.

After three or more passes, one can observe that a lamellar structure has formed. The grains at this stage in the deformation are rather elongated and have a width that varies greatly from one area to another. The length of the grains cannot be determined in most cases, because most grains extend beyond the limits of the maps. This can be observed in all three steels, though in the hyper-eutectoid steel this is complicated by the formation of the clusters of deformed cementite lamellae. These clusters occur as massive second-phase "particles" that subdivide the elongated grains in much smaller and irregularly shaped grains (see figures 4.39 to 4.41), though no clear difference in subgrain shape and size can be observed. However, the effect of the cementite clusters on the grains is only noticable if the clusters are at least several micrometers thick.

EVOLUTION OF THE SUBGRAIN STRUCTURE

The formation and subsequent evolution of the subgrains develops similarly to the grains. The orientation image maps of the three high-carbon steels exhibit the start of the development of a dislocation network that is typical of the early stages of subgrain formation. For instance, the microstructure of the eutectoid steel after one pass exhibits only a few dense dislocation walls (see figure 4.31). After two passes, the microstructure shows that a deformation substructure starts to form (see figure 4.32). Some of the dense dislocation walls have developed further to become subgrain boundaries that are predominantly discontinuous.

On further deforming the steels, the fraction of subgrains rapidly increases. The formation of a deformation substructure has progressed such that in all three steels a lot of the subgrains have continuous boundaries after three passes. The formation of these boundaries is, however, not complete and a considerable fraction of discontinuous subgrain boundaries can still be observed. Consequently, these will appear as large subgrains, partially because of the processing of the maps. One of the characteristics of the large subgrains is that they have the tendency to occur mostly in the centre of the grains. The cause of this is that the amount of deformation is mostly lower in the centre of a grain than at the grain boundaries where various local strains have to be accommodated. Examples of these are labeled 'L' and can be found in figures 4.33, 4.34 and 4.36. The formation of dislocation cell walls is aided by the cracked cementite lamellae, whose tips act as sources for the generation of dislocations [61]. Local differences in the dislocation density cause a certain heterogeneity in the subgrain dimensions. This can be clearly observed in the map of the hypo-eutectoid steel after four passes (see figure 4.34).

Upon processing of the map, the uncompleted formation of a dislocation cell wall around a subgrain leads to the formation of excessively large subgrains, because of the definition that is used by the analysis software. This effect has to be taken into account for in the statistical analysis. On the other hand, the formation of the subgrain structure is complete after five passes and in this stage only well-developed subgrains can be seen.

The fraction of high-angle boundaries can be seen to increase with increasing deformation after the establishment of a subgrain structure. Initially, the grains are separated from each other by high-angle boundaries, whereas the subgrains are separated from each other by low-angle boundaries. The misorientation between the subgrains gradually increases during subsequent deformation and hence the fraction of high-angle boundaries increases at the expense of the fraction of low-angle boundaries. Furthermore, these newly formed high-angle boundaries tend to occur predominantly parallel to the extrusion direction, though a smaller fraction of high-angle boundaries is formed in the normal direction.

DEFORMATION HETEROGENEITY

Another noticeable feature is the occurrence of local differences in deformation behaviour, which become more pronounced with increasing deformation. The orientation image map of the hyper-eutectoid steel after four passes (see figure 4.40) shows several clear examples of this behaviour. In the immediate vicinity of the clusters of deformed cementite lamellae a large number of very small grains of various different orientations can be observed. Contrarily, at some distance away from the clusters, the microstructure seems more homogeneous and similar to that of the hypo-eutectoid and the eutectoid steels after four passes (see figures 4.34 and 4.37) with clearly less subgrain misorientations that exceed the limit of high-angle boundaries.

Similar microstructural behaviour can be observed in the hypo-eutectoid steel. Here, local differences in deformation behaviour occur at the interface of the ferrite and the pearlite. Due to this the orientation gradually changes and tiny grains are formed. For instance, figure 4.32 shows several very small pearlite grains (labeled 'P') in between the two ferrite grains. Figure 4.32a shows that their colour (light brown) differs only slightly from the colour of the large pearlite grains (darker brown), which indicates they originally were part of the large pearlite grains and therefore had the same orientation.

Contrary to the other two steels, the eutectoid steel deforms more homogeneously, while the other two exhibit large local differences in the subgrain size. However, it can still be that the hypo-eutectoid and the hyper-eutectoid steel become fully homogeneous at higher strain levels.

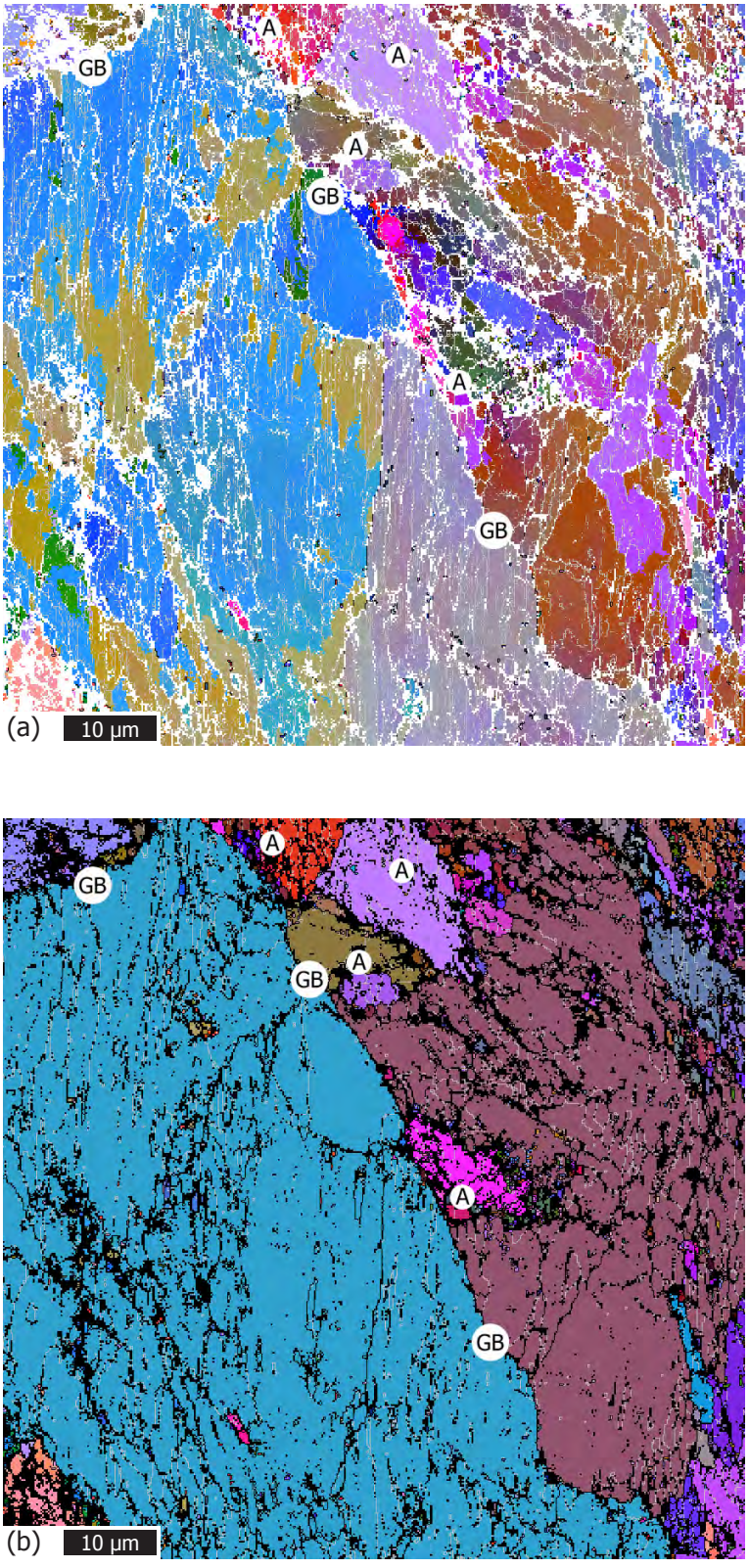

Figure 4.31. Orientation image maps of the eutectoid steel after one pass, showing (a) the microstructure and (b) the corresponding grain structure.

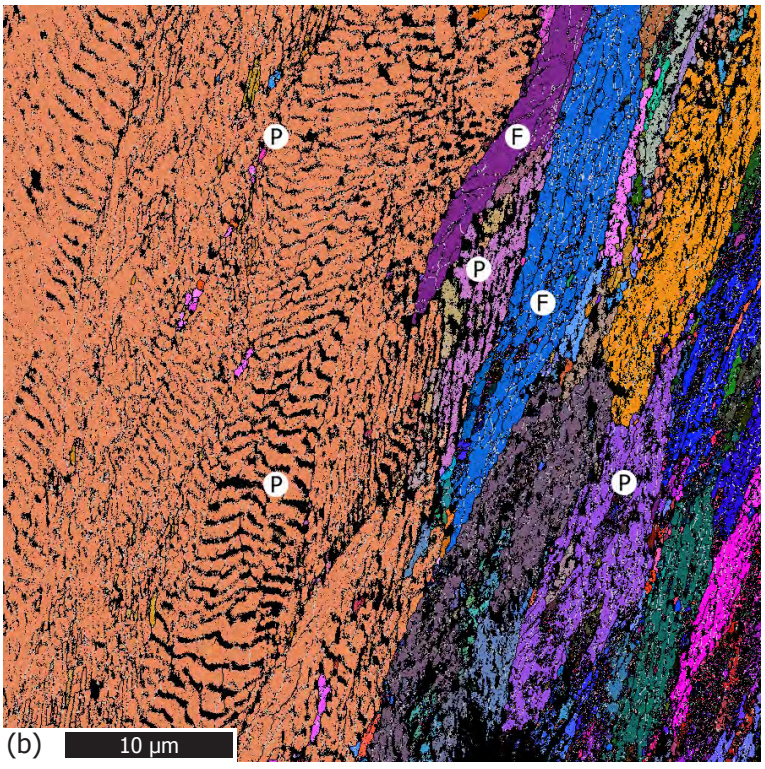

Figure 4.32. Orientation image maps of the hypo-eutectoid steel after two passes, showing (a) the micro-structure and (b) the corresponding grain structure.

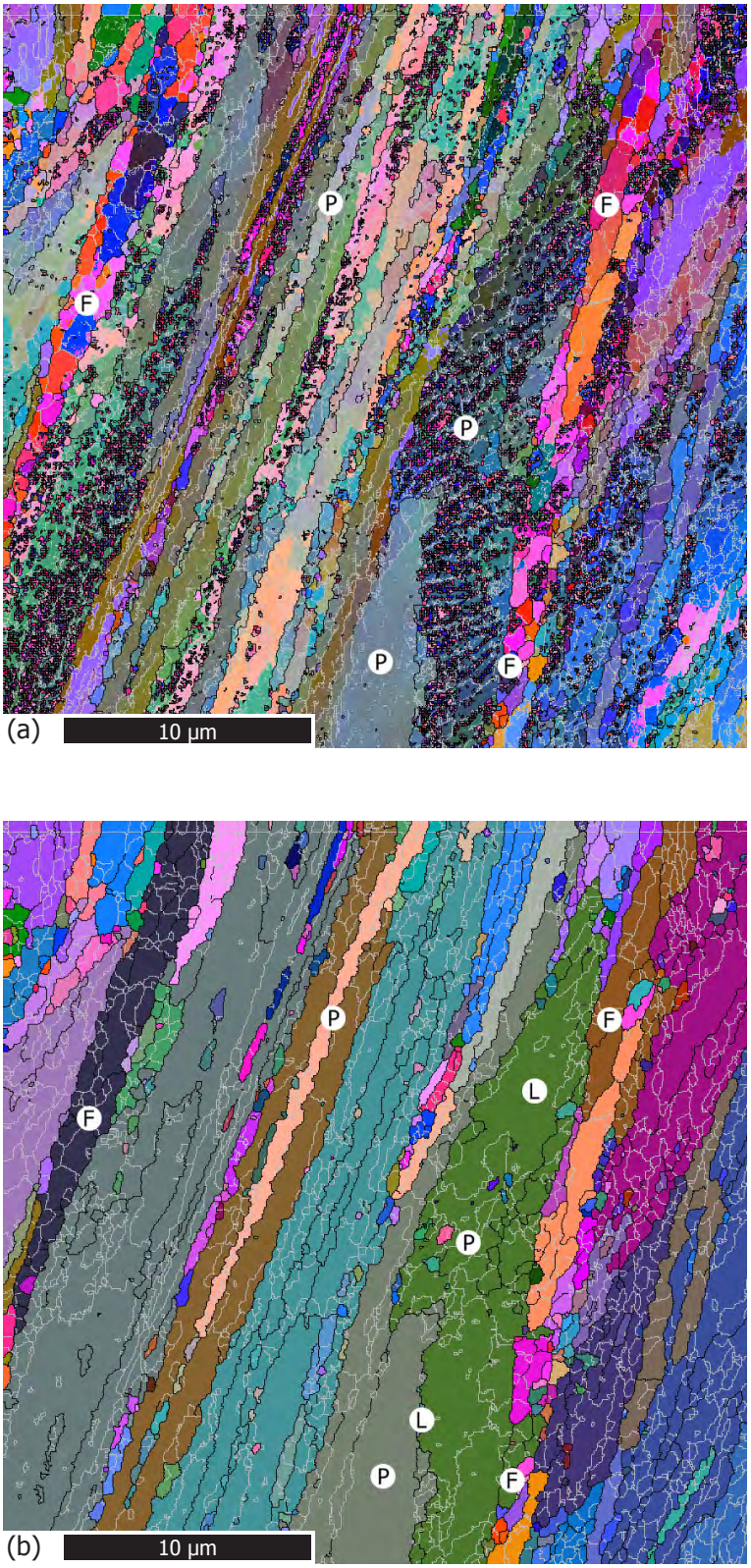

Figure 4.33. Orientation image maps of the hypo-eutectoid steel after three passes, showing (a) the microstructure and (b) the corresponding grain structure.

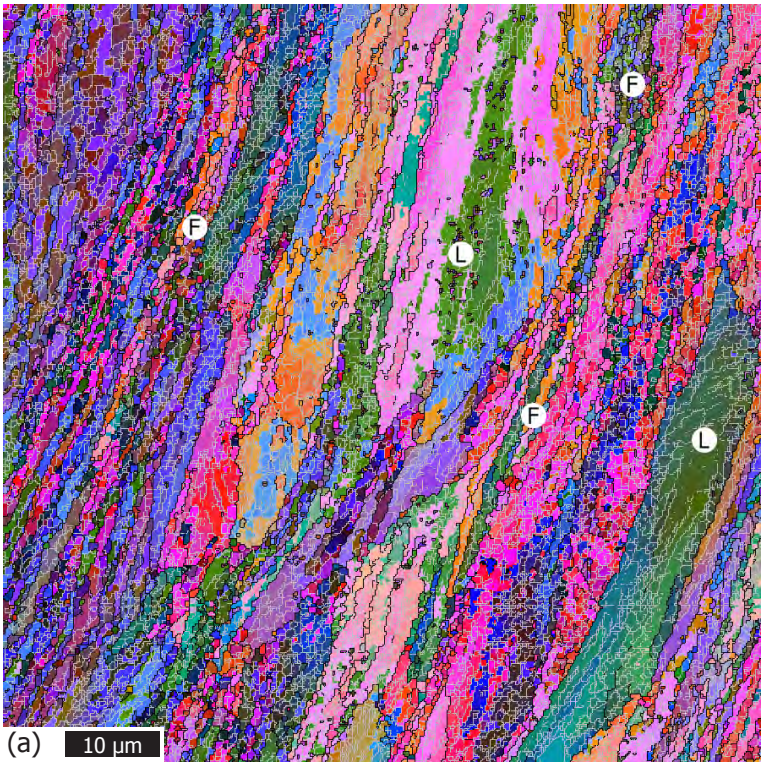

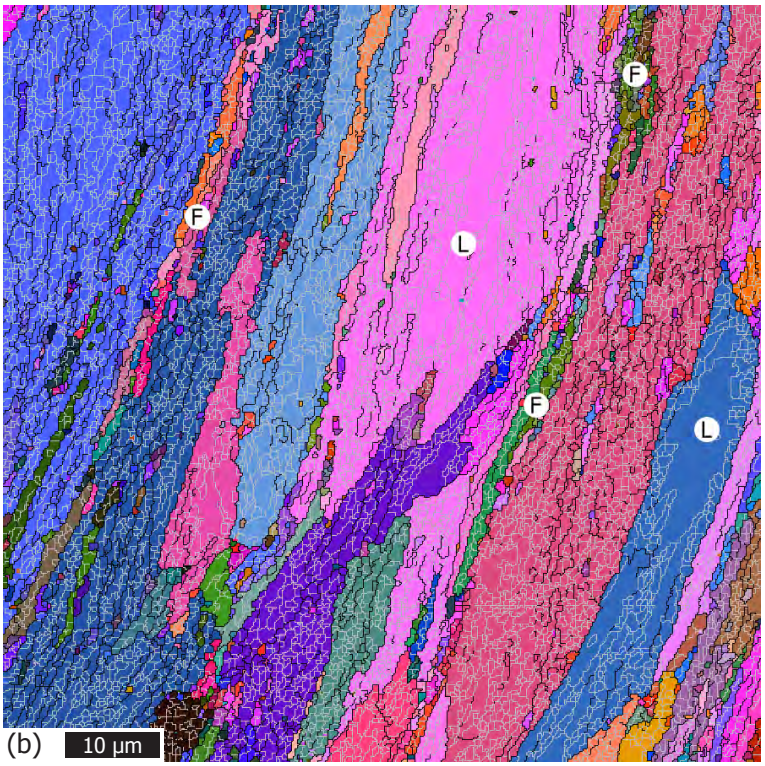

Figure 4.34. Orientation image maps of the hypo-eutectoid steel after four passes, showing (a) the micro-structure and (b) the corresponding grain structure.

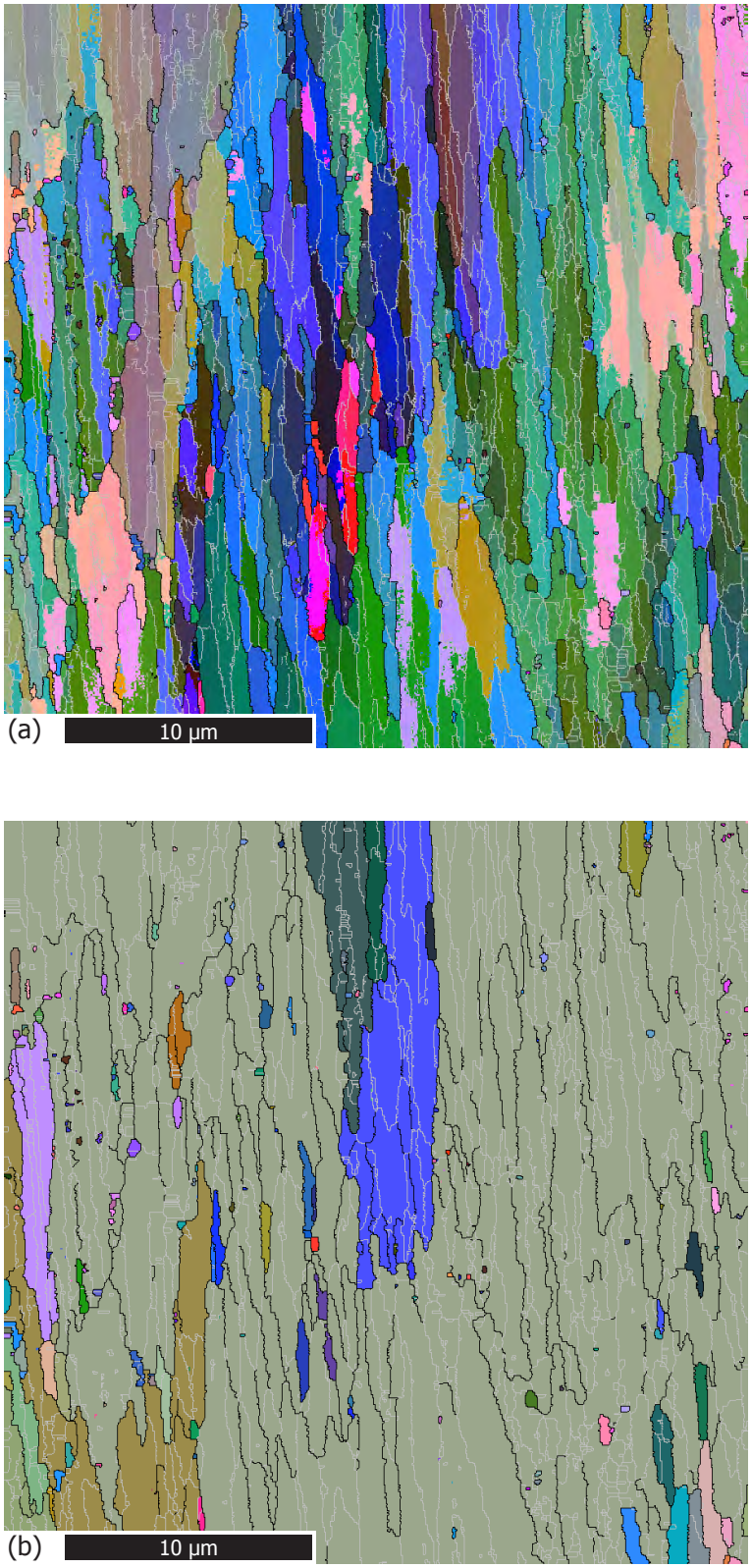

Figure 4.35. Orientation image maps of the hypo-eutectoid steel after five passes, showing (a) the microstructure and (b) the corresponding grain structure.

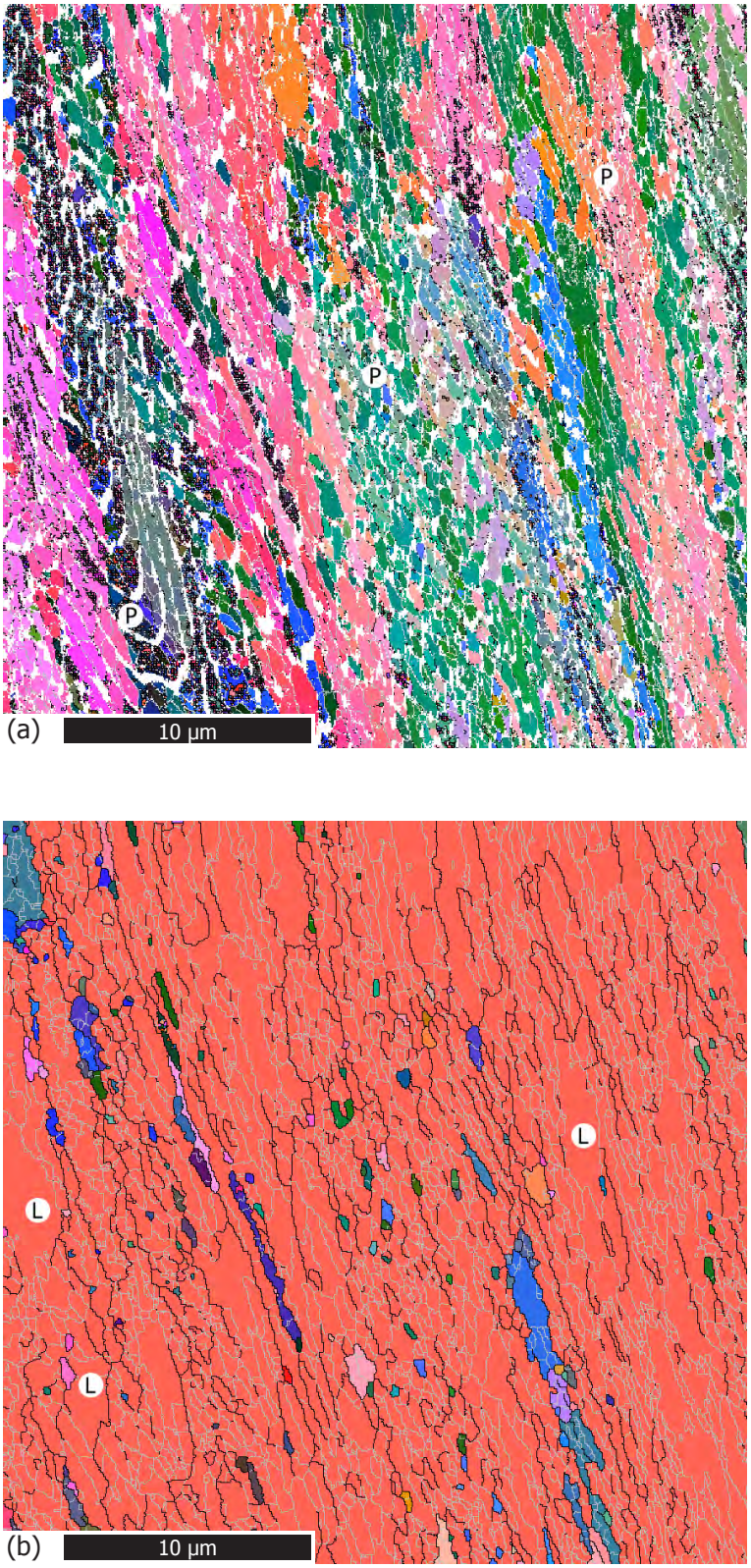

Figure 4.36. Orientation image maps of the eutectoid steel after three passes, showing (a) the microstructure and (b) the corresponding grain structure.

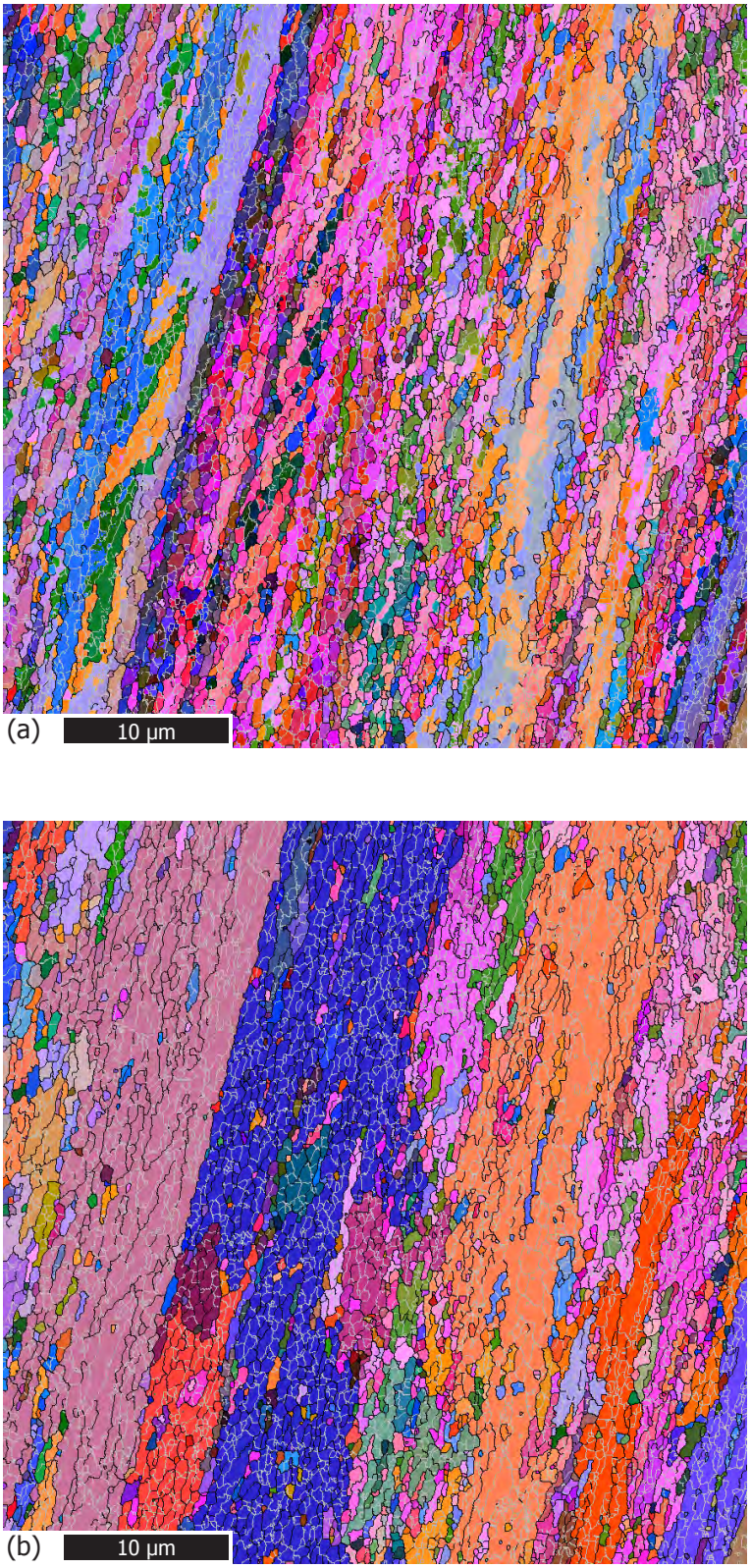

Figure 4.37. Orientation image maps of the eutectoid steel after four passes, showing (a) the microstructure and (b) the corresponding grain structure.

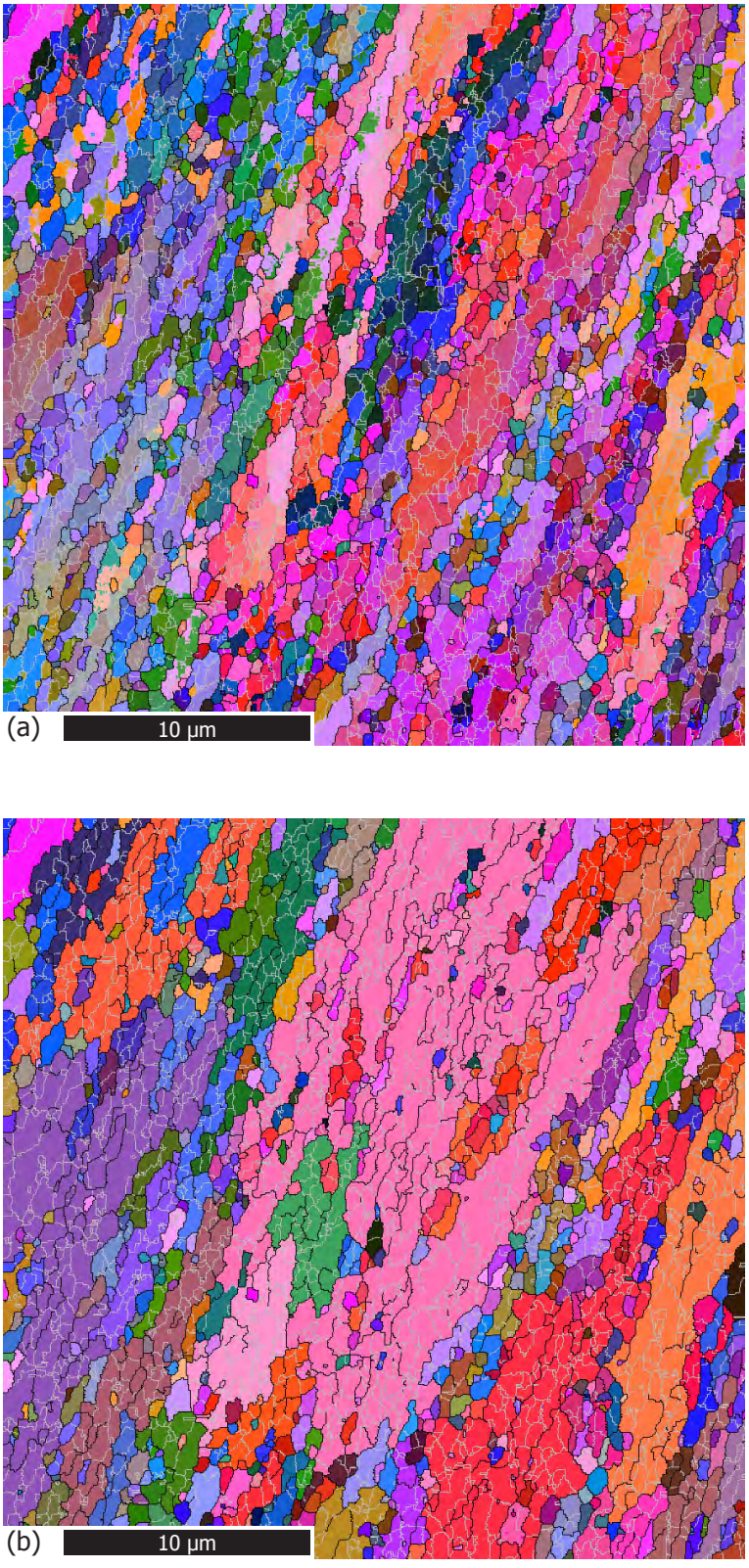

Figure 4.38. Orientation image maps of the eutectoid steel after five passes, showing (a) the microstructure and (b) the corresponding grain structure.

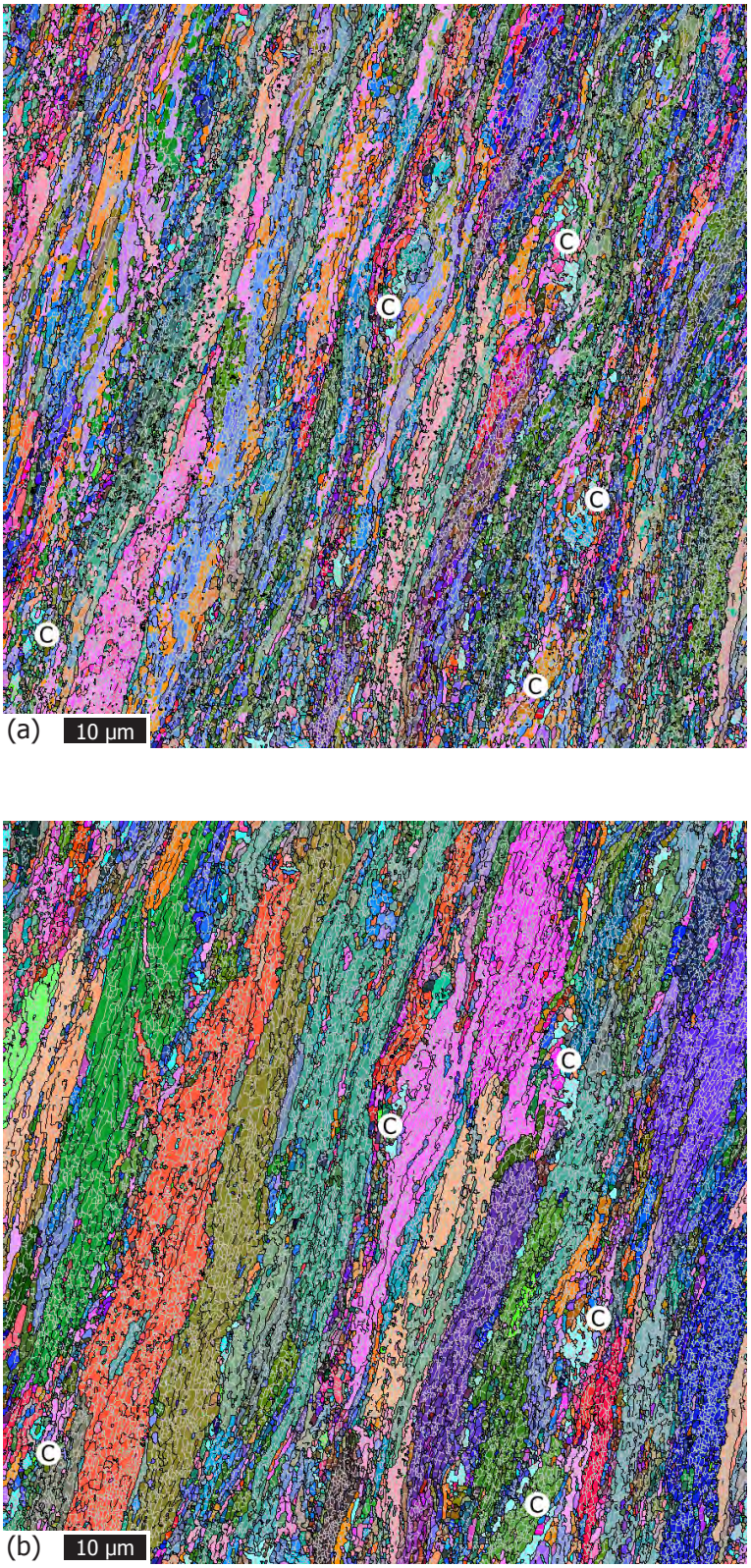

Figure 4.39. Orientation image maps of the hyper-eutectoid steel after three passes, showing (a) the microstructure and (b) the corresponding grain structure.

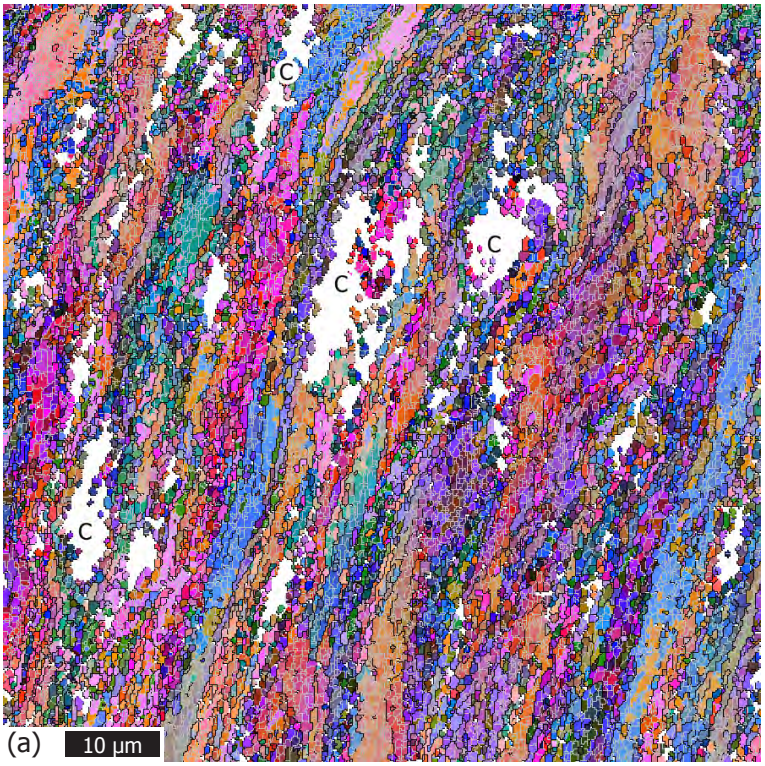

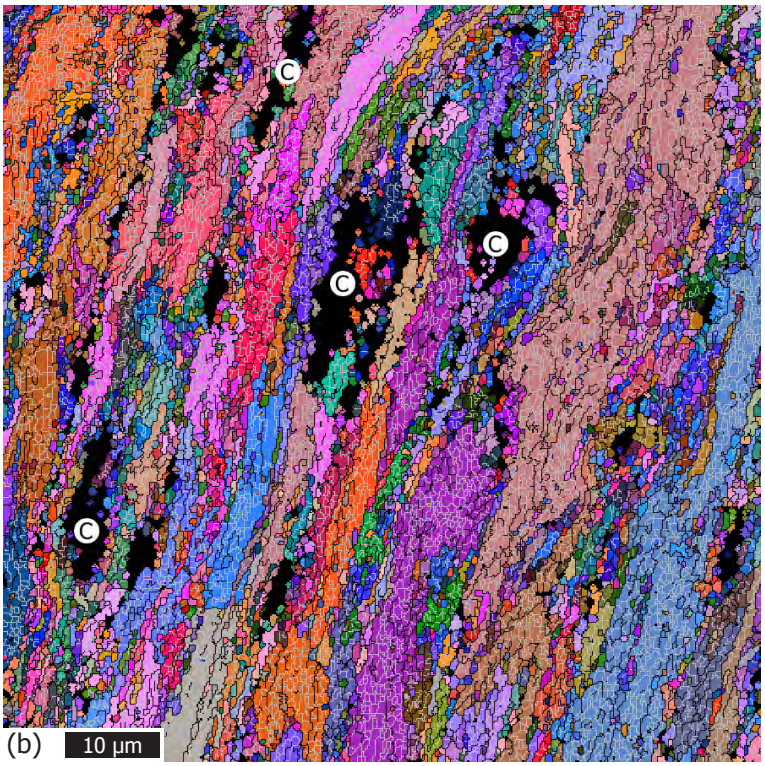

Figure 4.40. Orientation image maps of the hyper-eutectoid steel after four passes, showing (a) the microstructure and (b) the corresponding grain structure.

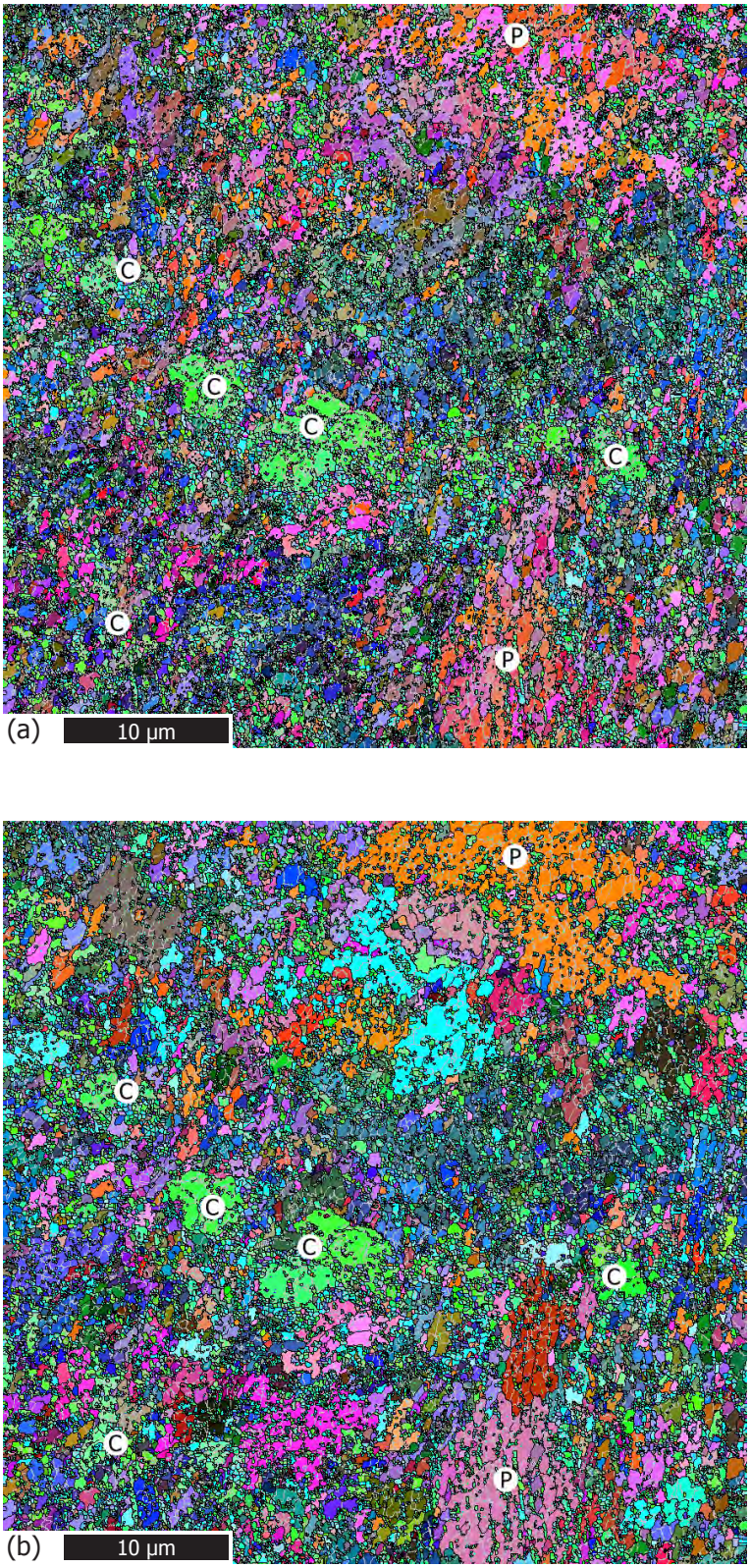

Figure 4.41. Orientation image maps of the hyper-eutectoid steel after five passes, showing (a) the microstructure and (b) the corresponding grain structure.

4.2.3 QUANTITATIVE ANALYSIS

In this section, a quantification will be given of the characteristics discussed in the previous section. A complete survey of the results of the statistical analysis of the orientation image maps can be found in tables B3 to B10 in Appendix B, whereas a summary is shown in table 4.5.

ISSUES DURING THE ANALYSIS

The selection of the threshold value that is applied to the (sub-) grain dimensions in order to get rid of the considerable number of tiny (sub-) grains is an issue in the quantitative analysis. In order to assess the influence of the threshold value on the results and to select the correct threshold value, three different threshold values were chosen and their results were compared with each other. The results are listed in tables 4.2 to 4.4. These tables show that the results of the hypo-eutectoid steel and the hyper-eutectoid steel do not change when using 0.10 μm and 0.25 μm. This is due to a combination of the stepsize (namely 0.20 μm for the hypo-eutectoid and the hyper-eutectoid steels and 0.05 μm for the eutectoid steel) and the fact that the same threshold value was used for the reallocation of small subgrains (less than five pixels for all maps), due to which only one data point was measured below the threshold value.

Another trend is that the values of the area, the equivalent circular diameter and the length in the normal direction of the hypo-eutectoid steel are in all cases (much) higher than those of the eutectoid and the hyper-eutectoid steels. The latter two steels themselves exhibit somewhat complex behaviour, namely for threshold values of 0.10 or 0.25 μm the values of the eutectoid steel are lower than those of the hyper-eutectoid steel, whereas for a threshold value of 0.50 μm both steels have comparable results. The threshold value apparently has a large effect on the outcome of the results.

The size distribution graphs of the parameters that are under investigation here, are all asymmetric Gaussian-like curves, having a narrow left half of the peak and a broad right half of the peak. Two typical examples of which are shown in figure 4.42. If a threshold value of 0.50 μm were chosen, the vast majority of the grains would have been disregarded and the results would not have been representative. On the other hand, if 0.10 μm were chosen, the application of the threshold value would have a negligible effect on the results and a lot of the unrealistically small (sub-) grains would have remained. This problem can be overcome by selecting a threshold value of 0.25 μm, since in this case the unrealistically small (sub-) grains are disregarded, yet enough data remains to make the results representative.

DATA INTERPRETATION

Following the selection of the correct threshold value, all the data from the orientation image maps were processed. The following equation was used to calculate the average equivalent circular diameter of the grains and the subgrains:

$$ECD_{avg} = \frac{1}{N} \cdot \sum_{i=1}^{i=n} ECD_i \tag{4.9}$$

Table 4.2. Average values for selected parameters for the hypo-eutectoid steel after four passes.

Threshold		0.10 µm		0.25 µm		0.50 µm	
		Grains	Subgrains	Grains	Subgrains	Grains	Subgrains
A	μm^2	4.97	0.48	5.62	0.48	7.58	0.55
ECD	µm	1.08	0.71	1.20	0.71	1.49	0.77
L_{ND}	µm	1.13	0.63	1.20	0.63	1.47	0.68
L_{ED}	µm	2.05	6.19	2.19	6.20	2.65	6.21

Table 4.3. Average values for selected parameters for the eutectoid steel after four passes.

Threshold		0.10 µm		0.25 µm		0.50 µm	
		Grains	Subgrains	Grains	Subgrains	Grains	Subgrains
A	μm^2	0.77	0.14	0.96	0.18	1.95	0.35
ECD	µm	0.54	0.37	0.64	0.44	0.97	0.64
L_{ND}	µm	0.49	0.32	0.61	0.41	1.01	0.65
L_{ED}	µm	0.86	1.64	1.01	1.68	1.34	1.88

Table 4.4. Average values for selected parameters for the hyper-eutectoid steel after four passes.

Threshold		0.10 µm		0.25 µm		0.50 µm	
		Grains	Subgrains	Grains	Subgrains	Grains	Subgrains
A	μm^2	1.02	0.31	1.07	0.31	1.44	0.36
ECD	µm	0.76	0.60	0.79	0.60	0.95	0.66
L_{ND}	µm	0.76	0.53	0.79	0.53	1.14	0.72
L_{ED}	µm	1.20	3.21	1.22	3.21	1.61	3.23

Table 4.5. Statistical data from the quantitative analysis of the orientation image maps for the grains (subscript G) and the subgrains (subscript SG) in the three high-carbon steels, including the average (subscript avg) and standard deviation values (subscript stdev) of the equivalent circular diameter (ECD) and the percentage of low-angle (% LAGB) and high-angle (% HAGB) boundaries. (*) = not available.

		Hypo-eutectoid steel			Eutectoid steel			Hyper-eutectoid steel		
ECAP-passes		3	4	5	3	4	5	3	4	5
$ECD_{G, avg}$	µm	0.88	1.20	(*)	(*)	0.64	0.70	0.70	0.79	0.42
$ECD_{G, stdev}$	µm	1.37	2.39	(*)	(*)	0.90	0.78	0.99	0.86	0.34
$ECD_{SG, avg}$	µm	0.51	0.71	0.72	0.55	0.44	0.46	0.47	0.60	0.38
$ECD_{SG, stdev}$	µm	0.36	0.33	0.43	0.29	0.18	0.18	0.19	0.18	0.16
% LAGB	%	49	57	53	63	42	41	44	40	15
% HAGB	%	51	43	47	37	58	59	56	60	85
Map width	µm	30	80	30	30	45	30	90	80	45
Map height	µm	30	80	29	30	45	30	90	80	45

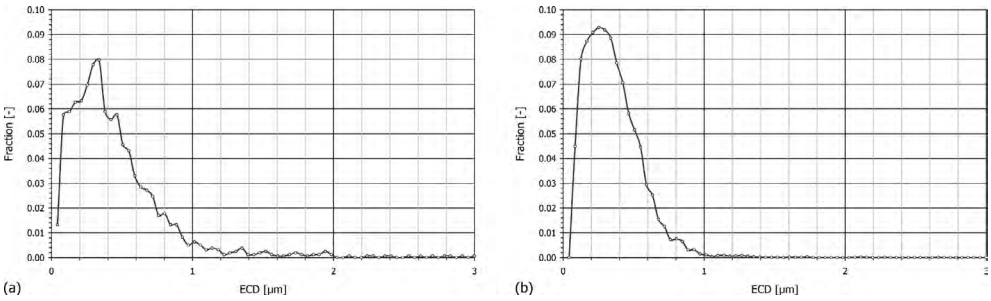

Figure 4.42. Distribution of the equivalent circular diameter of (a) the grains and (b) the subgrains in the eutectoid steel after four passes.

In this equation, ECD_{avg} is average equivalent circular diameter in µm, n is the total number of (sub-) grains.

Table 4.5 shows that data is missing for the grain dimensions of the hypo-eutectoid steel after five passes and for the eutectoid steel after three passes. This is due to a combination of the excessively large grains that were measured (see figures 4.35 and 4.36) and the utter instability of the data processing software. The detection of both the ferrite and the cementite phase during the acquisition of the Kikuchi-bands turned out to be a bad choice. Due to the inability of the data processing software to process or analyse one phase at the time the numerous tiny cementite fragments are also counted. This results in greatly reduced and incorrect (sub-) grain dimensions of the hyper-eutectoid steel after three and five passes. The results from these two orientation image maps are therefore omitted from further quantitative discussions.

The trends in the data listed in table 4.5 show different behaviour. The equivalent circular diameter of the grains in the hypo-eutectoid steel exhibits a sharp increase and that of the eutectoid steel a small increase with increasing deformation. Contrarily, the evolution of the equivalent circular diameter of the subgrains in the hypo-eutectoid steel exhibits a gradual increase, whereas the eutectoid steel shows a sharp decrease between the third and fourth pass, but remains constant between the fourth and the fifth pass. No trends in the evolution of the hyper-eutectoid steel could be observed, since only the measurements after four passes are reliable. However, both the subgrains and the grains of the hypo-eutectoid and the hyper-eutectoid steel after four passes appear to be larger than those in the eutectoid steel in the same condition. The cause for the larger grains lies in the size of the orientation image maps of these conditions, which is much larger than that of the other conditions. This in turn bring about an increase of the importance of the larger grains, i.e. the grains that previously extended beyond the boundaries of the map, with respect to the smaller grains. The size of the subgrains is not affected by the map size. The larger subgrain dimensions of the hypo-eutectoid steel after four passes can be attributed to the incompleted formation of the subgrain boundaries. These findings are supported by the standard deviations of both the grain and subgrain dimensions.

It was mentioned in section 4.2.2 on the qualitative analysis of the orientation image maps that the total number of subgrains rapidly increases in the initial stages of deformation. A concomitant effect is the increase of the amount of low-angle boundaries. On the other hand, the amount of high-angle boundaries, which initially separate only the grains from each other, remains constant. However, the boundary misorientation begins increase gradually, once a sub

grain structure is established. The fraction of high-angle boundaries can then be seen to increase at the expense of the fraction of low-angle boundaries. Furthermore, it seems that the phases have a larger effect on the boundary misorientation than the carbon content, since the largest difference in boundary misorientation occurs between the hypo-eutectoid and the eutectoid steel, whereas these two steels have the smallest difference in carbon content.

When comparing the average values of the boundary misorientation, the results may be misleading, since they are highly affected by the threshold value that is chosen to distinct low-angle boundaries from high-angle boundaries. In order to get a reliable impression, the boundary misorientation distribution is plotted in graphs. Figure 4.43 depicts the boundary misorientation distribution of the three high-carbon steels deformed to four passes (ε_{eff} = 2.67). These graphs can be divided into two ranges: the first range includes the low-angle boundaries and the moderately high-angle boundaries with misorientation angles in the range from 15 ° to 30 °, whereas the second range contains all the high-angle boundaries with misorientation angles in excess of 30 °. All three graphs show a clear peak in the misorientation in the first range, meaning that the microstructure of the three steels is still predominantly low-angled in nature. The high values of the percentage of high-angle boundaries listed in table 4.5 seem to contradict the low-angled nature, but is simply due to the choice of the threshold. Furthermore, the peak in the misorientation distribution of the hypo-eutectoid steel is significantly larger than that of the other two steels. Hence, the microstructure is in a less well-developed stage of deformation or -equivalently- the rate of evolution of the microstructure of the hypo-eutectoid steel stays behind with the other two steels. Additionally, the peaks of the eutectoid and the hyper-eutectoid steels are equally large, though the peak of the latter has shifted to slightly higher misorientations and also exhibits a slightly higher fraction of high-angle boundaries. This confirms the previously made findings that the fraction of high-angle boundaries is larger in the hyper-eutectoid steel than in the other two steels due to the presence of the cementite clusters.

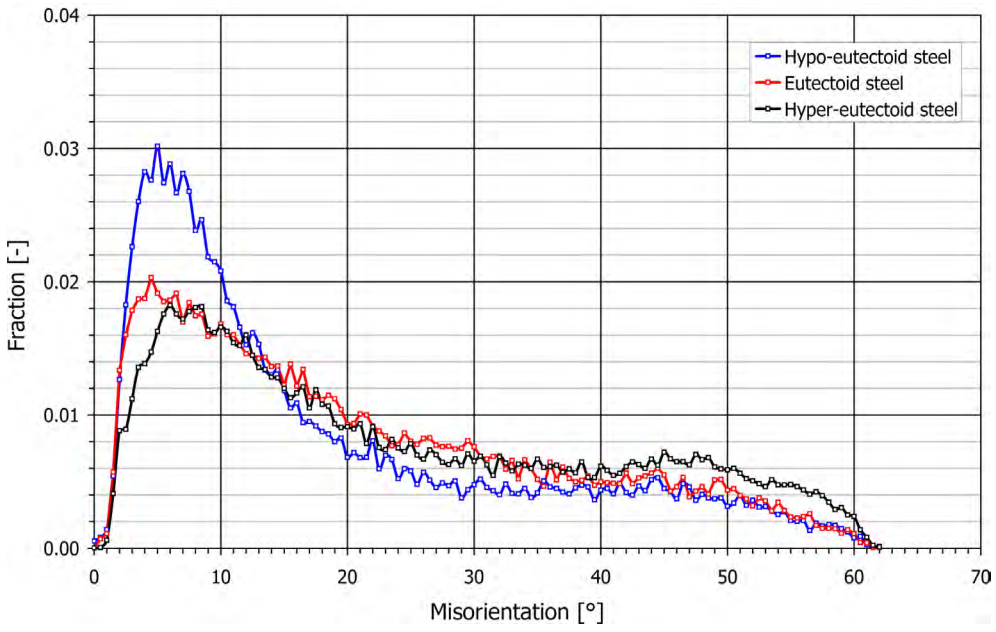

Figure 4.43. Graphs showing the boundary misorientation distribution after processing of the orientation image maps of the three high-carbon steels after four passes.

As mentioned in the previous section, the microstructure of the steels reveals some strain localisation. This microstructural heterogeneity expresses itself in the hypo-eutectoid steel after three or more passes by a tendency of the deformation to concentrate in the ferrite and in the pearlite immediately adjacent to the ferrite. A similar observation is made in the maps of the hyper-eutectoid steel. The latter maps show that after three or more passes the cementite clusters are surrounded by small (sub-) grains, see for instance figure 4.40. The local differences in the microstructural heterogeneity in the steels are shown by the boundaries and the size of the subgrains. In areas where the local deformation rate is higher, i.e. in the softer areas, the fraction of high-angle boundaries is larger than in areas with lower deformation rates. In addition to that, it may be that the subgrain size in the softer areas is smaller than in the harder areas.

In order to establish the extent of the microstructural heterogeneity that can be observed in the orientation image maps of the three steels after four passes, several subsets were taken containing smaller sections of the orientation image maps. Subsequently, the dimensions of the (sub-) grains in these selected areas were determined. Three subsets were taken from the hypo-eutectoid steel. The first subset covers the area immediately adjacent to a band of ferrite grains. This subset consists of pearlite grains surrounding the band of ferrite grains. Subset 2 and subset 3 consist of areas that are composed only of pearlite grains. Furthermore, two subsets were taken from the hyper-eutectoid steel, namely subset 1 from the area that consists of "streams" of pearlite that flow around the clusters and subset 2 from the "streams" of pearlite whose movement appears to be restrained by the clusters. Finally, two subsets were taken from the eutectoid steel. These subsets were not made because of the microstructural heterogeneity, but because the orientation image map contained large local concentrations of misindexed data points. The two subsets were chosen such that they contain as few misindexed data points as possible. The results of these measurements are listed in tables 4.6 to 4.8.

The results of the statistical analysis of the selected areas of the hypo-eutectoid steel show a higher percentage of high-angle boundaries and a smaller subgrain size in the pearlite neighbouring the ferrite. It may therefore be concluded that the pearlite in this area has to accommodate the difference in the rate of deformation between the ferrite and the pearlite that is further away from the ferrite and does not share any boundary with the ferrite grains.

A similar observation can be made in the case of the hyper-eutectoid steel: here the pearlite is much softer than the clusters and hence the deformation concentrates in the pearlite. In the vicinity of large second-phase particles or second-phase pseudo-particles -which the cementite clusters really are- the deformation rate is higher than at greater distances away from these (pseudo-) particles. Consequently, the microstructure exhibits pearlite grains that "flow" around the large clusters. Moreover, it can also be observed that other pearlite grains are restrained or even halted in their movement. This behaviour leads to a significantly larger amount of high-angle boundaries among the moving pearlite of subset 1 than among the restrained pearlite of subset 2. On the other hand, the subgrain size is not affected by the heterogeneity.

In the eutectoid steel one can observe an even distribution of the subgrain size and the percentage of high-angle boundaries as was expected. The standard deviation is also smaller than that of the other two steels, meaning the subgrain size distribution is narrower than that of the other two steels.

4.2.4 DISCUSSION

After inspection of the orientation image maps and the data that was derived from them, it was found that the maps frequently cover only a small area. Therefore, their representativeness may be questionable and one should be careful with the interpretation of the quantitative data. Nevertheless, some qualitative and quantitative general conclusions can be drawn from the maps. These are summarised in the following paragraphs.

QUALITATIVE DISCUSSION OF THE MICROSTRUCTURAL EVOLUTION

The comparison of the orientation image maps of the hypo-eutectoid steel after three and four passes does not reveal many changes in a qualitative respect, but from a quantitative point of view a clear increase in the (sub-) grain size and a clear decrease in the percentage of high-angle boundaries are shown. The map of the hypo-eutectoid steel after five passes is omitted from the discussion, because of an error during processing. The sample accidentally rotated in the die and consequently an elongated microstructure was formed with excessively long grains and sub-grains, as can be observed in figure 4.35.

The orientation image maps of the eutectoid steel exhibit clearly different microstructures. Despite the different map sizes that were used, it is evident that the microstructure after four

Table 4.6. Microstructural heterogeneity in the hypo-eutectoid steel after four passes.

	Subset 1	Subset 2	Subset 3
ECD	0.55 ± 0.47	0.76 ± 0.70	0.63 ± 0.45
n	735	280	241
% LAGB	58	64	66
% HAGB	42	36	34

Table 4.7. Microstructural heterogeneity in the eutectoid steel after four passes.

	Entire map	Subset 1	Subset 2
ECD	0.37 ± 0.25	0.42 ± 0.29	0.40 ± 0.26
n	17,016	4,463	7,760
% LAGB	32	38	34
% HAGB	68	62	66

Table 4.8. Microstructural heterogeneity in the hyper-eutectoid steel after four passes.

	Subset 1	Subset 2
ECD	0.15 ± 0.30	0.15 ± 0.37
n	1,712	820
% LAGB	34	41
% HAGB	66	59

passes contains significantly more subgrains and grains than that after three passes. The microstructure of the eutectoid steel after three passes still contains quite a few areas in which a subgrain structure has not formed yet, whereas the establishment of a subgrain structure in this steel is compete after four passes. A further change occurs between four and five passes. The orientation image map after four passes exhibits a lamellar structure, where the interior of the elongated grains exhibits a clear subgrain structure with roughly the same morphological and crystallographic orientation. After five passes, more high-angle boundaries can be seen. Additionally, the edges of the elongated grains have become more serrated, because individual subgrains have begun to rotate towards a more stable final orientation. It can therefore be concluded that once a subgrain structure has been established, the subgrain boundary misorientation continues to increase.

The same qualitative trend as observed in the other two steels can also be observed in the hyper-eutectoid steel. Although the microstructures that are seen in the orientation image maps after three and four passes are qualitatively similar and also display a lamellar structure, the microstructure after five passes is completely different. The microstructure of this condition displays a random morphological and crystallographic orientation. The lamellar structure is not visible anymore, the grains have an irregular shape and the subgrains tend to be more equiaxed than elongated. Quantitatively, it is only possible to draw reliable conclusions from the map after four passes, as was previously explained.

Recently, research on the severe deformation of steel was published by Bowen [7], Reis et al [69]. Their results are in many aspects remarkably similar to the results presented here, hence a comparison is made in the following paragraphs.

Bowen investigated the effects of severe deformation by equal-channel angular pressing on the microstructural evolution of an aluminium-magnesium alloy and an interstitial-free steel. He used the exact same conditions as were used for this investigation. Reis et al investigated the severe deformation behaviour of an interstitial-free steel via accumulative roll-bonding. The processing conditions they used differ considerably from those used in this investigation and that of Bowen. Reis et al deformed an interstitial-free steel by accumulative roll-bonding in a laboratory roll at 480 °C, thereby applying ten consecutive passes during each of which a rolling reduction of 50 % was applied. This leads to an accumulated rolling reduction of 99.9 % or a total strain of $\varepsilon_{eff} = 8.0$. Measurements were conducted on the central region and on the surface region of the stack of sheets.

The results presented in this investigation show that two stages can be distinguished in the evolution of the microstructure in the applied strain range. In the first stage, i.e. at the lower levels of deformation, the number of low-angle boundaries increases rapidly during the first few passes through the formation of a subgrain structure. In the second stage, i.e. at the higher levels of deformation, the majority of the subgrain structure has been formed. Consequently, only a moderate build-up of the number of low-angle boundaries can be seen during further deformation of the steels until after five passes the formation is complete. Simultaneously, the misorientation of the existing low-angle boundaries increases rapidly, such that they become high-angle boundaries. Already after four passes, a substantial fraction of subgrain boundaries have become

high-angled in nature. It must be pointed out that there is no clear limit between the end of the first stage and the beginning of the second stage. The two stages overlap to a certain extent, as was also found by Reis et al [69].

On a larger scale, it can be observed that both the grains and the subgrains in the high-carbon steels become elongated and form a lamellar structure. In this lamellar structure the major axis of the grains and subgrains tends to be oriented towards the deformation direction, i.e. the rolling direction during accumulative roll-bonding and the pressing direction during equal-channel angular pressing. The origin of this lamellar structure comes from the tendency of the new high-angle boundaries to form predominantly parallel to the extrusion direction, while a smaller fraction of the high-angle boundaries is formed in a direction that is perpendicular to the pressing direction. The same behaviour has also been encountered by Bowen [7], Kestens [41] and Reis et al [69], although during the experiments of Reis et al a typical rolling microstructure dominated during the first few passes. Occasionally, the characteristic behaviour of the formation of new high-angle boundaries leads to the formation of subgrains that are completely surrounded by high-angle boundaries. These should therefore be classified as separate grains. However, as was shown by the boundary misorientation distribution graphs (see figure 4.43), the three high-carbon steels are still low-angled in character, despite the rapid increase of the percentage of high-angle boundaries. The new grains are often formed inside the existing elongated grains (see e.g. figure 4.37b). These high-angled subgrains are formed because their original orientation was rather unstable, contrary to the surrounding subgrains, and hence deformation triggered the rapid rotation of these subgrains and the concomittant increase of the boundary misorientation. Moreover, in the section on the qualitative EBSD-analysis (section 4.2.2) it was already mentioned that some orientations are more stable than others. Bowen [7,65] also noticed this kind of behaviour, which in a certain strain range leads to local differences in the rate of grain refinement.

Furthermore, Bowen [7,65] also observed that once a lamellar structure has formed, the grains are several subgrains in width and during further deformation the grain width progressively decreases until it reaches one subgrain in width by the end of stage 3 (ε_{eff} = 6). In this respect, the three high-carbon steels investigated here differ from the interstitial-free steel investigated by Bowen, since even at the highest strains applied (ε_{eff} = 3.33) the grains are roughly ten to twenty subgrains wide. In addition to this, the formation of a lamellar structure in the three high-carbon steels is not yet complete.

QUALITATIVE DISCUSSION OF THE MICROSTRUCTURAL HETEROGENEITY

Recently, a paper was published that dealt with the effects of second-phase particles on the microstructural evolution during equal-channel angular pressing. Apps et al [1] performed research on a model single-phase aluminium-magnesium alloy and a commercial precipitation-hardening aluminium-iron-silicon alloy. They found that "new high-misorientation boundaries are rapidly developed within deformation zones surrounding the second-phase particles, which leads to an acceleration in both the density and misorientation of the new high-angle boundaries formed in a particle-containing alloy, relative to a single-phase material." Apart from this microstructural heterogeneity they observed that these second-phase particles also cause a subdivision of the

grains and are very effective in reducing the average high-angle grain boundary spacing. Their results are in agreement with previous results from Humphreys et al [29] and Hutchinson [33].

The hyper-eutectoid steel behaves similar to the aluminium alloy tested by Apps et al. Like their aluminium alloy, the hyper-eutectoid steel contains large "particles" in the form of the cementite clusters. In the immediate vicinity of these clusters one can observe the formation of very small grains and concomitantly a much higher density of high-angle boundaries than at a distance further away from the clusters. The underlying reason is that the particles cause heterogeneities in the plastic flow, something that is also similar to the flow behaviour around the clusters in the hyper-eutectoid steel. Differences in microstructural behaviour can also be observed. The subgrain dimensions of the hyper-eutectoid steel are not affected by the presence of the clusters, whereas Apps et al found that both the grain size and subgrain size are consider ably smaller in the immediate vicinity of the hard second-phase particles than elsewhere. After comparing these results, it appears that the following requirements need to be met in order for this kind of microstructural behaviour to occur:

(1) A substantial fraction of a second phase needs to be present;
(2) The second-phase (pseudo-) particles need to be much harder than the matrix material;
(3) The second-phase (pseudo-) particle needs to have a certain minimum size in order to be effective.

Given the results presented in this report and in the paper by Apps et al, it may be concluded that the deformation is concentrated in the softer phase. Consequently, substantially more deformation is required to introduce submicrocrystalline grains in materials like these, since the soft phase comprises only a small fraction of the entire material. Moreover, the steels have at present a very inhomogeneous microstructure and the flow is rather localised, which will probably also affect the mechanical properties.

QUANTITATIVE DISCUSSION

The quantitative results of the EBSD-analysis are compared with results from Bowen [7,65], Reis et al [69]. Unfortunately, due to the serious software deficiencies and to the accuracy and reliability issues discussed previously, it is decided to use only the data of the high-carbon steels after a strain of $\varepsilon_{eff} = 2.67$ (four passes) for the comparison. The results are shown in figure 4.44 and table 4.9.

Figure 4.44 reveals striking similarities and differences. The course of the grain refinement during accumulative roll-bonding is remarkably similar to that during equal-channel angular pressing, despite the large differences between these processes. On the other hand, the rate at which both steels evolve is different.

The grain dimensions of the three high-carbon steels are markably different from those of the interstitial-free steel tested by Bowen. Whereas the grain width of the hypo-eutectoid steel is only slightly smaller, the grain widths of the other two high-carbon steels are much smaller than that of the interstitial-free steel. This clearly shows that already after three passes a submicrometer subgrain structure is achieved in these steels. It is also clear evidence that an (almost)

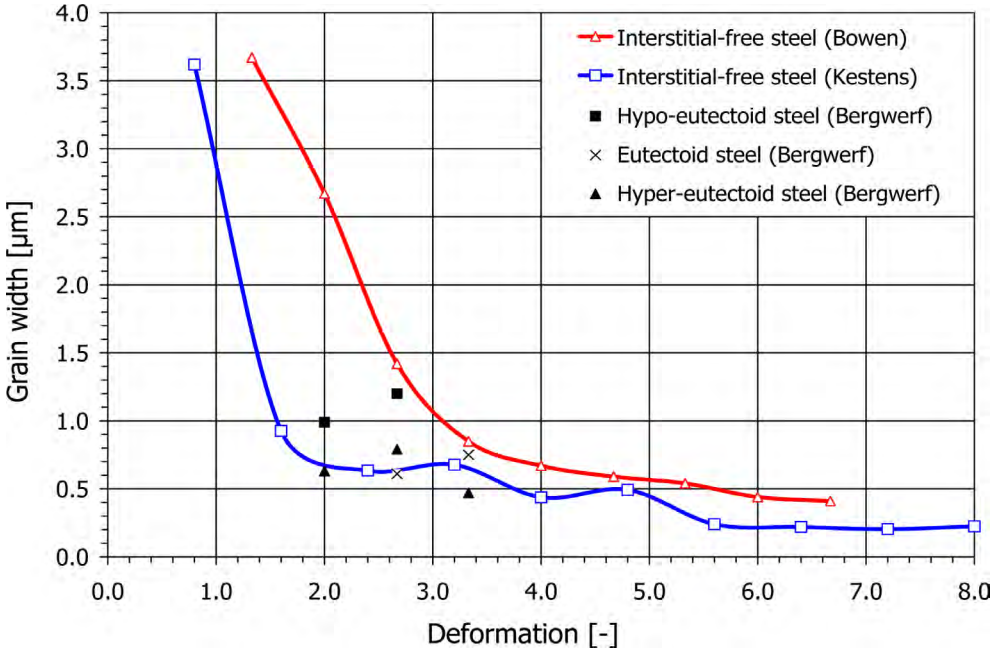

Figure 4.44. Evolution of the grain width as a function of strain for four different types of steel. Data for the interstitial-free steels are courtesy of Bowen [7] and Reis et al [69].

Table 4.9. Grain width, subgrain width and percentage of high-angle boundaries of several steels that have been deformed via equal-channel angular pressing or via accumulative roll-bonding to an effective strain of ε_{eff} = 2.67. All data was obtained from orientation image maps of the mid-section of the sample.

Steel	Grain width (µm)	Subgrain width (µm)	Percentage HAGB's (%)
Interstitial-free (1)	1.30	0.66	32.50
Interstitial-free	0.65 (2)	(3)	31.50 (2)
Hypo-eutectoid	1.20	0.63	43.45
Eutectoid	0.61	0.41	57.60
Hyper-eutectoid	0.79	0.53	60.37

(1) Data courtesy of Bowen [7].
(2) Interpolated from data of Reis et al [69].
(3) Data not available.

eutectoid structure strongly promotes grain refinement and is also more advantageous to grain refinement than a single-phase structure or a structure with finely dispersed small precipitates. More differences occur in the evolution of the high-angle boundaries. Table 4.9 shows that the percentage of high-angle boundaries is again considerably smaller than that of the high-carbon steels. Another difference occurs among the high-carbon steels: the percentage of high-angle boundaries of the eutectoid and the hyper-eutectoid steels are comparable, but is considerably smaller in the hypo-eutectoid steel. The subgrain size of the hypo-eutectoid steel is considerably larger than that of the other two steels. This is in agreement with the findings from the previous section in which was stated that the grains in the hypo-eutectoid steel hardly contain high-angle boundaries. These findings also confirm that the presence of a soft phase has a detrimental effect on the rate of microstructural evolution, since the other two high-carbon steels exhibit sub-

stantially smaller (sub-) grains. It must be concluded that the rate of microstructural evolution and grain refinement is considerably higher in the high-carbon steels.

The results of Reis et al are, however, more complex. In this case, the rate of grain refinement is much higher than that of all other steels. This is due to the strain inhomogeneity of the accumulative roll-bonding process that is particularly strong during the first few passes. The shear deformation condition is superimposed on the plane strain deformation condition, causing a larger effective deformation, hence smaller grain dimensions, in the centre of the stack of sheets. Reis et al found that the shear deformation is the dominant deformation mode up to a strain of about $\varepsilon_{eff} = 4.5$, whereas at larger strains a plane strain condition is dominant.

CONCLUDING REMARKS

Overlooking the results presented here and comparing them with those from Bowen, Reis et al striking similarities are found, despite the obvious differences of deformation mode and carbon content. Apparantly, neither the deformation mode nor the material seem to be of great importance to the final microstructure. In fact, only the rate of microstructure chang differs.
In addition, after gathering and reviewing the evidence that (1) the formation of a lamellar structure is incomplete, (2) the grains are many subgrains wide and (3) local heterogeneities in the subgrain dimensions exist, it must be concluded that all three high-carbon steels are in the final phase of stage 2, as has been described in section 2.2. Bowen indicated that stage 3 is in the strain range from $\varepsilon_{eff} = 4 - 6$, which leads to the conclusion that the high-carbon steels behave according to the mechanism described by him. Again, only the rate of grain refinement is different: the subgrains in the high-carbon steels are much smaller.

4.3 MECHANICAL PROPERTIES

Tensile testing was carried out at the Swinden Technology Centre of Corus UK in Rotherham and microhardness testing was carried out at the Manchester Materials Science Centre. Two tensile test samples and one microhardness sample were produced from each ECAP-processed sample. The tensile test samples were tested to produce the yield strength, the ultimate tensile strength and the fracture elongation for all three steels. The average of two tests was taken for each data point in the graphs. The data from these experiments are listed in tables C1 and C2 of appendix C, and plotted in figures 4.45 to 4.48.

MICROHARDNESS

The results of these measurements are shown in figure 4.45. The graphs of the three steels are characterised by an initial sharp increase after the first pass and an absence of a significant change at greater levels of deformation. The microhardness of the hypo-eutectoid steel increases from 213 HV in the initial condition to just under 300 HV after five passes. The microhardness

of the other two steels is as good as the same in the initial conditions; 254 HV and 250 HV for the eutectoid and the hyper-eutectoid steel, respectively. After five passes, the difference in microhardness between these two steels has become significant with 323 HV for the eutectoid steel and 344 HV for the hyper-eutectoid steel. The difference in the microhardness can be attributed to the effect of the composition. The hyper-eutectoid steel is the hardest of the three steels, because it contains the largest fraction of the hard cementite phase. The opposite is true for the hypo-eutectoid steel, which has the largest fraction of the soft ferrite phase. Apparently, the presence of the soft ferrite has a larger and negative effect on the microhardness than the presence of the hard grain boundary cementite, which causes positive effect on the hardness.

TENSILE TESTING

The yield strength, the ultimate tensile strength and the elongation at fracture are plotted as a function of the strain in figures 4.46 to 4.48, respectively. The yield strength of the three steels is initially about σ_{YS} = 400 MPa. Strangely, the yield strength of the eutectoid steel (418 MPa) exceeds that of the hyper-eutectoid steel (385 MPa) in the initial condition, but not in any of the deformed conditions. The cause of this oddity remains yet unknown. After a single pass, the yield strength quickly rises to a value of about 700 MPa for the hypo-eutectoid steel and about 800 MPa for the other two steels with the increase of the hyper-eutectoid steel being slightly stronger than that of the other two steels. The effect of the composition immediately becomes evident, since the yield strength of the hypo-eutectoid steel is considerably lower than that of the other two steels, which are more closely spaced. At higher levels of deformation, the yield strength of the three steels progressively increases, although at a much lower rate than after the first pass. The difference in strength between the three steels is more or less conserved during subsequent passes. Maximum yield strengths of 884 MPa, 982 MPa and 1,066 MPa are attained after four passes for the hypo-eutectoid, the eutectoid and the hyper-eutectoid steel, respectively.

The initial conditions of the ultimate tensile strength of the three steels resemble those of the microhardness and the yield strength in that the ultimate tensile strength of the hypo-eutectoid steel is the lowest (743 MPa), while the ultimate tensile strength of the eutectoid steel (878 MPa) exceeds that of the hyper-eutectoid steel (860 MPa), although during subsequent deformation the latter is higher than the former. The course of the ultimate tensile strength of the three steels as a function of the strain is characterised by a pronounced increase during the first pass. During subsequent passes the ultimate tensile strength increases only very little and after four passes it amounts 974 MPa, 1,036 MPa and 1,112 MPa for the hypo-eutectoid, the eutectoid and the hyper-eutectoid steel, respectively. The increase between the initial condition and the last pass is not as much as with the yield strength, but values of about 1 GPa or more are still very impressive! Similar to the microhardness, the ultimate tensile strength of the hypo-eutectoid steel is much lower than that of the eutectoid and the hyper-eutectoid steels. The latter ones have approximately the same values until two passes, while the eutectoid steel appears to be somewhat softer than the hyper-eutectoid steel between the second and the fourth pass.

The behaviour of the fracture elongation differs from one steel to the other. The fracture elongation of the hypo-eutectoid steel decreases strongly from the initial 18 % to 10 %

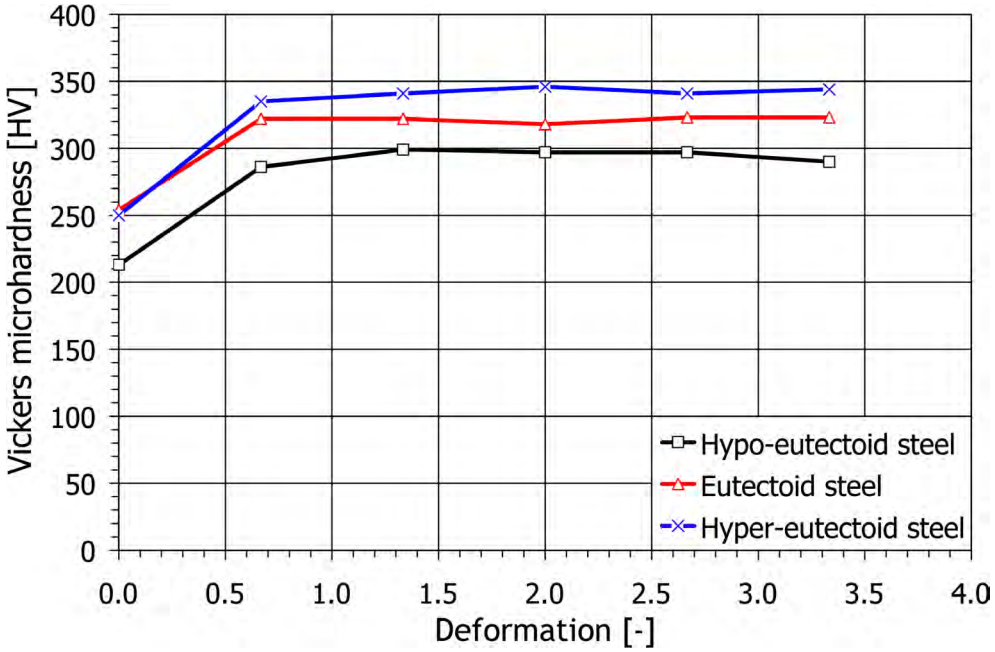

Figure 4.45. The Vickers microhardness (1 kg load) as a function of the accumulative deformation by equal-channel angular pressing for the three high-carbon steels.

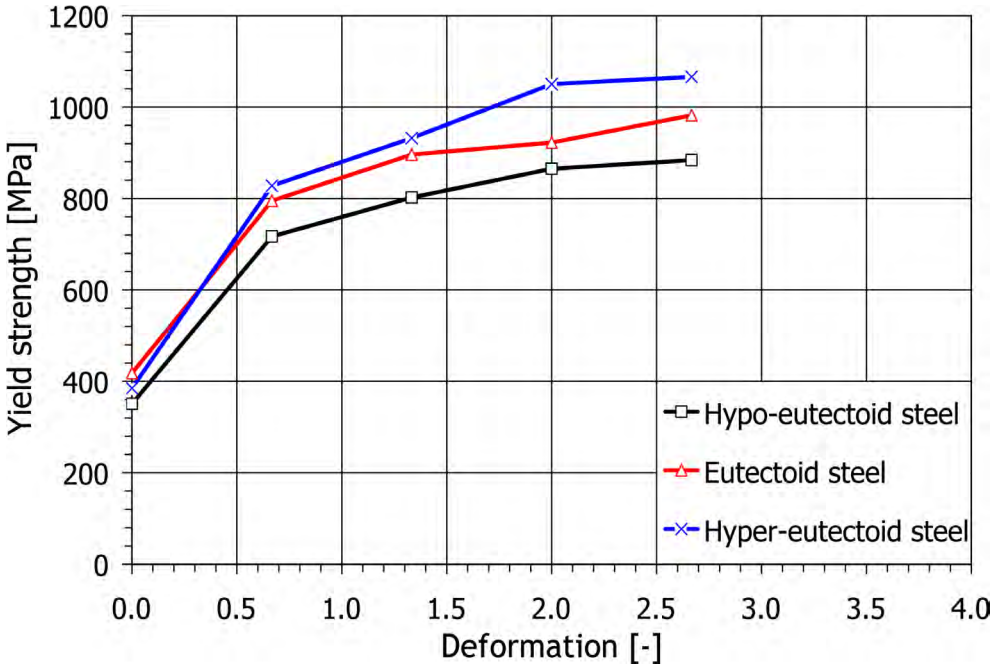

Figure 4.46. The yield strength as a function of the accumulative deformation by equal-channel angular pressing for the three high-carbon steels.

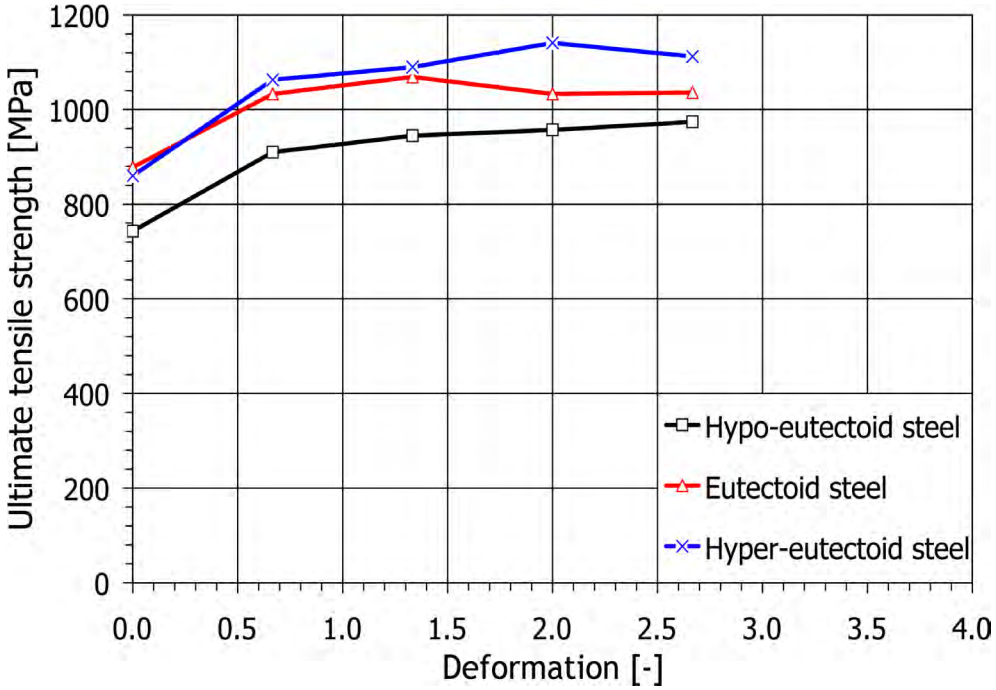

Figure 4.47. The ultimate tensile strength as a function of the accumulative deformation by equal-channel angular pressing for the three high-carbon steels.

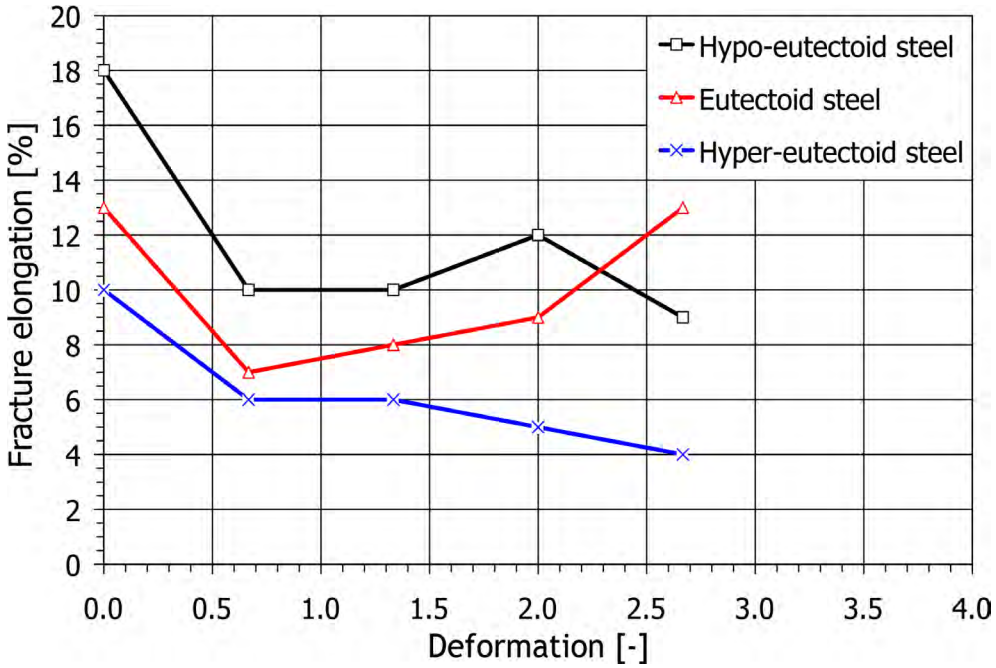

Figure 4.48. The fracture elongation as a function of the accumulative deformation by equal-channel angular pressing for the three high-carbon steels.

after one pass. It then remains roughly constant, but shows a more pronounced drop to 9 % during the fifth pass. The fracture elongation of the eutectoid steel decreases equally strong from 13 % in the initial condition to 7 % after one pass. It then increases slightly up to the fourth pass and sharply to the initial value of 13 % after the fifth pass. The hyper-eutectoid steel exhibits the same behaviour as that of the hypo-eutectoid steel. It initially amounts 10 %, but during subsequent passes it first remains constant at, then decreases gradually to 4 %.

DISCUSSION

The initial values of the strength and the hardness of the hyper-eutectoid steel are odd. Normally they should be the highest of the three steels, but in this case the initial values fall in between those of the hypo-eutectoid and the eutectoid steels. Since this oddity occurred not only in the yield strength and the ultimate tensile strength, but also in the Vickers microhardness, a mistake during tensile testing must be ruled out as a possible cause. Instead, the cause must be found in the microstructure of this steel. Although the exact cause cannot be determined, it could be that local differences in the microstructure of the billet from which the extrusion samples were taken, may have caused this effect.

The increase in the strength and the hardness is caused by (1) strain hardening, i.e. the built-up of a dense dislocation network and subsequent entanglement of dislocations, and (2) grain boundary strengthening, i.e. the formation of a barrier in the movement of the dislocations. The former plays a major role during the first extrusion pass between $\varepsilon = 0$ and $\varepsilon = 0.67$. At higher strains, the dislocation density increases only moderately until it reaches a maximum. At the same time, a dislocation cell structure is being established that evolves into a subgrain structure. During subsequent deformation, the misorientation between the lattices of adjacent subgrains tends to increase further, thereby forming a barrier in the movement of dislocations that is increasingly harder to overcome. Consequently, a simultaneous effect of both strain hardening and boundary strengthening can be observed during subsequent extrusion, i.e. at deformation levels higher than $\varepsilon = 0.67$. However, it is impossible to distinguish two separate intervals for the strain hardening that is dying out and the boundary strengthening that is becoming increasingly important. The increase in the fracture elongation of the eutectoid steel after the third pass may be an indication of the onset of grain boundary strengthening, though this remains uncertain. Further research to the mechanical properties of the steels at higher levels of deformation will need to be performed.

Around the turn of the millennium D.-H. Shin and his co-workers published a number of papers [79–85] dealing with the effects of equal-channel angular pressing on the microstructural development and the mechanical properties of a commercial low-carbon steel with the composition 0.15 wt.%C – 1.1 wt.%Mn – 0.25 wt.%Si. The rig they used had a die with round channels of 18 mm in diameter. The two channels intersected at an angle of $\varphi = 90$ °, while the corner was rounded off with an angle of curvature of $\psi = 20$ °. These parameters yield an effective strain of $\varepsilon_{eff} \approx 1$ per pass. The pressing was carried out at a temperature of either 200 °C (473 K) [79] or 350 °C (623 K) [80-85], while the sample was rotated 180 ° in between the passes, a method that is commonly known as route C.

D.-H. Shin and co-workers obtained remarkable results with their experiments. Figure 4.49 shows two graphs from one of their papers [80]; graph (a) shows the Vickers microhardness for the pearlite and the ferrite phase separately as a function of the deformation, while graph (b) shows the yield strength, the ultimate tensile strength and the fracture elongation as a function of the deformation. The yield strength of their low-carbon steel triples to 900 MPa after four passes ($\varepsilon_{eff} \approx 4.2$). The value of ultimate tensile strength, increases to about 900 MPa after four passes, almost double of the original value, while the value of fracture elongation is reduced to approximately 10 %, which is much less than the original value of 26 %. Notice that the curves of the yield strength and the ultimate tensile strength converge with increasing deformation. This is evidence of a lack of strain hardening at higher levels of deformation. The lack of strain hardening is commonly encountered in severely deformed materials, also in the three high-carbon steels that are under investigation in this report.

Although they used the same device and a very similar material, their results do not fully agree with those presented in this report. The microhardness of their low-carbon steel increases faster during the first pass than that of the three high-carbon steels, and during subsequent passes the microhardness of the low-carbon steel continuously increases, though at a lower rate than during the first pass, whereas that of the high-carbon steels remains constant. Furthermore, the behaviour of the yield strength of the low-carbon steel is in agreement with that of the high-carbon steels. The behaviour of the ultimate tensile strength of the low-carbon steel, on the other hand, differs from that of the high-carbon steel and resembles that of the course of the microhardness. The agreements and differences can be attributed to the effect of the composition on the dislocation behaviour. The low-carbon steel contains a considerably larger fraction of ferrite than the high-carbon steels. Consequently, the generation of new dislocation and their subsequent movement throughout the crystal lattice is different. The larger fraction of ferrite allows a considerably larger amount of dislocations to be formed, which are also less hindered by obstacles, such as second phases and dislocation entanglements. Due to this, the mechanical properties of the low-carbon steel do not level off that quickly, but continue to increase gradually.

4.4 GENERAL DISCUSSION

COMPARISON BETWEEN THE SEM AND EBSD-TECHNIQUES

The previous sections suggest a possible correlation between the rate of fragmentation of the cementite lamellae and the rate of formation of a subgrain structure in the ferrite. Fragmented cementite lamellae were identified as possible sites for the formation of subgrain structures. The identification was done using either secondary electron images or orientation image maps. However, simultaneous measurements using these two techniques were not conducted.

The main advantage of secondary electron imaging in a scanning electron microscope is to quantify the dimensions of high-contrast objects (grains, second-phase particles, etc.), though this technique is less suitable to determine the subgrain size and the dimensions of tiny second-

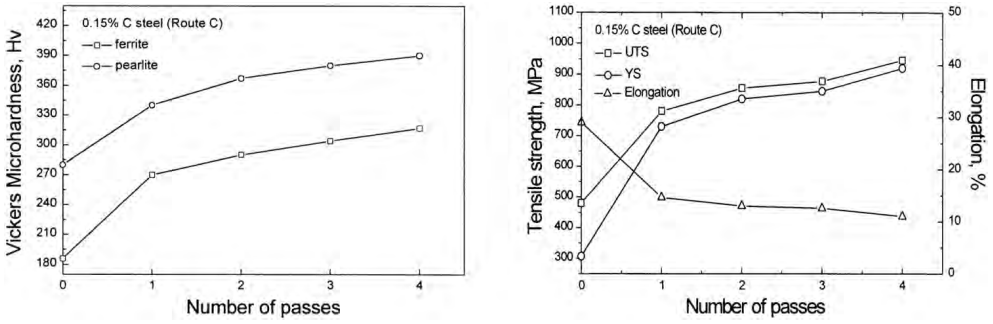

Figure 4.49. (a) The Vickers microhardness (1 kg load) and (b) the yield strength, the ultimate tensile strength and the fracture elongation as a function of the accumulative deformation by equal-channel angular pressing for a low-carbon steel. [80]

phase particles. Subgrains are occasionally visible, but this is an exception rather than a rule. As was found during the present investigation too, the accuracy of the measurement is highly dependent on the contrast and rapidly decreases if the contrast is at a medium or low level. Quantitative microstructural analysis may be very difficult or even impossible when examining samples of a severely deformed material. Additional treatments, such as etching with an appropriate etchant or occasionally electropolishing, are often required to obtain a sufficiently high contrast. The etchant used in this investigation yielded a high contrast for the SEM-analysis of the high-carbon steels.

It is impossible to determine the crystallographic orientation using secondary electron imaging. Orientation image microscopy via electron backscattered diffraction analysis was used to overcome this problem. The advantage of this technique is that it is excellently suitable to swiftly determine the dimensions of large volumes of (sub-) grain structures and for the determination of the orientation of individual crystals. Even the orientation of spots within a crystal can be determined so that orientation gradients can be recorded and can be mapped. This also enables the determination of the orientation relationship between two points in adjacent crystals. Contrary to SEM, the EBSD is less or even not suitable to quantify the dimensions of second-phase particles. These are difficult to detect or easily "overlooked" when their dimensions are small compared to the step size. Further information on the difficulties of this technique can be found in section 4.2.1. In this investigation the EBSD-technique was adopted to map the microstructure from spot to spot and to quantify the (sub-) grain dimensions. Although in many cases second-phases particles could be seen in the orientation image maps, the accuracy and resolution was too low to use this information for interpretation.

The best results can be obtained when creating orientation image maps from the secondary electron images of the same location or vice versa. Unfortunately, it was found to be impossible to simultaneously measure both the rate of fragmentation and the rate of subgrain formation. This was primarily due to different sample preparation methods. Another cause was the heavy use of the Philips XL30 scanning electron microscope that hardly allowed for prolonged sessions. Careful electropolishing was essential, since orientation image mapping can only be carried out accurately on samples with strain-free surfaces. If electropolished samples were analysed via secondary electron imaging this would have yielded blurry low-contrast images that

were not suitable for quantitative microstructural analysis. Alternatively, chemical etching was required for SEM-analysis. This, however, would have yielded very indented surfaces that were not strain-free. Consequently, orientation image maps from such samples would have exhibited strong shadow formation and a low indexation.

GENERAL EVOLUTION OF THE MICROSTRUCTURES

Observation of the data from the secondary electron images and the orientation image maps revealed that the microstructures in the three high-carbon steels evolve quite differently. Both the pearlite and the subgrains evolve in a different manner in the presence of ferrite or grain boundary cementite. The following paragraphs describe how this evolution takes place during successive deformation.

After the first pass, the lamellae start to deform and dislocation cell walls start to appear. Local variations in the deformation lead to the formation of complex microstructures and in the hyper-eutectoid steel also to the formation of clusters of deformed cementite lamellae. No difference was observed in the deformation behaviour of the pearlite in the three steels.

After the second pass, more complex deformation microstructures are observed. All three steels contain small regions in which the cementite lamellae have broken up into smaller segments, although the lamellar nature of the microstructure is still dominant. However, it is obvious from the secondary electron images that the fragmentation progressed at a higher rate in the hypo-eutectoid steel and the eutectoid steel than in the hyper-eutectoid steel. A plausible explanation for this may be found in the lamellar width and distance. As table 4.1 shows, the lamellar width and distance of the hypo-eutectoid and the eutectoid steels are the same, while those of the hyper-eutectoid steel are much bigger. Hence, the lamellae in the hyper-eutectoid steel are stronger and break less easily. Observation of the orientation image maps revealed that the formation of a subgrain structure has clearly progressed between the first and the second pass.

Comparing the microstructures of the three steels taken after the second and the third pass, it is immediately noticed that the microstructure of the hyper-eutectoid steel has clearly undergone a substantial change, while a smaller and less obvious change can be observed in the microstructures of the other two steels. The microstructure of the hyper-eutectoid steel after two passes is predominantly lamellar with long and bent cementite lamellae. Contrarily, the microstructure of this steel after three passes reveals that the cementite lamellae are mostly broken into shorter fragments. Yet, they are clearly not fully fragmented, i.e. the area and perimeter of the cementite lamellae are still decreasing with increasing deformation, and are still longer in the hyper-eutectoid steel than in the other two steels. The microstructure of the other two steels after the second and the third pass reveal a microstructure that consists of areas with long and bent lamellae and areas with fully fragmented lamellae. The latter areas are found chiefly in the vicinity of grain boundaries, where strain accommodation leads to higher localised deformation.

After four passes, the microstructure of the eutectoid steel is almost fully fragmented. On the other hand, there are still plenty of regions in the hypo-eutectoid and the hyper-eutectoid steels to be observed in which the lamellar nature is still dominant, despite a clear decrease in the fraction of lamellar cementite between the third and the fourth pass. The hypo-eutectoid steel

seems to contain the largest fraction of lamellae, while the fragmentation seems to have progressed at a higher rate in the other two steels. In addition to these findings, it was found that the fraction of high-angle boundaries of the hypo-eutectoid steel is smaller than that of the other two steels. This is caused by the less advanced state of fragmentation and the presence of large subgrains in the soft ferrite grains. Additionally, the formation of ribbon-shaped grains can be observed in both the hypo-eutectoid and the hyper-eutectoid steels. In the hypo-eutectoid steel the ribbons consist of ferrite grains, whereas in the hyper-eutectoid steel the ribbons are made of pearlite grains. Clearly, the softer phase forms ribbon-shaped grains.

Given the shortage of quantitative data from the secondary electron images and the orientation image maps we can only speculate why it appears as if the hypo-eutectoid steel after five passes is in the most advanced state of fragmentation, contrary to the previous passes. The fragmentation in this steel is complete, whereas that of the other two steels is not complete yet and some tiny lamellar regions can be observed. An explanation could be that the accidental rotation of the billet during the fifth pass caused the remaining lamellae to break. As the samples of the eutectoid and the hyper-eutectoid steels did not rotate, there is still a very small fraction of lamellae left after five passes. An important implication of this explanation would be that route A is not the most effective route for breaking lamellar eutectoid microstructures.

The nature of the fragments can be different, though. While the findings presented here show that the fragmented lamellae are big enough to act as sources for the generation of dislocations, previous findings from Bowen [7,8], Kestens [41] and Reis et al [69] contradict the present findings. They conducted research on micro-alloyed interstitial-free steel and found that the carbides in these steels are much too small to act as dislocation sources, although the carbides do affect the movement of dislocations.

Around the turn of the millennium D.-H. Shin and co-workers [79-85] conducted equal-channel angular pressing experiments on a low-carbon steel containing 0.15 wt.% C. They conclude from transmission electron micrographs that a submicrocrystalline grain structure has formed, although the exact method is not described and the representativeness of the microstructures shown (see figure 4.50) is disputable. Nevertheless, their conclusion is supported by the findings of this investigation and by previous research by Bowen [7,8]. The three high-carbon steels under investigation here contain 47 - 85 % high-angle boundaries after a strain of ε_{eff} = 3.33, whereas the interstitial-free steel tested by Bowen contains about 50 % high-angle boundaries after a strain of ε_{eff} = 4. Although accurate numbers cannot be given, it is estimated from the bright-field images that the percentage of high-angle boundaries in the low-carbon steel is comparable. The results for the grain size are comparable too. The grain size of the high-carbon steels is in the range of 0.6 – 1.2 µm. These values are larger than the 0.3 µm found by Shin et al, but the level of deformation is lower than theirs. At the same level of deformation, the grain size of the interstitialfree steel amounts about 0.6 µm. This too is larger than the grain sizes found by Shin et al, but the difference is due to the extremely low carbon content. Furthermore, the diffraction pattern of the low-carbon steel contains discontinuous rings of diffuse maxima in the intensity and the fraction of high-angle boundaries in the bright-field image of figure 4.50b does not seem too high at all. Hence, it is likely that the process of grain refinement has not reached completion yet

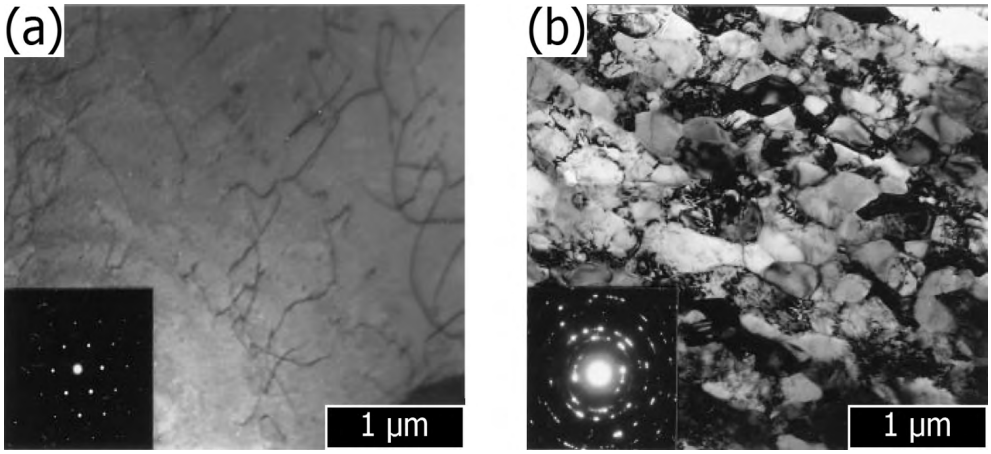

Figure 4.50. Bright-field transmission electron micrographs and their corresponding selected area diffraction patterns of a low-carbon steel (a) in the as-received condition and (b) after four passes ($\varepsilon_{eff} \approx 4.2$) by equal-channel angular pressing. [80]

in the low-carbon steel. Again, the same was found in this investigation and in that of Bowen [7] at comparable levels of deformation.

MICROSTRUCTURAL HETEROGENEITY AND DEFORMATION LOCALISATION

The interaction between the heterogeneous deformation and the heterogeneous microstructure causes strain accommodation to take place and the already complex microstructure to become even more complex. The extent and manner in which the microstructure responds to the localised strain often differs widely from spot to spot. Several locations for the occurrence of strain localisation were identified, namely:

(1) The shear bands and other deformation features in the pearlite;
(2) The interface between neighbouring pearlite colonies, and;
(3) Additional effects occur in the hypo-eutectoid and the hyper-eutectoid steels due to the presence of the ferrite and the grain boundary cementite phase.

The effects of the additional interaction between these phases include for instance the accelerated fragmentation of the cementite lamellae in the pearlite in the vicinity of ferrite and grain boundary cementite grains. The opposite effect also occurs: decelerated fragmentation is frequently found in the centre of pearlite grains and in the immediate vicinity of some cementite clusters. Another, less significant effect that occurs due to the heterogeneous deformation is that the angle under which the pearlite intersects with the other phase (cementite, ferrite or pearlite) affects the rate of fragmentation of the cementite lamellae. Relatively small angles of intersection are likely to lead to bending of the pearlite, whereas relatively large angles will lead to fragmentation. The heterogeneous deformation behaviour affects not only the cementite lamellae in the pearlite, but also the ferrite. The subgrains in the ferrite phase of the hypo-eutectoid steel are substantially larger than those in the ferrite lamellae of the pearlite. Consequently, disproportionally large average subgrain dimensions may be found in the hypo-eutectoid steel.

Not only the rate of fragmentation is affected by strain localisation in the microstructure, the formation of a subgrain structure is affected too. For instance strain localisation in the hypo-eutectoid steel tends to occur in the soft ferrite phase. A subgrain structure is readily formed in the ferrite phase because of this, and already after two passes the hypo-eutectoid steel contains a substantial density subgrains inside the ferrite phase. Additionally, the results revealed that after the establishment of a subgrain structure, the boundary misorientation quickly increases. These findings lead to the conclusion that strain localisation promotes the formation of a subgrain structure. In all three steels, it was found that the subgrain size is limited by the spacing between the intact or fragmented lamellae in the pearlite. And once formed, the subgrains do not grow bigger than this spacing. Also, the subgrain size is much larger in the ferrite phase in the hypo-eutectoid steel. Hence, the cementite lamellae are very effective in controlling the subgrain dimensions. The subgrain dimensions are, however, not affected by the strain localisation. Another characteristic of the subgrains in the hyper-eutectoid steel is that their dimensions are not smaller in the vicinity of cementite clusters or further away from these clusters. Similarly, subgrains do not become smaller in strongly deformed pearlite or in highly fragmented regions. In all regions undergoing a higher local deformation the subgrain boundary misorientation is higher than in other, less deformed regions in the microstructure. The important conclusions from these findings are that the interlamellar spacing of the pearlite is the main factor controlling the subgrain size and that the local rate of deformation is the main factor controlling the misorientation between the (sub-) grains.

LINKING THE MICROSTRUCTURES TO THE MECHANICAL PROPERTIES

Mechanical testing revealed that the main change occurs during the first pass, whereas no (substantial) change occurs during subsequent passes. The course of the microstructural change as a function of the deformation is different, however. In this case, the largest change occurs not during the first pass, but during the second or the third pass, depending on the steel. Like the mechanical behaviour, a gradual change in the microstructures can be observed during subsequent passes.

The evolution of the yield strength, the ultimate tensile strength and the microhardness as a function of accumulative deformation resembles that of a normal stress-strain curve in which the behaviour can be explained by the ongoing competition between dislocation generation (work-hardening) and dislocation annihilation (recovery) in the ferrite (both in the ferrite grains and in the pearlite). The strong increase after the first pass that is displayed by all three steels is likely due to the very high dislocation density that is introduced. Further deformation will cause the dislocation density to increase only slowly until a maximum is reached. Simultaneously, the dynamic recovery will increase and the resultant effect will be a much lower increase of the yield strength, the ultimate tensile strength and the microhardness. It can be expected that the fragmentation of the cementite lamellae also has a increasing effect to the yield strength, the ultimate tensile strength and the microhardness, though this effect cannot be determined from the current data.

The graphs of the elongation at fracture of the three high-carbon steels exhibit trends that are seemingly inconsistent with the other mechanical and microstructural data. These differences are possibly caused by different necking behaviour. A possible mechanism for the fracture behaviour of the three high-carbon steel will be proposed here. Firstly, the crack initiation and crack propagation during necking are the major factors controlling the elongation at fracture. Cracks initiate from voids in either the weakest phase or on points of stress concentration.

The fact that the hypo-eutectoid steel has the largest fraction of the ductile ferrite phase can explain why this material exhibits the largest elongation at fracture. Substantially less cracks initiate in this steel than in the eutectoid and the hyper-eutectoid steels, because the ferrite grains are able to carry on more plastic deformation without cracking. Contrarily, cementite in the hyper-eutectoid steel consists of thick and hence stronger lamellae in the pearlite or at the grain boundaries. These are preferred sites for the formation of cracks, since their ability to deform plastically is much smaller than the ferrite phase. That is why the hyper-eutectoid steel has the lowest initial elongation at fracture. During subsequent deformation, shear bands are formed in all three steels. These shear bands and other deformation features are relatively easy paths for crack propagation. Consequently, a decrease in the elongation at fracture can be observed with increasing plastic deformation. In the hypo-eutectoid steel, deformation concentrates in the ferrite phase, causing it to undergo extensive work-hardening, thereby losing most of its initial benefit of resisting crack formation. The largest decrease in elongation at fracture can therefore be observed in this steel after one pass.

Subsequent deformation causes existing cracks to grow and new cracks to form. Growing cracks are often hindered by the cementite in both the pearlite and at the grain boundaries. The complex microstructures found in the pearlite have a dual effect, both a beneficial and a detrimental one. On the one hand, they increase the rate of crack propagation, because of the presence of a large density of shear bands that facilitate growing cracks. On the other hand, they decrease the rate of crack propagation, because the cementite lamellae, both intact and broken, are serious obstacles to overcome. As the deformation progresses, not only do the lamellae break up into increasingly smaller segments, but the edges of the newly formed segments tend to round off in the hypo-eutectoid and the eutectoid steels too. However, microstructural analysis has shown that the fragmented cementite lamellae and the cementite clusters in the hyper-eutectoid steel frequently have irregular and sharp edges, which act as stress concentration points. Hence, the crack propagation will proceed at a higher rate in this steel and a gradually decreasing elongation at fracture can be observed. In the hyper-eutectoid steel, the pearlite is the weaker and softer phase. Consequently, the microstructure of the hyper-eutectoid steel is the most complex of the three high-carbon steels with numerous shear deformation features. This explains why the smallest elongation at fracture is found in the hyper-eutectoid steel. The eutectoid steel lacks the weak ferrite grains and its fragmented cementite lamellae tend to round-off. A low rate of crack propagation can therefore be expected in this steel, and due to this, a steady increase of the elongation at fracture at higher levels of deformation can be observed.

With the lack of accurate data, these explanations remain speculative. Additional fracture-mechanical research is needed to determine the exact nature of the mechanism of necking and fracture in these high-carbon steels.

Furthermore, it was remarkable to find that neither the fragmentation of the cementite lamellae in all three steels nor the evolution of the cementite clusters in the hyper-eutectoid steel cause the ultimate tensile strength and the microhardness to rise after one extrusion pass ($\varepsilon_{eff} \geq 0.67$). The yield strength, the ultimate tensile strength and the microhardness apparently do not depend significantly on the fragmentation behaviour of the cementite lamellae, though they depend on the work-hardening behaviour. Contrary to these properties, the elongation at fracture depends more significantly on the fragmentation behaviour.

CONCLUDING REMARKS

After comparing the data, it was concluded that the most important parameters in the process of grain refinement of high-carbon steels with a lamellar eutectoid microstructure are the interlamellar distance of the pearlite and the local rate of deformation. The deformation microstructures that are formed in these materials contain subgrains that form between the cementite lamellae. During subsequent deformation the subgrains do not grow through intact or broken cementite lamellae. The heterogeneous deformation only causes the subgrain boundary misorientation to increase, while the subgrain volume remains the same.

It was unexpected to find that the fragmentation of the cementite lamellae has a much smaller effect on the microstructural development than the interlamellar distance of the lamellae. The fragmentation of the cementite lamellae appeared to have a dual effect on the mechanical properties, since the fragmentation appears to have a smaller effect on the yield strength, the ultimate tensile strength and the microhardness than on the elongation at fracture.

Furthermore, there are indications that applying a constant strain path, i.e. using route A, during equal-channel angular pressing of lamellar eutectoid microstructures is not the most effective for the fragmentation of the lamellae.

CHAPTER 5
CONCLUSIONS

(1) A multi-phase lamellar eutectoid microstructure substantially accelerates the development and subsequent evolution of the microstructure compared to a (pseudo-) single-phase microstructure.

(2) The presence of a substantial fraction of coarse second-phase pseudo-particles that are harder than the matrix and do not dissolve at elevated processing temperatures increases both the rate of evolution of the microstructure and the mechanical properties (disregarding fracture-mechanical properties). The opposite is also true: a substantial fraction of a soft phase decreases the rate of evolution of the microstructure and causes inferior mechanical properties as compared to a hard phase.

(3) The macroscopic mode of deformation and the crystal structure have little influence on the evolution of the grain and subgrain dimensions during severe deformation of materials with a cubic crystal structure and a medium to high stacking-fault energy, other than the rate of evolution.

(4) The evolution of the grain and subgrain dimensions of the three high-carbon steels is in agreement with the mechanism of grain refinement by severe deformation proposed by Bowen [7,8].

(5) After five passes by equal-channel angular pressing, equivalent to an effective deformation of $\varepsilon_{eff} \approx 3.33$, the three high-carbon steels are in the final phase of stage 2 (as defined by Bowen [7,8]), which comprises the formation of a microstructure consisting of large and elongated grains with subgrains whose boundary misorientation progressively increases with increasing deformation.

(6) The final submicrocrystalline grain size is determined chiefly by the interlamellar distance of the cementite lamellae.

(7) The boundary misorientation is determined only by the rate of plastic deformation on a microscopic scale.

CHAPTER 6

RECOMMENDATIONS

(1) Due to the persistent trouble that I experienced with the die of the equal-channel angular press I recommend the following modifications to the construction of the die:

   (a) The use of a die material that can resist the high pressures and the abrasion from the processing of hard steels, such as a die made from a hard type of tool steel that is fitted with a surface coating.

   (b) Improved construction of the position of the thermocouples in the die in order to be able to more accurately measure the temperature in the immediate vicinity of the die channel. An improve of the temperature control system would also be beneficial.

   (c) Improved design of the die, which prevents the die halves to open during pressing and yet maintains the ease of cleaning of the die.

   (d) The use of a smaller cross section of the die channels. The main advantage is that this will substantially reduce the pressing load, although the main disadvantage is that there is an increased chance of buckling of the ram.

(2) It is shown in this thesis that the final submicrocrystalline grain size depends on the inter-lamellar distance of the cementite lamellae. It would therefore be recommendable to investigate the effect of the interlamellar distance on the rate of formation of subgrain structures and on the submicrocrystalline grains that eventually are formed from the subgrains.

(3) It was found that the accidental rotation of the billet during pressing led to accelerated fragmentation of the cementite lamellae in the pearlite of the hypo-eutectoid steel. This indicates that the application of route A, involving a constant strain-path, for equal-channel angular pressing of lamellar eutectoid microstructures may not be the most efficient strain path for the breaking down of a lamellar microstructure. Hence, it would be recommendable to investigate the effects of the strain path on the rate of fragmentation of lamellar eutectoid microstructures, thus which route is most efficient in generating a submicrocrystalline structure with the largest area of high-angle boundaries?

(4) Since it was found that the local rate of deformation enhances the boundary misorientation and is especially high in the vicinity of grain boundaries, it would be beneficial to use a steel with a small initial grain size. A second benefit would be the small interlamellar distance.

(5) Two issues that have not received any attention in this thesis, but are known to be important from literature, are the absence of an increase of the dislocation density once a subgrain structure has formed, the lack of sufficient strain hardening that is the consequence of this, and the absence of a substantial refinement of the subgrains once they are formed.

REFERENCES

[1] P. J. Apps, J. R. Bowen, P. B. Prangnell, *The effect of coarse second-phase particles on the rate of grain refinement during severe deformation processing*, Acta Materialia, vol. 51, pp. 2811 - 2822, 2003;

[2] *ASM Handbook, Volume 1: Properties and Selection: Irons, Steels and High-Performance Alloys*, 5th printing, ASM International, Materials Park, Ohio, USA, 1997;

[3] S. C. Baik, Y. Estrin, H. S. Kim, H.-T. Jeong, R. J. Hellmig, *Calculation of deformation behavior and texture evolution during equal-channel angular pressing of IF steel using dislocation based modeling of strain hardening*, Materials Science Forum, vols. 408-412, pp. 697-702, 2002;

[4] B. Bay, N. Hansen, D. A. Hughes, D. Kuhlmann-Wilsdorf, *Overview no. 96: Evolution of fcc deformation structures in polyslip*, Acta Metallurgica et Materialia, vol. 40, no. 2, pp. 205 - 219, 1992;

[5] P. B. Berbon, M. Furukawa, Z. Horita, M. Nemoto, T. G. Langdon, *Influence of Pressing Speed on Microstructural Development in Equal-Channel Angular Pressing*, Metallurgical and Materials Transactions A, vol. 30A, pp. 1989-1997, 1999;

[6] R. Bergwerf, *Ultrafine-grained ferritic steels: A literature review to their formation, production and properties*, Delft University of Technology, Delft, The Netherlands, 2007;

[7] J. R. Bowen, *The formation of ultra-fine grained model aluminium and steel alloys, PhD-thesis, University of Manchester Institute of Science and Technology*, Manchester, Great Britain, 2000;

[8] J. R. Bowen, P. B. Prangnell, F. J. Humphreys, *Microstructural evolution during formation of ultrafine grain structures by severe deformation*, Materials Science and Technology, vol. 16, no. 11-12, pp. 1246-1250, 2000;

[9] J. R. Bowen, A. Gholinia, S. M. Roberts, P. B. Prangnell, *Analysis of billet deformation behaviour in equal-channel angular extrusion*, Materials Science and Engineering A, vol. 287, pp. 87-99, 2000;

[10] H. J. Bunge, *Texture Analysis in Materials Science - Mathematical Methods*, Butterworths, London, 1982;

[11] J. B. Burns, A. R. Hanson, E. M. Riseman, *Extracting straight lines*, IEEE Transactions on Pattern Analysis and Machine Intelligence, V, PAMI, vol. 8, p. 425, 1986;

[12] A. Day, P. Trimby, *Channel 5 Manual*, HKL Technology, Hobro, Denmark, 2001;

[13] R. D. Doherty, D. A. Hughes, F. J. Humphreys, J. J. Jonas, D. Juul Jensen, M.E. Kassner, W. E. King, T. R. McNelley, H. J. McQueen, A. D. Rollett, *Current issues in recrystallization: a review*, Materials Science and Engineering A, vol. 238, pp. 219–274, 1997;

[14] S. Ferrasse, V. M. Segal, K. T. Hartwig, R. E. Goforth, *Microstructures and Properties of Copper and Aluminum Alloy 3003 Heavily Worked with Equal-channel Angular Extrusion*, Metallurgical and Materials Transactions A, vol. 28A, pp. 1047-1057, 1997;

[15] S. Ferrasse, V.M. Segal, K. T. Hartwig, R. E. Goforth, *Development of a submicrometer-grained microstructure in aluminium 6061 using equal-channel angular extrusion*, Journal of Materials Research, vol. 12, no. 5, pp. 1253-1261, 1997;

[16] Y. Fukuda, K. Oh-Ishi, Z. Horita, T. G. Langdon, *Processing of a low-carbon steel by equal-channel angular pressing*, Acta Materialia, vol. 50, pp. 1359–1368, 2002;

[17] M. Furukawa, Y. Iwahashi, Z. Horita, M. Nemoto, T. G. Langdon, *The shearing characteristics associated with equal-channel angular pressing*, Materials Science and Engineering A, vol. 257, pp. 328-332, 1998;

[18] A. Gholinia, P. B. Prangnell, M. V. Markushev, *The effect of strain path on the development of deformation structures in severely deformed aluminium alloys processed by ECAP*, Acta Materialia, vol. 48, pp. 1115-1130, 2000;

[19] J. Gil Sevillano, P. Van Houtte, E. Aernoudt, *Large strain work hardening and texture*, Progress in Materials Science, vol. 25, pp. 69-412, 1980;

[20] H. Gleiter, *Nanocrystalline Materials*, Progress in Materials Science, vol. 33, no. 4, pp. 223 -315, 1989;

[21] H. Gleiter, *Nanostructured materials: state of the art and perspectives*, Nanostructured Materials, vol. 6, no. 1-4, pp. 3-14, 1995;

[22] E. O. Hall, *The deformation and ageing of mild steel III: discussion of results*, Proceedings of the Physical Society B, vol. 64, pp. 747-753, 1951;

[23] B. Q. Han, E. J. Lavernia, F. A. Mohamed, *Mechanical properties of iron processed by severe plastic deformation*, Metallurgical and Materials Transactions A, vol. 34A, no. 1, pp. 71-83, 2003;

[24] Z. Horita, M. Furukawa, M. Nemoto, T. G. Langdon, *Development of fine grained structures using severe plastic deformation*, Materials Science and Technology, vol. 16, no. 11-12, pp. 1239-1245, 2000;

[25] Z. Horita, T. Fujinami, M. Nemoto, T. G. Langdon, *Improvement of mechanical properties for Al using equal-channel angular pressing*, Journal of Materials Processing Technology, vol. 117, pp. 288-292, 2001;

[26] P. V. C. Hough, *United States Patent No. 3,069,654*, 1962;

[27] D. A. Hughes, N. Hansen, *Microstructural evolution of nickel during rolling and torsion*, Materials Science and Technology, vol. 7, pp. 544–553, 1991;

[28] D. A. Hughes, N. Hansen, *High angle boundaries formed by grain subdivision mechanisms*, Acta Materialia, vol. 45, no. 9, pp. 3871-3886, 1997;

[29] F. J. Humphreys, M. G. Ardakani, *The deformation of particle-containing aluminium single crystals*, Acta Metallurgica et Materialia, vol. 42, pp. 749-761, 1994;

[30] F. J. Humphreys, P. S. Bate, P. J. Hurley, *Orientation averaging of electron backscattered diffraction data*, Journal of Microscopy, vol. 201, no. 1, pp. 50-58, 2001;

[31] F. J. Humphreys, *Review: Grain and subgrain characterisation by electron backscatter diffraction*, Journal of Materials Science, vol. 36, no. 16, pp. 3833-3854, 2001;

[32] F. J. Humphreys, M. Hatherly, *Recrystallization and Related Annealing Phenomena*, Pergamon, Oxford, UK, 2nd edition, 2002;

[33] B. Hutchinson, *Deformation microstructures and textures in steels*, Philosophical Transactions of the Royal Society in London, vol. 357A, pp. 1471-1485, 1999;

[34] J. Illingworth, J. Kitter, *A Survey of the Hough Transform*, Computer Vision, Graphics and Image Processing, vol. 44, pp. 87-116, 1988;

[35] Y. Iwahashi, J. Wang, Z. Horita, M. Nemoto, T. G. Langdon, *Principle of Equal-Channel Angular Pressing for the Processing of Ultra-fine Grained Materials*, Scripta Materialia, vol. 35, no. 2, pp. 143-146, 1996;

[36] Y. Iwahashi, Z. Horita, M. Nemoto, T. G. Langdon, *An Investigation of Microstructural Evolution During Equal-Channel Angular Pressing*, Acta Materialia, vol. 45, no. 11, pp. 4733-4741, 1997;

[37] Y. Iwahashi, Z. Horita, M. Nemoto, T. G. Langdon, *The Process of Grain Refinement in Equal-Channel Angular Pressing*, Acta Materialia, vol. 46, no. 9, pp. 3317-3331, 1998;

[38] Y. Iwahashi, M. Furukawa, Z. Horita, M. Nemoto, T. G. Langdon, *Microstructural Characteristics of Ultrafine-Grained Aluminum Processed During Equal-Channel Angular Pressing*, Metallurgical and Materials Transactions A, vol. 29A, pp. 2245-2252, 1998;

[39] H. Jin, D. J. Lloyd, *The Tensile Response of a Fine-Grained AA5754 Alloy Produced by Asymmetric Rolling and Annealing*, Metallurgical and Materials Transactions A, vol. 35A, no. 3A, pp. 997-1006, 2004;

[40] R. Kaibyshev, I. Mazurina, *Mechanisms of Grain Refinement in Aluminum Alloys during Severe Plastic Deformation*, Materials Science Forum, vol. 467-470, pp. 1251-1260, 2004;

[41] L. A. I. Kestens, *Private communication*, 2005;

[42] H.-K. Kim, M.-I. Choi, C.-S. Chung, D. H. Shin, *Fatigue properties of ultrafine grained low carbon steel produced by equal-channel angular pressing*, Materials Science and Engineering A, vol. 340, pp. 243-250, 2003;

[43] H. S. Kim, S. I. Hong, M. H. Seo, *Effects of strain hardenability and strain-rate sensitivity on the plastic flow and deformation homogeneity during equal-channel angular pressing*, Journal of Materials Research, vol. 16, no. 3, pp. 856-864, 2001;

[44] H. S. Kim, *Finite element analysis of equal-channel angular pressing using a round corner die*, Materials Science and Engineering A, vol. 315, pp. 122-128, 2001;

[45] Y. S. Kim, T. Lee, K.-T. Park, W.-J. Kim, D. H. Shin, Dry sliding wear behavior of ultrafine grained commercial purity aluminum and low carbon steel produced by severe plastic deformation techniques, in: "*Ultrafine Grained Materials II*" (as held at the 2002 TMS Annual Meeting), Charlotte, NC, USA, pp. 409-418, 2002;

[46] C. C. Koch, Y. S. Cho, *Nanocrystals by High Energy Ball Milling*, Nanostructured Materials, vol. 1, no. 3, pp. 207-212, 1992;

[47] C. C. Koch, Processing of Nanophase Materials by High Energy Ball Milling, in: "*Nanophases and Nanocrystalline Structures*", The Minerals, Metals & Materials Society, pp. 19-31, 1993;

[48] S. Komura, P. B. Berbon, M. Furukawa, Z. Horita, M. Nemoto, T. G. Langdon, *High strain rate superplasticity in an Al-Mg alloy containing scandium*, Scripta Materialia, vol. 38, no. 12, pp. 1851–1856, 1998;

[49] S. Komura, Z. Horita, M. Nemoto, T. G. Langdon, *Influence of stacking fault energy on microstructural development in equal-channel angular pressing*, Journal of Materials Research, vol. 14, no. 10, pp. 4044-4050, 1999;

[50] A. V. Korznikov, G. Tram, O. Dimitrov, G. F. Korznikova, S. R. Idrisova, Z. Pakiela, *The mechanism of nanocrystalline structure formation in Ni_3Al during severe plastic deformation*, Acta Materialia, vol. 49, no. 4, pp. 663-671, 2001;

[51] N. C. Krieger Lassen, K. Conradsen, D. Juul Jensen, *Image processing procedures for analysis of electron backscattering patterns*, Scanning Microscopy, vol. 6, p. 115, 1992;

[52] K. Kunze, S. I. Wright, B. L. Adams, D. J. Dingley, *Advances in automatic EBSP single orientation measurements*, Textures and Microstructures, vol. 20, pp. 41-54, 1993;

[53] M. Kuwahara, S. Eiho, *Processing of radio-isotope angiocardiographic images*, in: Digital Processing of Biomedical Images, K. Preston and M. Onoe, pp. 187-203, Plenum Press, New York, 1976;

[54] G. Langford, *Deformation of Pearlite*, Metallurgical Transactions A, vol. 8, p. 861-875, 1977;

[55] J. van de Langkruis, R. Bergwerf, S. van der Zwaag, W. H. Kool, *Linking Plain Strain Compression Tests on AA6063 to Laboratory Scale Extrusion via Constitutive Equations*, Materials Science Forum, vols. 331 - 337, pp. 565 - 570, 2000;

[56] D. N. Lee, *An Upper-Bound Solution of Channel Angular Deformation*, Scripta Materialia, vol. 43, pp. 115–118, 2000;

[57] S. H. Lee, Y. Saito, N. Tsuji, H. Utsunomiya, T. Sakai, *Role of shear strain in ultragrain refinement by accumulative roll-bonding (ARB) process*, Scripta Materialia, vol. 46, pp. 281–285, 2002;

[58] S. M. Lee, T. G. Langdon, *High Strain Rate Superplasticity in a Zn-22%Al Alloy after Equal-Channel Angular Pressing*, Materials Science Forum, vols. 357-459, pp. 321-326, 2001;

[59] M. Mabuchi, K. Ameyama, H. Iwasaki, K. Higashi, *Low temperature superplasticity of AZ91 magnesium alloy with non-equilibrium boundaries*, Acta Materialia, vol. 47, no. 7, pp. 2047-2057, 1999;

[60] K. Nakashima, Z. Horita, M. Nemoto, T. G. Langdon, *Influence of channel angle on the development of ultrafine grains in equal-channel angular pressing*, Acta Materialia, vol. 46, no. 5, pp. 1589-1599, 1998;

[61] G. H. Nijhof, *Accelerated spheroidization of cold rolled eutectoid steel*, PhD-thesis, Delft University of Technology, Delft, The Netherlands, 1981;

[62] K. Oh-Ishi, Z. Horita, M. Furukawa, M. Nemoto, T. G. Langdon, *Optimizing the Rotation Conditions for Grain Refinement in Equal-channel Angular Pressing*, Metallurgical and Materials Transactions A, vol. 29A, pp. 2011-2013, 1998;

[63] K.-T. Park, Y.-S. Kim, J. G. Lee, D. H. Shin, *Thermal stability and mechanical properties of ultrafine grained low carbon steel*, Materials Science and Engineering A, vol. 293, pp. 165-172, 2000;

[64] N. J. Petch, *The cleavage strength of polycrystals*, Journal of the Iron and Steel Institute, vol. 174, pp. 25-28, 1953;

[65] P. B. Prangnell, J. R. Bowen, A. Gholinia, The formation of submicron and nanocrystalline alloys by severe deformation, in: "*Proceedings of the 22nd Risø International Symposium on Materials Science*", edited by A. R. Dinesen, M. Eldrup, D. Juul Jensen, S. Linderoth, T. B. Pedersen, N. H. Pryds, A. Schrøder Pedersen, J. A. Wert, Risø National Laboratory, Roskilde, Denmark, 2001;

[66] A. Querales, J. G. Burne, *Effects of Thermomechanical Treatments on the Mechanical Behavior of Eutectoid Steel*, Metallurgical Transactions A, vol. 11A, pp. 255-266, 1980;

[67] V. Randle, O. Engler, *Introduction to texture analysis: macrotexture, microtexture and orientation mapping*, 1st edition, Gordon and Breach Science Publishers, Amsterdam, The Netherlands, 2000, ISBN 90-5699-224-4;

[68] R. E. Reed-Hill, R. Abbaschian, *Physical Metallurgy Principles*, 3rd edition, PWS Publishing Company, Boston, USA, 1991;

[69] A. C. C. Reis, L. A. I. Kestens, Y. Houbaert, *Lamellar Subdivision during Accumulative Roll Bonding of a Titanium Interstitial Free Steel*, Materials Science Forum, vols. 495-497, pp. 351-356, 2005;

[70] Y. Saito, H. Utsunomiya, N. Tsuji, T. Sakai, Proposal of novel ultra-high straining process for bulk materials: Development of the accumulative roll-bonding (ARB) process, in "*Aluminium Alloys: Their Physical and Mechanical Properties*", Japan Institute of Light Metals, pp. 2003-2008, 1998;

[71] Y. Saito, H. Utsunomiya, N. Tsuji, T. Sakai, *Novel ultra-high straining process for bulk materials: Development of the accumulative roll-bonding (ARB) process*, Acta Materialia, vol. 47, no. 2, pp. 579-583, 1999;

[72] Y. Saito, M. Mabuchi, M. Nakanishi, I. Shigematsu, G. Yamauchi, M. Nakamura, *Application of equal-channel angular extrusion on strengthening of ferritic stainless steel*, Journal of Materials Science, vol. 36, no. 13, pp. 3229-3232, 2001;

[73] A. J. Schwartz, M. Kumar, B. L. Adams, *Electron Backscatter Diffraction in Materials Science*, 1st edition, Kluwer Academic/Plenum Publishers, New York, USA, 2000;

[74] V. M. Segal, *Patent of the U.S.S.R. No. 575,892*, 1977;

[75] V. M. Segal, V. I. Reznikov, A. E. Drobyshevskiy, V. I. Kopylov, *Russian Metallurgy* (English translation), vol. 1, pp. 99-105, 1981;

[76] V. M. Segal, R. E. Goforth, K. T. Hartwig, *United States Patent No. 5,400,633*, 1995;

[77] V. M. Segal, *Materials processing by simple shear*, Materials Science and Engineering A, vol. 197, pp. 157-164, 1995;

[78] V.M. Segal, *Equal-channel angular extrusion: from macromechanics to structure formation*, Materials Science and Engineering A, vol. 271, pp. 322-333, 1999;

[79] D. H. Shin, W. J. Kim, W. Y. Choo, *Grain refinement of a commercial 0.15 % C steel by equal-channel angular pressing*, Scripta Materialia, vol. 41, no. 3, pp 259-262, 1999;

[80] D. H. Shin, C. W. Seo, J. Kim, K.-T. Park, W. Y. Choo, *Microstructures and mechanical properties of equal-channel angular pressed low carbon steel*, Scripta Materialia, vol. 42, pp. 695-699, 2000;

[81] D. H. Shin, B. C. Kim, Y.-S. Kim, K.-T. Park, *Microstructural evolution in a commercial low carbon steel by equal-channel angular pressing*, Acta Materialia, vol. 48, pp. 2247-2255, 2000;

[82] D. H. Shin, B. C. Kim, K.-T. Park, W. Y. Choo, *Microstructural changes in equal-channel angular pressed low carbon steel by static annealing*, Acta Materialia, vol. 48, pp. 3245-3252, 2000;

[83] D. H. Shin, I. Kim, J. Kim, K.-T. Park, *Grain refinement mechanism during equal-channel angular pressing of a low-carbon steel*, Acta Materialia, vol. 49, no. 7, pp. 1285-1292, 2001;

[84] D. H. Shin, Y. S. Kim, E. J. Lavernia, *Formation of fine cementite precipitates by static annealing of equal-channel angular pressed low-carbon steels*, Acta Materialia, vol. 49, pp. 2387-2393, 2001;

[85] D. H. Shin, J. J. Pak, Y. K. Kim, K.-T. Park, Y. S. Kim, *Effect of pressing temperature on microstructure and tensile behavior of low carbon steels processed by equal-channel angular pressing*, Materials Science and Engineering A, vol. 325, pp. 31–37, 2002;

[86] P. L. Sun, P. W. Kao, C. P. Chang, *High angle boundary formation by grain subdivision in equal channel angular extrusion*, Scripta Materialia, vol. 51, pp. 565-570, 2004;

[87] R. Z. Valiev, R. K. Islamgaliev, I. V. Alexandrov, *Bulk nanostructured materials from severe plastic deformation*, Progress in Materials Science, vol. 45, pp. 103-189, 2000;

[88] J. Wang, Y. Iwahashi, Z. Horita, M. Nemoto, M. Furukawa, R.Z. Valiev, T.G. Langdon, *An Investigation of Microstructural Stability of an Al-Mg Alloy with Submicrometer Grain Size*, Acta Materialia, vol. 44, no. 7, pp. 2973-2982, 1996;

[89] J. Wang, S.-B. Kang, H.-W. Kim, Z. Horita, *Lamellae deformation and structural evolution in an Al-33%Cu eutectic alloy during equal-channel angular pressing*, Journal of Materials Science, vol. 37, pp. 5223-5227, 2002;

[90] J. Wang, S.-B. Kang, H.-W. Kim, *Microstructure Transformation from Lamellar to Equiaxed Microduplex through Equal-Channel Angular Pressing in an Al-33%Cu Eutectic Alloy*, Metallurgical and Materials Transactions A, vol. 35A, pp. 279-286, 2004;

[91] J. Wang, S.-B. Kang, H.-W. Kim, *Shear features during equal-channel angular pressing of a lamellae eutectic alloy*, Materials Science and Engineering A, vol. 383, pp. 356–361, 2004;

[92] S. I. Wright, B. L. Adams, *Automatic analysis of electron backscatter diffraction patterns*, Metallurgical Transactions A, vol. 23A, p. 759, 1992;

[93] Y. Wu, I. Baker, *An Experimental Study of Equal-channel Angular Extrusion*, Scripta Materialia, vol. 37, no. 4, pp. 437-442, 1997;

[94] A. Yamashita, D. Yamaguchi, Z. Horita, T. G. Langdon, *Influence of pressing temperature on microstructural development in equal-channel angular pressing*, Materials Science and Engineering A, vol. 287, pp. 100-106, 2000;

[95] A. Yamashita, Z. Horita, T. G. Langdon, *Improving the mechanical properties of magnesium and magnesium alloy through severe plastic deformation*, Materials Science and Engineering A, vol. 300, pp. 142-147, 2001;

[96] G. G. Yapici, I. Karaman, Z. P. Luo, H. J. Maier, Y. I. Chumlyakov, *Microstructural refinement and deformation twinning during severe plastic deformation of 316L stainless steel at high temperatures*, Journal of Materials Research, vol. 19, no. 8, pp. 2268-2278, 2004;

[97] V. A. Zhorin, I. F. Makarova, M. A. Gen, N. S. Enikolopyan, *Formation of Metal Solid Solutions During Plastic Flow Under High Pressure*, Dokl. Akad. Nauk. SSSR, vol. 261, no. 2, pp. 405 -408, 1981;

[98] V. A. Zhorin, D. P. Shashkin, N. S. Enikolopian, *Dynamics of Solid Solution Formation in Cu-Ni Mixture Under Plastic Flow at High Pressure*, Physica Status Solidi A, vol. 89, no. 2, pp. 437-442, 1985;

[99] Y. T. Zhu, H. Jiang, D. P. Butt, I. V. Alexandrov, T. C. Lowe, *Microstructural evolution, microhardness and thermal stability of HPT-processed Cu*, Materials Science and Engineering A, vol. 290, no. 1-2, pp. 128-138, 2000;

[100] Y. T. Zhu, T. C. Lowe, *Observations and issues on mechanisms of grain refinement during ECAP process*, Materials Science and Engineering A, vol. 291, pp. 46-53, 2000;

APPENDIX A

RESULTS OF THE SEM-ANALYSIS

Table A1. Average values of the selected parameters, obtained from quantitative analysis of the secondary electron images of the three severely deformed high-carbon steels.

Parameter	Number of passes Steel	0	1	2	3	4	5
A (μm²)	Hypo-eutectoid	0.06		0.05	0.03	0.06	0.05
	Eutectoid		0.14	0.05	0.06	0.04	0.04
	Hyper-eutectoid		0.14	0.16	0.09	0.09	0.03
P (μm)	Hypo-eutectoid	1.73		1.38	0.74	1.35	0.97
	Eutectoid		2.33	1.38	1.18	0.94	0.92
	Hyper-eutectoid		2.16	2.19	1.60	1.40	0.80
ECD (μm)	Hypo-eutectoid	0.24		0.21	0.15	0.23	0.21
	Eutectoid		0.32	0.20	0.21	0.19	0.18
	Hyper-eutectoid		0.34	0.35	0.26	0.27	0.16
R (-)	Hypo-eutectoid	4.080		3.191	2.020	2.645	1.783
	Eutectoid		3.793	3.529	2.292	1.998	2.007
	Hyper-eutectoid		3.106	3.230	2.733	2.096	1.925

Table A2. Standard deviation values of the selected parameters, obtained from quantitative analysis of the secondary electron images of the three severely deformed high-carbon steels.

Parameter	Number of passes Steel	0	1	2	3	4	5
A (μm²)	Hypo-eutectoid	0.005		0.004	0.002	0.005	0.003
	Eutectoid		0.018	0.006	0.005	0.004	0.004
	Hyper-eutectoid		0.016	0.020	0.009	0.006	0.003
P (μm)	Hypo-eutectoid	0.114		0.081	0.038	0.075	0.036
	Eutectoid		0.228	0.142	0.077	0.050	0.061
	Hyper-eutectoid		0.176	0.229	0.125	0.075	0.044
ECD (μm)	Hypo-eutectoid	0.008		0.007	0.004	0.007	0.004
	Eutectoid		0.013	0.012	0.009	0.006	0.007
	Hyper-eutectoid		0.017	0.021	0.012	0.010	0.006
R (-)	Hypo-eutectoid	0.241		0.132	0.052	0.107	0.036
	Eutectoid		0.281	0.262	0.082	0.051	0.059
	Hyper-eutectoid		0.169	0.208	0.139	0.065	0.044

APPENDIX B

RESULTS OF THE EBSD-ANALYSIS

Table B1. Data manipulation parameters for the orientation image maps that are used for display purposes only.

Steel	**Hypo-eutectoid**			**Eutectoid**			**Hyper-eutectoid**		
Number of ECAP-passes	**3**	**4**	**5**	**3**	**4**	**5**	**3**	**4**	**5**
Removal of suspect points	Yes	Yes	Yes	Yes	Yes	Yes	Yes	Yes	Yes
Removal of misindexed points	No	Yes	Yes	No	Yes	Yes	No	No	No
Subgrain reconstruction	L3 (full)	L3 (full)	L3 (full)	N/A	L3 (full)	L3 (full)	N/A	L3 (1c)	L3 (full)

Table B2. Data manipulation parameters for the orientation image maps that are used for statistical calculations with removal of the suspect and misindexed data points.

Steel	**Hypo-eutectoid**			**Eutectoid**			**Hyper-eutectoid**		
Number of ECAP-passes	**3**	**4**	**5**	**3**	**4**	**5**	**3**	**4**	**5**
Removal of suspect points	Yes	Yes	Yes	Yes	Yes	Yes	Yes	Yes	Yes
Removal of misindexed points	Yes	Yes	Yes	Yes	Yes	Yes	No	No	No
Subgrain reconstruction	L3 (full)	L3 (full)	L3 (full)	L3 (full)	L3 (full)	L3 (full)	L3 (full)	L3 (1c)	L3 (full)
Orientation averaging									
- Filter	K9	K9	K9	K9	K9	K9	K9	K9	K9
- Number of cycles	1	1	1	1	1	1	1	1	1
- Boundary threshold value (°)	1.5	1.5	1.5	1.5	1.5	1.5	1.5	1.5	1.5
Subgrain reallocation threshold value (px)	≤4	≤4	≤4	≤4	≤4	≤4	≤4	≤4	≤4

The tables listed on the next two pages show the results of the statistical calculations on the data from the orientation image maps. Abbreviations used in these tables: the area (A), the equivalent circular diameter (ECD), the length in the normal direction ($L_{ND} = L_x$) and the extrusion direction ($L_{ED} = L_y$), the aspect ratio between these two lengths ($L_{ND}/L_{ED} = L_x/L_y$), the total number (n) and the percentage of low-angle boundaries (%LAGB) and high-angle boundaries (%HAGB), the mean angular deviation (MAD) and the band contrast (BC).

All values mentioned in the tables on this page are calculated according to the incorrect routines that are built into VMAP.

Table B3. Average values for the grains.

Steel	Hypo-eutectoid			Eutectoid			Hyper-eutectoid		
Passes	**3**	**4**	**5**	**3**	**4**	**5**	**3**	**4**	**5**
ECD	1.13	1.70	x	x	0.84	1.02	0.59	1.17	0.22
L_{ND}	1.05	1.56	x	x	0.69	0.93	0.51	1.02	0.22
L_{ED}	2.08	2.83	x	x	1.31	1.48	0.87	1.62	0.23
L_{ND}/L_{ED}	0.51	0.55	x	x	0.52	0.63	0.59	0.63	0.96
n	390	901	x	x	1,580	690	10,591	3,796	33,581

Table B4. Standard deviation values for the grains.

Steel	Hypo-eutectoid			Eutectoid			Hyper-eutectoid		
Passes	**3**	**4**	**5**	**3**	**4**	**5**	**3**	**4**	**5**
ECD	2.05	3.52	x	x	1.33	1.27	0.99	1.28	0.23
L_{ND}	2.10	3.41	x	x	1.04	1.34	0.93	1.27	0.30
L_{ED}	5.05	7.63	x	x	2.82	2.39	2.61	2.96	0.31
L_{ND}/L_{ED}	0.86	0.99	x	x	0.87	0.88	1.05	0.90	1.31

Table B5. Average values for the subgrains.

Steel	Hypo-eutectoid			Eutectoid			Hyper-eutectoid		
Passes	**3**	**4**	**5**	**3**	**4**	**5**	**3**	**4**	**5**
ECD	0.57	0.99	0.83	0.56	0.55	0.57	0.56	0.89	0.26
L_{ND}	0.51	0.87	0.50	0.47	0.46	0.50	0.48	0.77	0.25
L_{ED}	0.77	1.14	1.62	0.80	0.68	0.69	0.66	1.02	0.27
L_{ND}/L_{ED}	0.66	0.76	0.31	0.59	0.67	0.72	0.73	0.75	0.95
n	2,843	9,205	1,246	3,383	8,736	3,602	35,594	12,452	36,545
%LAGB	49	57	53	63	42	41	44	40	15
%HAGB	51	43	47	37	58	59	56	60	85

Table B6. Standard deviation values for the subgrains.

Steel	Hypo-eutectoid			Eutectoid			Hyper-eutectoid		
Passes	**3**	**4**	**5**	**3**	**4**	**5**	**3**	**4**	**5**
ECD	0.49	0.44	0.79	0.39	0.31	0.33	0.24	0.25	0.16
L_{ND}	0.49	0.43	0.41	0.32	0.26	0.30	0.23	0.26	0.17
L_{ED}	1.05	0.82	2.04	0.79	0.53	0.49	0.39	0.41	0.21
L_{ND}/L_{ED}	1.90	0.93	0.91	0.83	0.91	0.94	0.88	0.88	1.30

All values mentioned in the tables on this page are calculated according to the routines discussed in section 4.2.1. Values in between brackets are found to be unreliable.

Table B7. Average values for the grains.

Steel	Hypo-eutectoid			Eutectoid			Hyper-eutectoid		
Passes	**3**	**4**	**5**	**3**	**4**	**5**	**3**	**4**	**5**
A	2.09	5.62	x	x	0.96	0.87	1.15	1.07	0.23
ECD	0.88	1.20	x	x	0.64	0.70	0.70	0.79	0.42
L_{ND}	0.99	1.20	x	x	0.61	0.75	0.63	0.79	0.47
L_{ED}	(1.40)	2.19	x	x	(1.01)	(1.09)	(1.00)	1.22	0.52
L_{ND}/L_{ED}	(0.71)	0.55	x	x	(0.60)	(0.69)	(0.63)	0.64	0.91
n	270	797	x	x	1,176	524	5,526	3,616	5,424

Table B8. Standard deviation values for the grains.

Steel	Hypo-eutectoid			Eutectoid			Hyper-eutectoid		
Passes	**3**	**4**	**5**	**3**	**4**	**5**	**3**	**4**	**5**
A	9.07	44.11	x	x	9.11	4.82	12.04	8.12	1.02
ECD	1.37	2.39	x	x	0.90	0.78	0.99	0.86	0.34
L_{ND}	1.64	2.55	x	x	0.81	0.96	0.99	0.96	0.50
L_{ED}	(2.43)	5.70	x	x	(1.28)	(1.45)	(2.01)	2.22	0.51
L_{ND}/L_{ED}	(0.68)	0.45	x	x	(0.64)	(0.66)	(0.49)	0.43	0.99

Table B9. Average values for the subgrains.

Steel	Hypo-eutectoid			Eutectoid			Hyper-eutectoid		
Passes	**3**	**4**	**5**	**3**	**4**	**5**	**3**	**4**	**5**
A	0.30	0.48	0.55	0.30	0.18	0.19	0.20	0.31	0.14
ECD	0.51	0.71	0.72	0.55	0.44	0.46	0.47	0.60	0.38
L_{ND}	0.49	0.63	0.68	0.48	0.41	0.44	0.42	(0.53)	0.39
L_{ED}	(1.83)	(6.20)	(1.25)	(1.39)	(1.68)	(1.60)	(2.47)	(3.21)	(2.01)
L_{ND}/L_{ED}	(0.27)	(0.10)	(0.54)	(0.35)	(0.25)	(0.27)	(0.17)	(0.16)	(0.20)
n	1,785	9,205	908	2,197	6,088	2,201	31,075	12,452	7,960

Table B10. Standard deviation values for the subgrains.

Steel	Hypo-eutectoid			Eutectoid			Hyper-eutectoid		
Passes	**3**	**4**	**5**	**3**	**4**	**5**	**3**	**4**	**5**
A	0.90	1.05	0.76	0.47	0.21	0.18	0.20	0.21	0.15
ECD	0.36	0.33	0.43	0.29	0.18	0.18	0.19	0.18	0.16
L_{ND}	0.33	0.29	0.38	0.26	0.16	0.15	0.16	(0.16)	0.15
L_{ED}	(1.36)	(5.04)	(0.93)	(1.04)	(1.10)	(1.00)	(1.53)	(1.44)	(0.96)
L_{ND}/L_{ED}	(0.24)	(0.06)	(0.41)	(0.25)	(0.14)	(0.15)	(0.11)	(0.11)	(0.15)

Table B11. Survey of the settings for the acquisition of the Kikuchi-bands and of several of the resulting parameters.

Steel	**Hypo-eutectoid**			**Eutectoid**			**Hyper-eutectoid**		
Passes	**3**	**4**	**5**	**3**	**4**	**5**	**3**	**4**	**5**
Acc. voltage	20 keV	20 keV	20 keV	20 keV	20 keV	20 keV	20 keV	20 keV	20 keV
Working distance	20 mm	20 mm	20 mm	20 mm	20 mm	20 mm	20 mm	20 mm	20 mm
Beam size	3	3	3	3	3	3	3	3	3
Aperture size	4	4	4	4	4	4	4	4	4
Magnification	2,000x	1,000x	2,000x	2,000x	2,000x	2,000x	1,000x	1,000x	2,000x
Map width	30 µm	80 µm	30 µm	30 µm	45 µm	30 µm	90 µm	80 µm	45 µm
Map height	30 µm	80 µm	29 µm	30 µm	45 µm	30 µm	90 µm	80 µm	45 µm
Step size	0.05 µm	0.20 µm	0.05 µm	0.05 µm	0.05 µm	0.05 µm	0.10 µm	0.20 µm	0.05 µm
Detected phases	αFe	αFe	αFe	αFe	αFe	αFe	αFe, Fe_3C	αFe	αFe, Fe_3C
V/H-ratio	0.753	0.757	0.797	0.775	0.783	0.783	0.774	0.757	0.753
Min. intensity	0 %	0 %	0 %	0 %	0 %	0 %	0 %	0 %	0 %
Min. no. bands	4	4	4	4	4	4	4	4	4
Max. no. bands	5	6	5	5	5	5	6	6	5
Hough resolution	70	60	60	70	60	70	60	55	65
MAD	0.4	0.4	0.4	0.5	0.4	0.3	0.5	0.4	0.6
Mean BC	83	110	75	114	72	66	139	77	99
% ind. before	63	70	58	77	56	51	80	61	80
% ind. after	100	100	100	100	100	100	100	91	100

APPENDIX C

RESULTS OF THE MECHANICAL TESTING

Table C1. Vickers microhardness (using a 1 kg load) of the three high-carbon steels. The values for the average and the corresponding standard deviation are calculated from the mean of ten measurements.

Steel	Deformation (-)	Number of passes (-)	Average (HV)	Standard deviation (HV)
Hypo-eutectoid	0.00	0	213	5
Hypo-eutectoid	0.67	1	286	9
Hypo-eutectoid	1.33	2	299	6
Hypo-eutectoid	2.00	3	297	9
Hypo-eutectoid	2.67	4	297	11
Hypo-eutectoid	3.33	5	290	9
Eutectoid	0.00	0	254	16
Eutectoid	0.67	1	322	7
Eutectoid	1.33	2	322	9
Eutectoid	2.00	3	318	7
Eutectoid	2.67	4	323	5
Eutectoid	3.33	5	323	5
Hyper-eutectoid	0.00	0	250	10
Hyper-eutectoid	0.67	1	335	10
Hyper-eutectoid	1.33	2	341	7
Hyper-eutectoid	2.00	3	346	9
Hyper-eutectoid	2.67	4	341	11
Hyper-eutectoid	3.33	5	344	9

Table C2. Results from the tensile tests that were carried out on the three high-carbon steels as determined by Corus Swinden Technology Centre in Rotherham, England.

Steel	Deformation (-)	Number of passes (-)	0.2% Proof stress (MPa)	0.5% Proof stress (MPa)	Ultimate tensile stress (MPa)	Fracture elongation (%)
Hypo-eutectoid	0.00	0	351	386	743	18
Hypo-eutectoid	0.67	1	717	738	910	10
Hypo-eutectoid	1.33	2	802	809	945	10
Hypo-eutectoid	2.00	3	865	864	957	12
Hypo-eutectoid	2.67	4	884	889	974	9
Hypo-eutectoid	3.33	5				
Eutectoid	0.00	0	418	475	878	13
Eutectoid	0.67	1	795	821	1033	7
Eutectoid	1.33	2	896	908	1069	8
Eutectoid	2.00	3	922	929	1033	9
Eutectoid	2.67	4	982	981	1036	13
Eutectoid	3.33	5				
Hyper-eutectoid	0.00	0	385	420	860	10
Hyper-eutectoid	0.67	1	828	849	1063	6
Hyper-eutectoid	1.33	2	932	938	1090	6
Hyper-eutectoid	2.00	3	1050	1044	1141	5
Hyper-eutectoid	2.67	4	1066	1073	1112	4
Hyper-eutectoid	3.33	5				

ABSTRACT

This master thesis deals with the research to the effects of severe plastic deformation on the development of the microstructure and the mechanical properties of three low-alloyed high-carbon steels. The steels investigated include a hypo-eutectoid, an eutectoid and a hyper-eutectoid steel containing 0.61, 0.81 and 1.22 weight-percent carbon. The microstructure of the eutectoid steel consists only of pearlite, whereas that of the hypo-eutectoid and the hyper-eutectoid steels also contains several volume-percent of ferrite and grain boundary cementite, respectively.

Several experiments were conducted using equal-channel angular pressing at a processing temperature of 500 °C (773 K). The die configuration consisted of a channel angle of 120° and a corner angle of 0°, yielding an effective deformation of 0.67 per pass. The microstructure was analysed and the mechanical properties were assessed after each pass. Samples were analysed both in the initial and in the deformed conditions by means of hardness testing, qualitative and quantitative image analysis using secondary electrons in a scanning electron microscope and the assessment of the crystallographic orientation using electron backscattered diffraction.

The results revealed the formation of very complex microstructures due to the severe deformation. The cementite lamellae deform plastically and gradually break up into tiny segments of the size of coarse second-phase particles. Besides, small pieces of pearlite regroup to form smaller clusters in the hyper-eutectoid steel. A subgrain structure is formed in the ferrite phase and in the ferrite lamellae, exhibiting a subgrain boundary misorientation that progressively rises from low- to high-angle boundaries with increasing deformation. It appeared that the size of the subgrains is largely controlled by the interlamellar distance of the cementite lamellae and that the subgrain boundary misorientation is determined by the local amount of deformation. The mechanical properties exhibit dramatic changes; from 351 MPa to 1,066 MPa for the yield strength and from 743 MPa to 1,141 MPa for the ultimate tensile strength, but contradictory values for the elongation at fracture.

Keywords: severe plastic deformation (SPD), equal-channel angular pressing (ECAP), high-carbon steel, ultrafine grains, subgrain structure, electron backscattered diffraction (EBSD), scanning electron microscopy (SEM), hardness, tensile testing

SAMENVATTING

Dit afstudeerverslag gaat over het onderzoek naar de invloeden van extreme vervorming op de ontwikkeling van de microstructuur en de mechanische eigenschappen van drie laaggelegeerde hoogkoolstofstaalsoorten. De onderzochte staalsoorten omvatten een ondereutectoïdische, een eutectoïdische en een boveneutectoïdische staalsoort met respectievelijk 0,61, 0,81 en 1,22 gewichtsprocent koolstof. De microstructuur van het eutectoïdische staal bestaat enkel uit perliet, terwijl die van het ondereutectoïdische en het boveneutectoïdische staal tevens enkele volumeprocent ferriet respectievelijk cementiet bevat.

Voor dit onderzoek zijn meerdere proeven uitgevoerd met behulp van knikmatrijspersen bij een procestemperatuur van 500 °C (773 K). De matrijs bestond uit twee kanalen die elkaar onder een hoek van 120° snijden, gebruik makend van een afrondingshoek van 0°, waardoor een effectieve rek van 0,67 per perscyclus werd bereikt. Na elke perscyclus werd de microstructuur van de proefstukken geanalyseerd en werden de mechanische eigenschappen bepaald. De proefstukken zijn zowel in de uitgangstoestand als in de vervormde toestanden geanalyseerd met behulp van hardheidsmetingen, kwalitatieve en kwantitatieve beeldanalyse met behulp van secundaire elektronen in een scanning-elektronenmicroscoop en bepaling van de kristallografische oriëntatie door middel van elektronendiffractie in een scanning-elektronenmicroscoop.

De resultaten tonen dat door de extreme vervorming zeer complexe microstructuren worden gevormd. De cementietlamellen vervormen plastisch en breken geleidelijk op in uiterst kleine stukken ter grootte van grove tweedefasedeeltjes. Daarnaast hergroeperen kleine stukken perliet zich tot kleinere en grillig gevormde "deeltjes" in het boveneutectoïdische staal. In de ferrietfase en de -lamellen wordt een subkorrelstructuur gevormd, waarvan de subkorrelgrensmisoriëntatie geleidelijk toeneemt van kleine- tot grotehoeksubkorrelgrenzen. Het is gebleken dat de grootte van de subkorrels afhangt van de afstand tussen de cementietlamellen en de subkorrelgrensmisoriëntatie afhangt van de lokale hoeveelheid vervorming. De mechanische eigenschappen vertonen een drastische verandering; van 351 MPa tot 1.066 MPa voor de rekgrens en van 743 MPa tot 1.141 MPa voor de treksterkte, maar tegenstrijdige waarden voor de breukrek.

Trefwoorden: extreme vervorming, knikmatrijspersen, hoogkoolstofstaal, ultrafijne korrels, subkorrelstructuur, elektronendiffractie, scanning-elektronenmicroscopie, hardheid, trekproeven